CONTROL OF LASING FROM A HIGHLY PHOTOEXCITED SEMICONDUCTOR MICROCAVITY

By

Feng-Kuo Hsu

A DISSERTATION

Submitted
to Michigan State University
in partial fulfillment of the requirements
for the degree of

Physics – Doctor of Philosophy

2016

ABSTRACT

CONTROL OF LASING FROM A HIGHLY PHOTOEXCITED SEMICONDUCTOR MICROCAVITY

By

Feng-Kuo Hsu

Technological advances in the fabrication of optical cavities and crystal growth have enabled the studies on macroscopic quantum states and emergent nonequilibrium phenomena of light-matter hybrids in condensed matter. Optical excitations in a semiconductor microcavity can result in a coupled electron-hole-photon (e-h-γ) system, in which various many-body physics can be studied by varying particle densities and particle-particle interactions. Recently there have been reports of phenomena analogous to Bose-Einstein condensates or superfluids for exciton-polaritons in a microcavity. An exciton-polariton is a quasiparticle resulting from strong coupling between the cavity light field and the exciton (e-h pair) transition, and typically is only stable at a low density ($\sim 10^{11}$ to $10^{12}\,cm^{-2}$ or less). At a higher density, it has been theoretically predicted that pairing of electrons and holes can result in a BCS-like state at cryogenic temperatures, which can produce cooperative radiation known as superradiance. In this work, we explore cooperative phenomena caused by e-h correlation and many-body effect in a highly photoexcited microcavity at room temperature.

High-density e-h plasmas in a photoexcited microcavity are studied under the following conditions: (1) the sample is photoexcited GaAs-based microcavity with large detuning between the band gap E_g of quantum well and cavity resonance to prevent carriers from radiative loss, (2) the density of e-h pairs is high enough to build long-range correlation with the assistance of cavity light field. The Fermi level of electron-hole pairs is about 80 meV above E_g, and (3) the e-h correlation is stabilized through thermal management, which includes modulating the excitation pulse laser temporally and spatially to reduce the heating and carrier diffusion effect. We have observed ultrafast (sub-10 picoseconds) spin-polarized lasing with sizable energy shifts and linewidth broadenings as

pump flux is increased. With optically induced confinement, multiple-lasing modes were produced, with sequential lasing time depending on energies. These phenomena are attributed to the spin-dependent stimulated emission from correlated e-h pairs. We further performed a non-degenerate pump-probe spectroscopy to investigate dynamic carrier relaxation. We find transient resonances with significant changes in differential reflectivity that can last more than 1 ns. The resonance exhibits a polarization-dependent splitting in about 1 meV under circularly polarized pumping. All the aforementioned phenomena can be explained by the combination effect of carrier-induced refractive index change and the light-induced e-h correlation.

Our research enriches the studies of coupled e-h-γ systems at room temperature and a high-density regime; however, further experiments and theoretical works are required to claim and clarify the formation of such correlated e-h pairs in a highly photoexcited microcavity. Nonetheless, we have demonstrated that many-body effects can be harnessed to control lasing dynamics and energies in highly photoexcited semiconductor microcavities. We expect an improved understanding of the many-body effect resulted from e-h pairing to help the development of polarization-controlled and wavelength-tunable lasers.

ACKNOWLEDGEMENTS

I would like to thank all those who contributed to the research presented in this dissertation. Fist of all, I wish to express my deep gratitude to my advisor, Chih-Wei Lai, for countless guidance, encouragement, and financial support. During my five years in Ph.D., I have learned invaluable experience from him such as problem solving as well as communication skill. In addition, his support to my next career step could not be overstated. Secondly, I would like to appreciate my second mentor, Wei Xie. He was patient on clearing my confusion in research, and was enthusiastic about discussing physics with me, which enriched my physics insight of my project. He also supported me when I was depressed both in research and daily life. Honestly speaking, the time that the three of us were together was probably my happiest period in my Ph.D. life.

There are many members at Michigan State University I would like to publicly thank with helping me in graduate program. Professor Brage Golding and John McGuire joined discussions for my projects with useful advise on research direction. My committee members always offered me great guidance and suggestions, so I could deliberate the research plan and learning how to present work better to people outside my field. Reza Loloee gave supports with equipment assistance all the time as well as the faith on the meaning of my work. Barry Tigner, Rob Bennett, Tom Hudson, and Thomas Palazzolo provided great help with assistance on electronic devices or mechanical tools. The secretaries in the department, Debbie Barratt, Kim Crosslan, and Cathy Cord assisted me a lot with affairs in graduate life. Our graduate director, Scott Prate, was willing to help us with any problems. I want to particularly thank Zeynep Altinsel, who gave me lots of support on improving my English speaking and communication. Without them, my graduate program would not have progressed smoothly.

I would like to acknowledge Greg Taft from KMLabs company who taught me a lot about the mode-locked mechanism in lasing and provided great consultation on technical problems. His support boosted our progress on two-color pump-probe project, and this experienceinitiated my

interest in the ultrafast laser field.

I am fortunate to have many friends during my graduate years, who have supported through traveling, concern and parties. Among my friends, I want to particularly thank my close classmates from National Taiwan University, who are almost my second family for their concern and support. More than seven years after graduation from university, I still feel our friendship strongly even through we are separated in more than ten places now.

Finally, this dissertation could not be possible without the support from my family, especially my parents' permanent love. Although we live at both ends of the earth, they never stop standing behind me. I thank them for their back in me, and I love my family forever.

TABLE OF CONTENTS

LIST OF TABLES

LIST OF FIGURES

CHAPTER 1

INTRODUCTION

1.1 Macroscopic quantum phenomena

Our world is mainly defined by two limits: the macroscopic limit described by Newton's Law, and the microscopic limit described by quantum mechanics. Bridging these two limits are few examples of "quantum macroscopic states," in which a significant correlation between particles makes the system behave like a macroscopic single state in classical physics. The most common example is the laser, where a large number of photons have the same energy and momentum. Other typical phenomena (corresponding to constituted particles) are superfluidity (liquid helium), superconductivity (bounded electron pairs, or Cooper pairs), and Bose-Einstein condensation (atomic gases) [1, 2]. The constituent particles in these macroscopic phenomena are all composite bosons.

A variety of quasi-particles with bosonic characters are found in solid state physics. In particular, the exciton, which is an electron-hole (e-h) pair bounded through Coulomb interaction in semiconductors, attracts much attention in research. In dilute density, excitons are regarded as bosons with a light effective mass (0.1 - 1 free electron mass m_0) compared to that of typical atomic gases; therefore, excitons could form Bose-Einstein condensation (BEC) at $\sim 1K$ [3, 4]. Since the transition temperature T_c of BEC is inversely proportional to its effective mass, the T_c of excitons' BEC is expected to be three to six order of magnitude greater than that of atomic gases' BEC. The strong coupling of an exciton (in bulk semiconductors or quasi-2D quantum wells) and a photon results in a quasiparticle, known as an exciton-polariton [5]. Like an exciton, an exciton-polariton is a composite boson with an even smaller effective mass ($10^{-1} - 10^{-4}\, m_0$), and has been considered as a candidate for room-temperature BEC [6].

1.2 Phase diagram in electron-hole physics

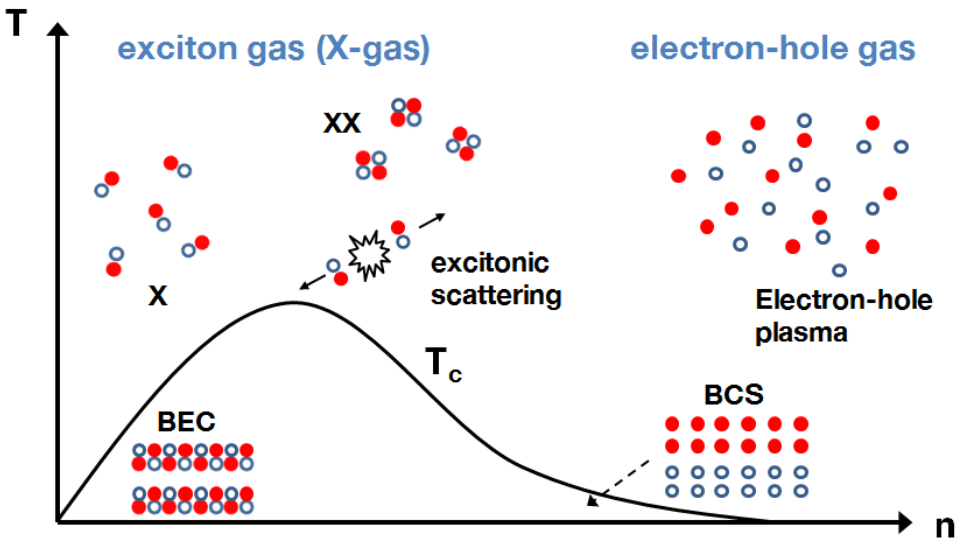

Figure 1.1 **Phase diagram of paired electrons and holes.** Symbolic schematic of paired electrons and holes (e-h) phase diagram as a function of temperature and density. At e-h density below Mott-transition density and $T > T_c$, where T_c is the critical temperature for the condensate of e-h pairs, the system phase might be dilute exciton gases (X), bi-exciton (XX) gases, and excitonic scattering process. The Mott transition is defined a region separating the system between "conducting state" (broken e-h pairs) and "insulating state" (exciton, e-h pairs are charge neutral). At low e-h density and $T < T_c$, exciton gas undergoes a transition to exciton Bose-Einstein condensation (BEC). At large e-h density and $T < T_c$, collective paired electrons and holes form by weak coupling, resembling Cooper pairs in superconductors, and are named as BCS-state. At e-h above Mott transition density and $T > T_c$, electrons and holes are almost free carriers forming electron-hole plasma (EHP).

The interaction and quantum correlation between excitons vary depending on the electron-hole density and the temperature; Fig. 1.1 illustrates the phase diagram of the electron-hole system. In dilute density of electrons and holes, the exciton behaves like a bosonic particle, and forms BEC in temperatures below transition temperature T_c in which the quantum correlation among excitons dominates the system. The exciton "condensate' has been experimentally reported in various studies [7, 8, 9, 10]. When the electron-hole density increases, the interaction of e-h pairs becomes complicated due to screening and spin effects in the e-h and exciton system. At sufficiently high density, screening of e-h Coulomb attraction inhibits the binding of e-h pairing, in

which excitons undergo a Mott transition to electron-hole plasma (EHP) [11]. However, correlated *e-h* pairs can still form a BCS-like states, near to the quasi-Fermi-level of an EHP [11, 12, 13]. Such a macroscopic BCS-like state would result in a cooperative radiation known as superradiance. Superradiance or superfluorescence, suggesting the formation of such a BCS-like state, has been reported in semiconductor quantum wells (QWs) [14, 15, 16]. Such a state could exist at cryogenic temperatures as large thermal fluctuation would destroy the binding of e-h pairs. At large electron-hole density and room temperature, the electrons and holes are usually incoherent. The common macroscopic phenomenon in this region is laser through photon stimulation.

The advanced technology of cavity fabrication enables the study of coupled photon-electron-hole systems. Due to their bosonic characteristics, as well as being a candidate for room temperature BEC, exciton-polaritons (hybrids of light and excitons) have been intensively investigated in semiconductor microcavity systems by numerous scientists in the past few decades. The exciton-polariton has a finite lifespan, and it is annihilated into photon radiation due to the recombination of the electron and the hole. Therefore, an exciton-polaritons' condensate could result in a large coherent radiation known as polariton lasing. So far, polariton lasing has apparently been found in GaAs-based devices [17, 18, 19], and CdTe-based devices [20]. Besides the "condensate" study, the bosonic characteristics of exciton-polaritons have stimulated other research relating to many-body physics in the reduced dimensional system. Many-body physics includes topics such as quantum vortices [21, 22], Berezinskii-Kosterlitz-Thouless (BKT) phases (a bound state of vortex and anti-vortex) [23, 24], Bogoliubov excitation [6, 25, 26], and superfluidity [27, 28]. The quantum interference between exciton-polaritons has also been studied in the confinements such as natural defect and potential fluctuation [29, 30, 31, 32], nanofabrication [33, 34, 35, 36, 37, 38], and optical potential [39, 40, 41, 42]. Most experiments on exciton-polaritons are performed at cryogenic temperatures, due to the small binding energy of excitons compared to thermal fluctuation. Nevertheless, the room-temperature polariton lasing has been reported in GaN-based devices [43, 44, 45] and ZnO-based devices [46, 47, 48], in which excitons are stable at room temperature as a result of a large binding energy ($\sim$ 20 - 60 meV). However, the aforementioned polariton

lasing occurs at a density much lower than the Mott-density; this is because a high carrier density enhances the screening effect and weakens the formation of excitons.

1.3 Motivation and approach

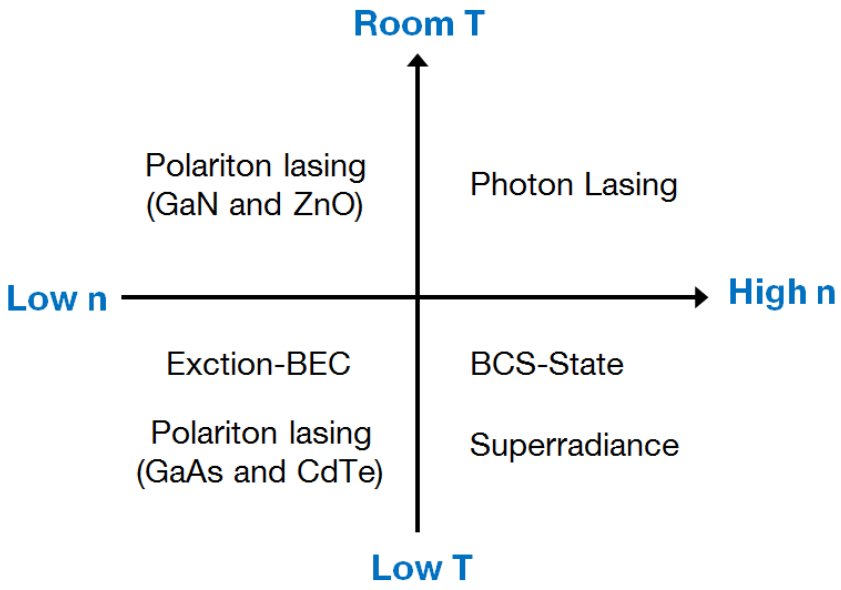

Figure 1.2 **Macroscopic quantum states in electron-hole system.** Simple phase diagram of macroscopic quantum states in e-h system as function of temperature and the density of e-h pairs. The critical carrier density separated from the low and the high e-h density is defined as the one at Mott-transition, which is typically about $10^{18}\,cm^{-3}$.

Fig. 1.2 shows a symbolic diagram of the aforementioned macroscopic quantum states at various levels of e-h density and temperature. Based on the diagram, it is rare that research convincingly presents many-body physics of particles at high density and room temperature, because the thermal fluctuation and screening effect destabilize the bound e-h pairs. However, theoretical studies claimed that the condensation of e-h pairs potentially exists near a band gap of semiconductors in dense EHP at room temperature [49]. Due to the insufficient number of experimental studies of many-body physics in e-h systems at high density and room temperature, we should devote our efforts to exploring the correlated e-h pairs at this region.

From the theoretical view, the presence of light would enhance the correlation between electrons and holes [50, 13]; therefore, we chose the semiconductor microcavity as our sample. Through the examination of the studies of cavity lasers and exciton-polaritons in microcavity systems, we can propose a few reasons why the formation of e-h condensates was inhibited at room temperature. First, the closed energy difference between cavity resonance and the quantum well band gap (known as detuning) made it hard for the system to maintain a high density of e-h pairs, because the recombination of electrons and holes limited the height of the electron-hole gas's Fermi-edge. Second, the thermal heating and carrier diffusion may destabilize the formation of e-h bound pairs. To address these issues, we applied a few different methods: (1) the cavity resonance was detuned to 80 meV above the quantum well band gap, to protect dense e-h carriers from radiative decay; (2) the excitation laser pulse was temporally modulated by three order magnitude smaller than the original one, in order to suppress thermal heating; (3) the excitation was spatially modulated as a flat-top beam profile in order to reduce carrier diffusion.

Besides exploring correlated e-h pairs, we would like to investigate spin dynamics. In semiconductor lasers, the spin is exploited to enhance the laser performance or applied to spintronic devices' integration. The spin-controlled semiconductor lasers, known as spin lasers, are proven to operate at the lower threshold [51, 52, 53] and to offer a larger polarization degree [54, 55, 56, 57, 58]. On the other hand, excitons, as well as exciton-polaritons, carry spin. Besides being a new candidate for spintronic devices, the spin-dependent polariton-polariton interaction enriches the physics phenomena (see review [6, 59]) such as the optical spin Hall effect [60, 61] and polarization change upon polariton-polariton scattering [62]. However, such spin interaction has rarely been discussed in terms of the aforementioned BCS-like state of e-h pairs at high density, as well as in superradiance.

Most studies of photoexcited quasiparticles in semiconductors have investigated their luminescence properties; it is rare that they explore their state before the annihilation of quasiparticles. The excitation energy is usually far above the emission level in order to prevent the excitation coherence from imprinting onto the forming correlated quasiparticles; however, exploring the dynamical

spectroscopy of correlated states becomes challenging, because pump-probe experiments require synchronized two laser-pulse systems. In this dissertation, we aim to demonstrate the realization of such pump-probe spectroscopy measurement.

1.4 Outline and results

In the next chapter, I present an introduction to the knowledge relevant to our work, including quantum well excitons, microcavity photons and exciton-polaritons (abbreviated as polaritons in the following part), and spin relaxation. I also review selective articles that are highly related to our work. In Chapter 3, I illustrate the structure and design of our microcavity sample, and detail the experimental apparatus. Chapter 4 to 7 presents the experimental results with the abstract for each chapter illustrated in the following paragraphs.

In Chapter 4, room-temperature spin-polarized ultrafast ($\sim$10 ps) lasing is demonstrated in a highly optically excited GaAs microcavity. This microcavity is embedded with InGaAs multiple quantum wells in which the spin relaxation time is less than 10 ps. The laser radiation remains highly circularly polarized even when excited by *nonresonant elliptically* polarized light. The lasing energy is not locked to the bare cavity resonance, and shifts $\sim$10 meV as a function of the photoexcited density. Such spin-polarized lasing is attributed to a spin-dependent stimulated process of correlated e-h pairs. These pairs are formed near the Fermi edge in a high-density EHP coupled to the cavity light field.

In Chapter 5, sequential lasing at two well-separated energies is observed in a highly photoexcited planar microcavity at room temperature. Two spatially overlapped lasing states with distinct polarization properties appear at energies more than 5 meV apart. Under a circularly polarized nonresonant 2 ps pulse excitation, a sub-10-ps transient circularly polarized high-energy (HE) state emerges within 10 ps after the pulse excitation. This HE state is followed by a pulsed state that lasts for 20–50 ps at a low energy (LE) state. The HE state is highly circularly polarized as a result of a spin-preserving stimulated process, while the LE state shows a significantly reduced

circular polarization because of a diminishing spin imbalance.

In Chapter 6, the observation of macroscopic harmonic states is reported in an optically induced confinement in a highly photoexcited semiconductor microcavity at room temperature. The spatially photomodulated refractive index changes (Δn) enable the visualization of sequential transit transverse modes, corresponding to harmonic states in a micrometer-scale optical potential at quantized energies up to 4 meV. We characterize the time evolution of the harmonic states directly from the consequent pulse radiation and identify sequential multiple $\sim$10 ps pulse lasing with different emitting angles, energies, and polarizations. Such a dynamic multiple-pulse lasing effect is attributed to light-induced correlated *e*-*h* pairs in a high-density plasma and their effective coupling to discrete transverse modes in the spatially photomodulated optical confinement.

In Chapter 7, the relaxation process of carriers in a high-density EHP is studied in an InGaAs/GaAs quantum-well based microcavity using optical pump-probe reflectance spectroscopic techniques. A transient optically-induced resonance appears near the cavity resonance (E_c) within 5 ps after 2 ps pulsed pump excitation with nearly 0.2 eV excess energy above E_c, and then decay slowly with a decay time constant over 500ps. The optically induced differential reflectance change $\Delta R/R$ can exceed 50%, which is three to four orders of magnitude higher than typical photomodulated reflectance measurements in GaAs-based quantum wells or vertical-cavity surface-emitting lasers. The large $|\Delta R/R|$ is the combination effect of the enhancement of optical nonlinearity due to e-h correlation and the carrier-induced refractive index change in microcavity sample. Polarization-dependent pump-probe reflectance spectra revealed a transient spin splitting up to $\sim$1 meV with a decay constant of 30 ps under a nonresonant elliptical polarized pump.

In Chapter 8, I summarize the essential research results and discuss the correlated e-h pairs issue with further perspectives on this project.

CHAPTER 2

BACKGROUND (LITERATURE REVIEW)

In this chapter, I briefly introduce a few important concepts and review relevant literature about the light-matter interacting systems. In the beginning, the exciton and microcavity photon are presented, and then followed by the introduction of the hybrid of exciton and cavity photon known as exciton-polariton. At low density and cryogenic temperature, the exciton-polaritons behaves like bosonic particles, and are predicted to behave like macroscopic state known as the polariton condensate in thermal equilibrium system or polariton laser in non-thermal equilibrium system. In section 4, the issue between conventional laser, polariton laser and polariton condensate will be discussed. In section 5, the work of the polariton control in the designed confinements is demonstrated. At high density and room temperature, the correlated e-h pairs are predicted to form in high-density EHP, and may result in superradiance. Next, I presented two distinct theories about correlated e-h pairs at room temperature, and review recent experimental work exploring the superradiance. In section 7, the spin dynamics of photoexcited carriers in the semiconductors is introduced, and the light polarization is determined by the life time and the spin relaxation time of photoexcited carriers. Finally, I illustrate the transfer matrix method, which is used in our theoretical simulation to fit the measured reflectance of microcavity sample.

2.1 Quantum well excitons

A solid normally consists of 10^{23} atoms. In order to describe the 10^{23} atoms state, a common way is to regard the stable ground state of a system as a quasivacuum and introduce quasiparticles as units of elementary excitations, which only weakly interact with each other. The quasivacuum of a semiconductor is the state of filled valence band and empty conducting band. An exciton is a quasiparticle consisting of an electron and a hole bound by Coulomb interaction $-e^2/\varepsilon r$, where ε

is the dielectric constant and r is the distance of electron and hole. The wavefunction of exciton can be analogous to Hydrogen atom. Due to the strong dielectric screening and a small effective mass ratio of the hole to the electron, the binding energy of exciton is about 10 – 100 meV. Its Bohr radius is about 10 – 100 Å, the size of an exciton extends over tens of cells in the semiconductor. The exciton can be considered as bosons when the exciton interparticle spacing is much larger than its Bohr radius.

A semiconductor QW is a thin layer of a semiconductor with small thickness sandwiched between two barrier layers with larger band gap. The thickness of the middle layer in design is normally comparable to exciton Bohr radius. The reduced dimension resulting in quantum confinement leads to exciton properties with larger binding energy and smaller Bohr radius.

2.2 Microcavity photons

There are various ways of cavity design to confine photons in a local area, and here we introduce one particular cavity: distributed Bragg reflector (DBR) based semiconductor microcavity. The structure of this kind of cavity is shown as Fig. 2.1, which contains cavity barriers with emitter such as QW sandwiched by two DBRs. The DBR is composed of alternative two-layer materials, and each thickness of the individual layer is chosen to match the Bragg condition $d = \lambda_c/4n_i$. The λ_c is cavity resonance wavelength; n_i is the refractive index of that materials at λ_c. In such design, the interference of transmitted and reflected light leads to excellent high reflectivity in a spectral window of width about 100 nm, which symbolic reflectance spectrum is shown in Fig. 2.1 (b).

The optical mode profile (the dip of reflectance in Fig. 2.1 (b)) in such Fabry-Perot resonator can be determined by transfer-matrix method, which the light intensity is enhanced significantly inside cavity barrier but decays inside the DBR mirrors. From the calculation and the decay in reference [63], we can define an effective cavity length as: $L_{eff} = L_c + \frac{\lambda_c}{2n_c}\frac{n_1 n_2}{|n_1 - n_2|}$, where L_c is the physical length of cavity, n_1 and n_2 are refractive index of layers in DBR, and n_c is refractive index of the cavity layer.

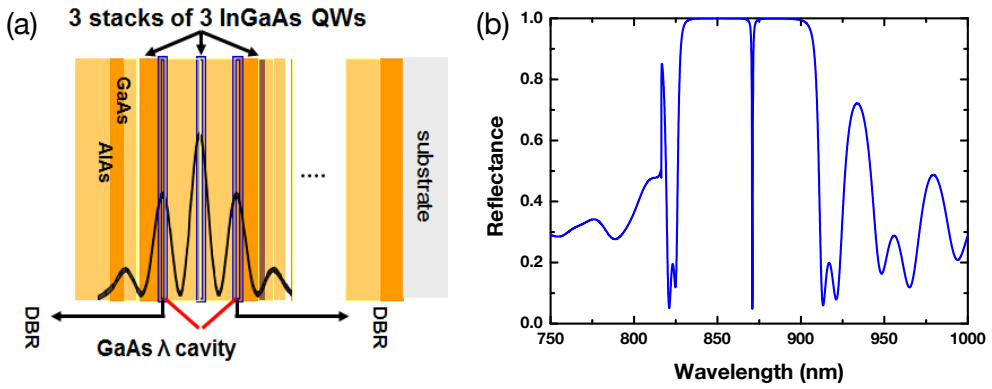

Figure 2.1 **Planar semiconductor microcavity.** (a), Schematic of planar semiconductor microcavity, which typically consists of multiple quantum wells (MQWs) sandwiched by two distributed Bragg reflectors (DBRs). The DBR is multiple pairs of two layer materials, the thickness of individual layer satisfies $d = \lambda_c/n_i$, where λ_c is the optical mode in the cavity. (b) Schematic of typical reflectance of a DBR-based semiconductor microcavity. The width of high reflectivity is stopband, while the dip within stop band is the cavity photon mode.

The microcavity is normally not perfect, so the resonant photon may leak off the cavity. The quality of cavity can be quantitatively described by Q-factor via $Q = \omega/\delta\omega$, where ω is the frequency of optical mode, and $\delta\omega$ is the linewidth of resonant optical mode. This Q-factor relates the lifetime τ of cavity photon by $Q = \omega\tau$.

Since the photon can not propagate freely inside the cavity, the dispersion of photon is strongly modified. In a condition of small in-plane momentum $k_{\|}$, the dispersion relation is approximately described by a parabolic shape with an effective photon mass m_c:

$$E(k) \approx E_0 + \frac{\hbar^2}{2m_c}k_{\|}^2 \tag{2.1}$$

The effective mass is defined as: $m_c = \frac{hn_c}{cL_c}$, which is on the order of 10^{-5} of free electron mass m_0.

2.3 Exciton-polaritons

For a semiconductor microcavity implemented by QW with high oscillator strength, if cavity photon mode can couple to exciton in the QW resonance with satisfied condition: the energy exchange

rate between exciton and cavity photon exceeds the exciton decoherence rate and photon leakage. The result gives the Rabi oscillation in a time domain, leading to a normal mode splitting of polariton branches. The energy-momentum ($k_{\|}$) dispersion of polariton is similar to resolve coupling two-level system, which Hamiltonian is [6]:

$$\begin{aligned}\hat{H}_{pol} &= \hat{H}_{cav} + \hat{H}_{exc} + \hat{H}_I \\ &= \sum E_{cav}(k_{\|})\hat{a}^{\dagger}_{k_{\|}}\hat{a}_{k_{\|}} + E_{exc}(k_{\|})\hat{b}^{\dagger}_{k_{\|}}\hat{b}_{k_{\|}} + \sum g_0(\hat{a}^{\dagger}_{k_{\|}}\hat{b}_{k_{\|}} + \hat{a}_{k_{\|}}\hat{b}^{\dagger}_{k_{\|}})\end{aligned} \tag{2.2}$$

Here $a^{\dagger}_{k_{\|}}$ and $b^{\dagger}_{k_{\|}}$ are creation operators of photon and exciton, respectively. E_{cav} and E_{exc} are energy of cavity photon and QW exciton. g_0 is the exciton-photon dipole interaction strength. The Hamiltonian $\hat{H_{pol}}$ can be diagonalized with transformation:

$$\begin{aligned}\hat{P}_{k_{\|}} &= X_{k_{\|}}\hat{b}_{k_{\|}} + C_{k_{\|}}\hat{a}_{k_{\|}} \\ \hat{Q}_{k_{\|}} &= -C_{k_{\|}}\hat{b}_{k_{\|}} + X_{k_{\|}}\hat{a}_{k_{\|}}\end{aligned} \tag{2.3}$$

The $X_{k_{\|}}$ and $C_{k_{\|}}$ are coefficients satisfying $\left|X_{k_{\|}}\right|^2 + \left|C_{k_{\|}}\right|^2$. The $\hat{H}_{pol}$ becomes:

$$\hat{H}_{pol} = \sum E_{LP}(k_{\|})\hat{P}^{\dagger}_{k_{\|}}\hat{P}_{k_{\|}} + \sum E_{UP}(k_{\|})\hat{Q}^{\dagger}_{k_{\|}}\hat{Q}_{k_{\|}} \tag{2.4}$$

Here $(\hat{P}_{k_{\|}}, \hat{P}^{\dagger}_{k_{\|}})$ and $(\hat{Q}_{k_{\|}}, \hat{Q}^{\dagger}_{k_{\|}})$ are the creation and annihilation operators of eigenstates of the system. These eigenstates are called lower exciton-polariton and upper exciton-polariton corresponding to their energy:

$$E_{LP,UP}(k_{\|}) = \frac{1}{2}\left[E_{exc} + E_{cav} \pm \sqrt{4g_0^2 + (E_{exc} - E_{cav})^2}\right] \tag{2.5}$$

The dispersion of cavity photon $E_{cav}(k_{\|})$ is parabolic shape, and the $E_{exc}(k_{\|})$ is normally flat in small $k_{\|}$, thus the dispersion of typical exciton-polariton can be referred to Fig. 2.2.

In Fig. 2.2, the dispersion of polaritons are closed to parabolic curve with finite curvature, this curvature corresponds to an effective mass of the quasiparticle. The effective mass of exciton-polariton is typically in a order of 10^{-1} – 10^{-4} m_0. The Exciton-polariton has finite lifetime due

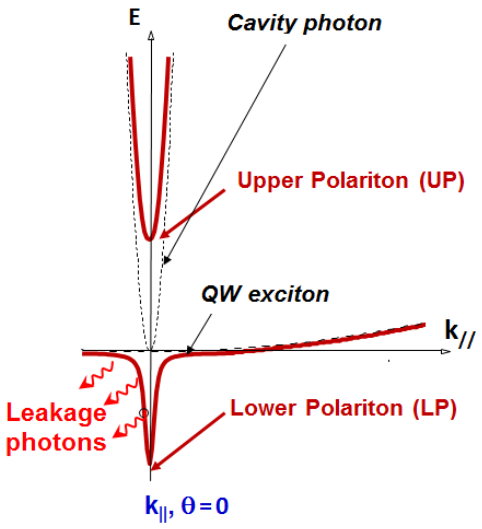

Figure 2.2 **Dispersion of exciton-polariton.** The dashed curves with large and small curvature are the dispersion of cavity photon mode and quantum well (QW) exciton. As cavity photon and QW exciton are in the strong coupling region, new eigenstates of the system appear shown as red curves, they are lower and upper exciton-polariton corresponding to lower and upper branches. The exciton-polariton has a finite lifetime and radiatively decay to photon due to the recombination of electron and hole. The photon carries information of energy and in-plane momentum, which can be detected in the experiment.

to recombination of electron and hole from the excitonic part, which the lifetime is typically about 1 – 10 ps at the bottom of branches.

The spectral properties of exciton-polariton like energy-momentum dispersion can be measured by angle-resolved photoluminescence. In the experiment, the semiconductor microcavity is optically pumped at a high energy to produce lots of free e-h pairs. These e-h pairs are cooling in energy through carrier-phonon scattering and populate at the polariton state. The polaritons can relax energy by two ways. One is through exciton-photon interaction through emitting optical or acoustic phonon, another is via Coulomb interactions with other polaritons or with free carriers in the system. The photoluminescence dynamics is determined by energy relaxation rate and spontaneous emission rate. If the energy relaxation rate is slower than the polariton emission rate, then the relaxation of polaritons to the lowest state is suppressed, and radiative decay occurs at higher energy with finite $k_{||}$. This phenomena is known as relaxation bottleneck. The leakage photon from

	Alkali Gas	Exciton (X)	X-polariton
m^*/m_0	10^3	0.1 – 1	$10^{-1} - 10^{-4}$.
Bohr radius (nm)	0.1	10	$10 - 10^3$
Spacing $n_c^{-1/3}(nm)$	$\sim 10^2$	$10 - 10^2$	$10^2 - 10^3$
T_c	$1nK - 1\mu K$	1 mK – 1K	1 – 300 K
Thermalization	1 – 10 ms	10 – 100 ps	1 – 10 ps
Lifetimes	1 – 100 s	1 – 100 ns	1 – 10 ps

Table 2.1 **Parameter comparison of bosonic quasipartilces**

the recombination of electrons and holes reveals the information of energy and $k_{||}$ of the polaritons.

2.4 Polariton lasing and condensation

Similar to exciton, the exciton-polariton can be regarded as a boson in a low-density limit. Due to light effective mass of these particles, they are predicted to form bosonic condensation with elevated temperature in the semiconductors. The table 2.1 shows the comparison of few important parameters in Bose-Einstein condensation for Alkali gases, excitons, and exciton-polariton.

The potential candidate of BEC at room temperature leads numerous research involving this topic, but a few considerations should be deliberated: (1) Polariton lifetime in a microcavity is typically short as 1 – 10 ps, which is comparable to thermalization time. Therefore, the condensation of exciton-polariton is referred to as a dynamical open-dissipative condensation, or a "polariton-laser". There is some debate whether the polariton achieves the thermal equilibrium to form a condensate, and the comprehensive discussion between the condensate and the polariton laser can be seen in reference [64]. (2) At high density, the screening effect of exciton becomes significant and attenuate the oscillator strength, leading the system to plasma phase. The transition density is on the order of Mott transition about $10^{10} - 10^{11}$ e-h pairs per cm^{-2}. (3) With increasing temperature, the thermal energy exceeds the binding energy of exciton, leading to instability of exciton in the system.

The exciton-polariton in a planar semiconductor microcavity is equivalent to a two-dimensional system. An uniform 2D system of bosons have BEC transition only at zero temperature in the

thermodynamic limit because long-wavelength fluctuations destroy the long-range order. However, such system with finite size restrains the density and phase fluctuation, allowing the formation of condensate at finite temperature. The long-range spatial and temporal coherence of polariton condensates has been demonstrated, revealing the signature of BEC [65, 66]. Generally speaking, the coherence length of polariton condensate is finite, and ranges on the order of optical pumping spot size.

The macroscopic population of coherent polariton could give cooperative radiation, resulting in polariton lasing. A rising question is how to make polariton populate effectively at one state with the key being the "final state stimulation". The final-state stimulation is a distinct feature of a system with identical bosonic particles, which describes the scattering rate into a particular state is proportional to N+1 if there is N-particle accumulate at that state. In conventional lasers, such stimulation of photons is essential to the lasing mechanism behind. Similarly, the final state stimulation enhances the polariton-polariton scattering, giving potential accumulation at the bottom of the lowest polariton branches. The early reports on polariton lasing from $k_{||}$ have been demonstrated on GaAs-based device [17, 19], CdTe-based devices [20] and GaN-based [43] devices.

These polariton lasers share few characteristics: (1) In an input-output relationship (pump intensity vs. emission intensity), the emission flux with increasing pump flux shows a sharp superlinear increase around the threshold density P_{th}. The corresponding injected density in QW at P_{th} is about two orders of magnitude than the Mott density. (2) The energy-momentum dispersion below P_{th} is measured with an agreement of LP dispersion instead of cavity-photon dispersion. (3) With increase pumping density starting from P_{th}, but keeping polaritons from being destroyed, the lasing exhibits energy blue-shift accompany with linewidth broadening. [20, 67, 19, 35, 26] These phenomena are attributed to polariton-polariton interaction, which mostly results from Coulomb exchange interaction and is a repulsive force.

Although photon laser and polariton laser system all initiate lasing with the final-state stimulation, their mechanisms are quite different as illustrated in Fig. 2.3. In photon laser system, the lasing emission results from the stimulation emission of the photon into cavity modes with occu-

pation number larger than 1. It requires electrons and holes staying at metastable states to build electronic population inversion before stimulation emission. In polariton laser system, the lasing is trigger by bosonic stimulation of polaritons, and lasing energy is not restricted to cavity modes. This also explains why the energy of polariton laser shifts instead of a constant with increasing pump flux. Normally, the threshold density is on the order of $\sim 1/\lambda_T^2$ (λ_T is the de-Broglie wavelength of polariton), and about three to four order of magnitude lower than that of a conventional laser threshold.

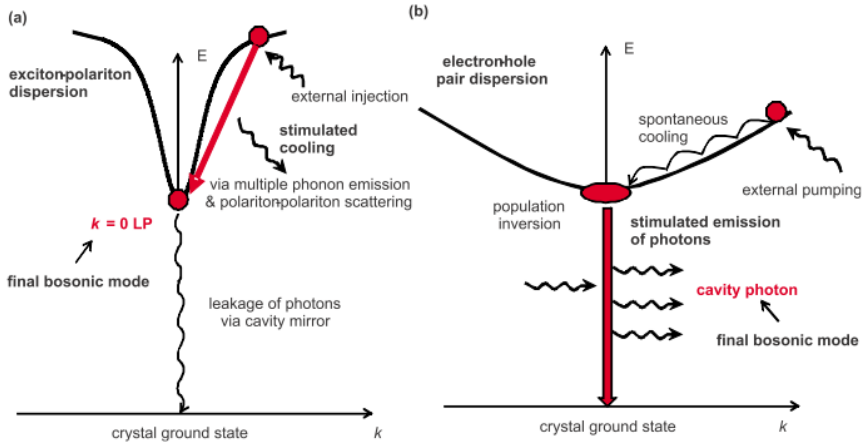

Figure 2.3 **Polariton lasing vs. photon lasing.** The diagram demonstrates the operational principle of polariton lasing (left) and photon lasing (right), and they normally are operated at quite different carrier density regimes. In polariton laser system which e-h density is about $10^{11} - 10^{13}\,cm^{-3}$, the generated exciton-polariton falls onto the lower dispersion branch at finite in-plane momentum $k_{||}$, then relaxes to lowest energy state $k_{||} = 0$ by stimulated cooling via multiple phonon emission or polariton-polariton scattering. A macroscopic population of polariton at the bottom of dispersion cooperative decays to radiation through e-h recombination. Therefore, the polariton lasing is not locked to cavity photon mode. In photon laser system which e-h density is about $10^{16} - 10^{18}\,cm^{-3}$, the injected electron-hole pairs relax to the bottom of cavity dispersion through spontaneous cooling and build up a population inversion. Once the cavity photon triggers the stimulated emission, the bunch of e-h pairs recombine to coherent radiation. This figure is adapted from [6]

The photon lasing and polariton lasing sometimes are classified into weak coupling region and strong coupling region, respectively, and they can be measured in the same sample structure. In reference [18], two lasing thresholds with distinct lasing energy are observed with increasing pump flux. They attributed the first lasing is polariton laser. As injected density continuously increases,

the saturation of 2D carrier density diminishes the polariton, making the system undergo a transition to weak coupling and then give photon lasing radiation. In reference [68], they claimed to observe the crossover between photon and exciton-polariton lasing in a semiconductor microcavity. In this research, they non-resonantly pumped the microcavity and performed energy-, time- and angle-resolved measurement to characterize the transient carrier distribution and effective temperature. Under high injected density, the lasing commences at the bottom of cavity dispersion, but 50 to 100 ps later the main lasing energy red shift toward the bottom of lower polariton branch.

2.5 Polaritons in potential landscapes

Trapping is a useful tool both in physics research and in industrial application. In physics, it helps with observing quantum many-body physics, like the early realization of BEC in atomic gases. In application, the confinement in microcavity enhance the lasing efficiency and lasing threshold reduction. In polariton system, the confinement is not necessary to observe the in-plane polariton condensate, but engineering polariton confinement can study the interactions and the transport of tailored polaritons in a complex environment. The study of polaritons with the engineering confinements can emulate many-body phenomena in another system such as the physics in high-temperature superconductors, graphene or frustrated spin-lattices [69, 70, 71]. On the other hand, the engineering polariton trapping enables to control the flow of polariton, which can be exploited to optoelectronic devices like photonic integrated circuits and logic elements [72, 73]. The exciton-polariton is constituted of light and matter, and both parts can be subjected to the confinement. In this section, we briefly review few articles of polariton in the potential landscapes. We will highlight a few characteristic of polariton lasing behaviors.

The simple way to trap the polariton is taking advantage of the ubiquitous defects in semiconductor microcavities [30, 31]. The size of the defect is around few to tens micrometers square. Under nonresonant excitation, a sequential lasing modes may appear with an order of energies

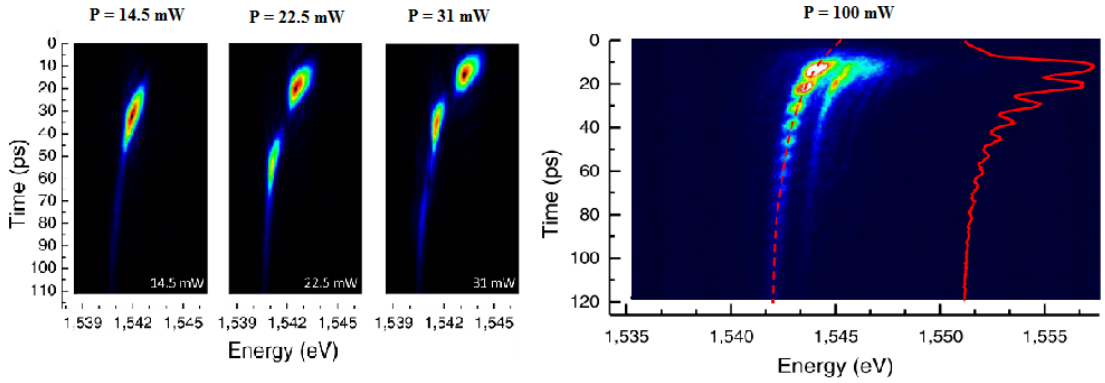

Figure 2.4 **Polariton in natural trap.** The experiment [31] was carried out in an $Al_{0.15}Ga_{0.85}As/AlAs$ microcavity. The exciton-polaritons were generated from a non-resonant pumping, and then form a condensate confined in a natural trap with size of 1 to 10 μm^2. The image shows the spectral- and time- resolved luminescence with increasing pump power. Sequential multiple lasing modes appear at high pump power, and may have oscillation effect. This figure is adapted from [31]

from high to low at pump flux much above the lasing threshold shown in Fig. 2.4 (c–e). At higher excitation power, the lasing may appear as an oscillation in a suitable size of the defect shown in Fig. 2.4. The sequential lasing modes with oscillation were attributed to the interplay between reservoir feeding and Bose stimulation. Namely when the polaritons form a condensate through bosonic stimulation and decays with cooperative radiation, the excitons in the trap are depleted. Later on, the excitons in neighboring place will replenish the trap, helping with the building of critical density again for the next lasing radiation.

One common way to create a confinement is taking the advantage of structure or engineering a designed trap. In the reference [36], they optically pumped a nanowire and controlled the trapping size by translating the position of excitation along the nanowire direction shown in Fig. 2.5. When the distance between the excitation and the edge of the nanowire is short enough, quantized lasing modes would appear in real space. Another example of fabricating trapping is to create a mesa in a semiconductor microcavity shown in Fig. 2.6. In the figure, the mesa has 9 μm diameter with 6 nm height. Around the energy 1.480 eV, discrete lasing modes commence both in the real and the momentum space. These lasing modes demonstrate discrete energies and the mode-number change

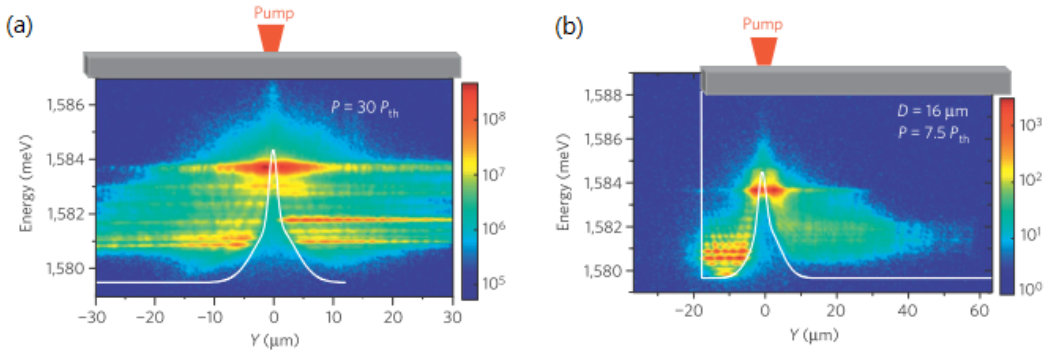

Figure 2.5 **Polariton trapped in nanowire.** In the experiment [36], a GaAs-based wire microcavity (gray bar) was optically non-resonant pump at different position. The edge of wire cavity and pump forms a confinement for the forming exciton-polaritons, and the size of confinement was controlled by the position of pumping. This figure is adapted from [36]

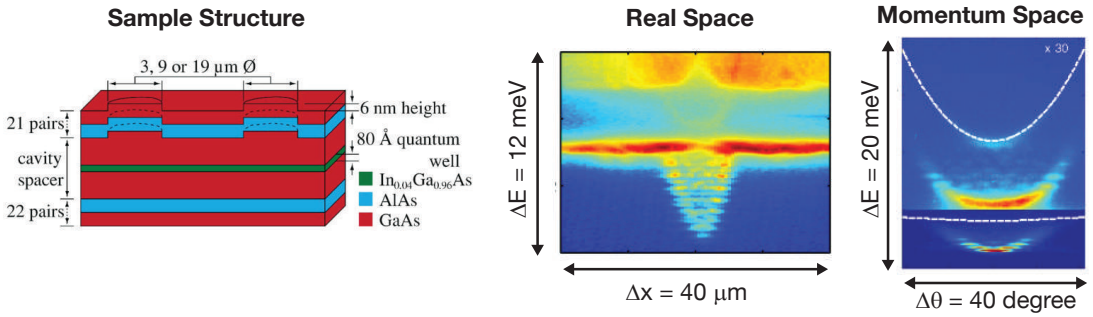

Figure 2.6 **Polariton trapped in a mesa of semiconductor microcavity.** The sample structure is a semiconductor microcavity with some mesa on the top DBR. Along the z-axis (perpendicular to cavity surface) the polaritons form interference in such confinement shown as in real space and momentum space. This figure is adapted from [36]

depending on the size of the mesa. In these two examples, the polaritons' spatial distribution in the confinement cab be deduced by solving the Schrodinger equation of quantum harmonic oscillators. However, the drawback of these two cases is that the confinement can not be controlled since the sample structure is fixed after the manufacture.

The optical potential has been popular for the study of particles in a potential because the size and the shape of the confinement can be flexibly controlled by lasers. With the advance technique of spatial light modulator, the optical potential design stimulates extensive investigations in the exciton-polariton field [39, 40, 41, 42]. In these reports, multiple polariton spots are created

by non-resonant optical pumping with a designed shape, and these polariton condensates in the microcavity are used to visualize the formation of spontaneously oscillating quantum fluid. The quantum fluid forms different interference patterns both in the real and the momentum space. These patterns are determined by the interaction of quasiparticles in the confinement, and its shape and the size are changed depending on the pump power as well as the confinement shape.

In chapter 6, we will demonstrate the macroscopic harmonic state in an optically induced confinement at room temperature. The previous investigation aforementioned have intensively explored the image in the real and the momentum space, but the lasing behavior in spectral- and time-resolved analysis have been rarely studied. In our project, we will present more comprehensive study not only on the spectroscopy in the real and the momentum space, but also the issue of the dynamics and polarization of luminescence from the sample.

2.6 Correlated electron-hole pairs at large density

The previous sections illustrate possible formation of quasiparticle condensate at cryogenic temperature. With increasing e-h density, exchange effects and the screening of the Coulomb interaction in e-h pairs destabilize the exciton and an EHP forms. However, some theorists use mean field theory to predict that the paired electrons and holes may form BCS-like state near the Fermi-edge. These e-h pairs are quite similar to the Cooper pairs in a superconductor at cryogenic temperature [13]. The correlation of e-h pairs might be enhanced by a presence of light field [50]. Recently, there was another report arguing that an energy level of bound e-h pairs at the band gap of the semiconductors exists in the large density EHP [49].

In the experiment, the build-up of macroscopic electric dipole under incoherently excitation can result in cooperative decay, giving known as superfluorescence or superradiance. This superradiance can even happen at large e-h density. Although superradiance is coherent emission resembling photon lasing, the dynamics of superradiance is quite different from that of conventional lasers.

In this section, I will illustrate the mean field theory of excitons, which deduces the BCS-like

state near the Fermi edge. Next, I briefly introduce the second theory that correlated e-h pairs form at the band gap of the semiconductors. Finally, I present the characteristics of superradiance and a few remarks of the relevant work.

2.6.1 Mean field theory for excitons

In this subsection, I will present the mean field theory about how e-h pairs form near the Fermi-edge of EHP. In the beginning, We first define the Hamiltonian in e-h system:

$$H = H_0 + H_C \tag{2.6}$$

where

$$H_0 = \sum_k [\varepsilon_{ck} a^\dagger_{c,k} a_{c,k} + \varepsilon_{vk} a^\dagger_{v,k} a_{v,k}] \tag{2.7}$$

$$H_C = \frac{1}{2} \sum_q [V^{ee}_q \rho^e_q \rho^e_{-q} + V^{hh}_q \rho^h_q \rho^h_{-q} - 2V^{eh}_q \rho^e_q \rho^h_{-q}] \tag{2.8}$$

$a^\dagger_{c,k}$ and $a^\dagger_{v,k}$ are creation operators for electrons in the conducting and valence band, respectively. ρ^e_q and ρ^e_h are density operators with the forms: $\rho^e_q = \sum_k a^\dagger_{c,k+q} a_{c,k}$ and $\rho^h_q = \sum_k a^\dagger_{v,k+q} a_{v,k}$. V^i_q is Coulomb interaction and for homogeneous three-dimension system $V^{ee}_q = V^{hh}_q = V^{eh}_q = 4\pi/\varepsilon q$. For parabolic bands, $\varepsilon_c(k) = \hbar^2 k^2/2m_e$ and $\varepsilon_v(k) = -E_g - \hbar^2 k^2/2m_h$.

The mean field theory starts from the following ansatz for the ground-state of the interacting electron and holes:

$$|\Psi_{MF}\rangle = \prod_k [u_k + v_k a^\dagger_{e,k} a_{v,k}]|0\rangle \tag{2.9}$$

Here $|0\rangle$ is vacuum state of the system, which the conducting bands are empty but valence bands are full. u_k and v_k are complex coefficients with relation $|u_k|^2 + |v_k|^2 = 1$, and the $|v_k|^2$ is equivalent to occupation number of e-h pairs in momentum k. The determination of u_k and v_k is to minimize the expectation value of Coulomb interaction term H_C in equation 2.6.

Next we will determine the equations of these parameters when the system is at equilibrium. Suppose the e-h density is $\langle n \rangle$ with the corresponding chemical potential μ, the free energy of the

system is:

$$F = \langle H_0 + H_C \rangle - \mu \langle n \rangle \tag{2.10}$$

The equilibrium of the system occurs when the free energy is minimal, that is $\partial F / \partial v_k = 0$. Considering only s-wave pairing is dominate in the system, a set of self-consistent equations can be obtained in the following:

$$\xi_k = \varepsilon_k - \mu - 2\sum_{k'} V^{ee}_{k-k'} n_{k'} = \varepsilon_k - \mu - \sum_{k'} V^{ee}_{k-k'}(1 - \xi_{k'}/E_{k'}) \tag{2.11}$$

$$\Delta_k = 2\sum_{k'} V^{eh}_{k-k'} \langle a^{\dagger}_{c,k} a_{v,k} \rangle = \sum_{k'} V^{eh}_{k-k'} \Delta_{k'}/E_{k'} \tag{2.12}$$

$$E_k^2 = \xi_k^2 + \Delta_k^2 \tag{2.13}$$

$$v_k^2 = \frac{1}{2}\left(1 - \frac{\xi_k}{E_k}\right)$$

$$u_k^2 = \frac{1}{2}\left(1 + \frac{\xi_k}{E_k}\right)$$

$$u_k v_k = \frac{\Delta_k}{2E_k} \tag{2.14}$$

Here the equation 2.11 describes the renormalized single-particle energy ξ_k per pair measured from the chemical potential, where $\varepsilon_k = \frac{\hbar^2 k^2}{2m_e} + \frac{\hbar^2 k^2}{2m_h}$. Equation 2.12 illustrates the "gap equation", which is similar to the one in BCS theory in superconductors. Δ_k represents the gap function and is also known as the order parameter. The order parameter Δ exists only when both u_k and v_k are non-zero for some overlapping range of momenta k, and it also symbolizes the overall degree of phase coherence. In equation 2.13, E_k is the pair-breaking excitation spectrum, which can be viewed as the energy cost of breaking one e-h pair in the condensation and placing it in an available state of momentum k. Equation 2.14 describes the coefficients of v_k and u_k as the function of E_k and Δ_k.

In the following I will discuss the state of system with different region of e-h pair density $\langle n \rangle$:
1. The density $\langle n \rangle$ is infinitesimal, that means the isolated excitons overlap very little. Hence the parameters of occupation are $v_k \ll 1$ and $u_k \approx 1$. In this limit, the chemical potential μ (measured from the bottom of the combined electron and hole bands) is negative and its magnitude approaches

to 1 Ryd, where Ryd is the binding energy of e-h pair. The lowest excitation occurs at k = 0, which corresponds to ionization of exciton into the free electron and hole.

2. As the e-h density $\langle n \rangle$ approaches to infinity, the kinetic energy of electron and hole dominates the interaction energy, and most of the k-states are occupied. We expect v_k is a step function like $v_k = \Theta(|k| - k_F)$, where k_F is the Fermi momentum. The wavefunction will approximately be:

$$|\Phi_{MF}\rangle_{n\to\infty} \to \prod_{|k|<k_F} a^{\dagger}_{c,k} a_{v,k} |o\rangle \tag{2.15}$$

Here the chemical potential is close to the Fermi energy. In the extreme limit that $n \to \infty$, the order parameter doesn't exist.

3. The density $\langle n \rangle$ is finite, the model can be elaborated as Fermi surface instability with more description in the following. The electrons and holes near the bottom of the Fermi sea are almost fixed due to the large density and Pauli exclusion. However, the state closed to the Fermi surface can suffer Coulomb interaction and produces a small fraction of the occupation number above the Fermi energy. The electrons and holes near the Fermi energy have more freedom for the density of state and may form e-h pairs. The binding energy of the pairing is equivalent to the order parameter Δ_k, which is quite small compared to μ or Fermi energy. The Δ_k is also the minimal excitation energy to break the e-h pairs.

Although above model is based on a three-dimensional system, quite a few theories predict that the BCS-like state could realize in a two-dimensional system such as in the QWs [13, 12]. One claimed that "The quantum confinement enhances the e-h correlation both in the atomic exciton limit and in the weak-coupling plasma limit" [13]. The absorption and gain spectra, which are calculated based on solving the Bethe-Salpeter equation of the e-h pair propagator, deviate significantly from the corresponding spectra in the free-particle system. These deviation is enhanced near the quasichemical potential μ and red shifts in energy due to the renormalization of the single particle energy [12].

A remark is pointed out by Guseinov and Keldysh that the BCS-state in an equilibrium sys-

tem behaves no difference from a normal dielectric or charge-density wave system. However, in a non-equilibrium situation, where the electron and hole populations are maintained with two different quasi-chemical potentials, the recombination will require not only tunneling but also the emission of a photon. The decay process due to the recombination will break the coherence of e-h pairs, leading to a cooperative radiation known as superradiance phenomenon. I will introduce the superradiance in the last subsection.

2.6.2 Condensation of electron-hole pairs at band gap

Normally the many body effect are commonly used in many theories to explain those experimental results in large-density EHP system that cannot be explained by free carriers calculation or conventional lasers theory. One popular theory aforementioned predicts the formation of the BCS-like state near the Fermi surface at cryogenic temperature. But this model is hardly applied on the system at room temperature because the binding energy or the correlated e-h pairs 1–2 meV is much smaller compared to the thermal fluctuation at room temperature ($\sim 25meV$). Here I introduce another theory [49] predicting the existence of bound e-h pairs in a large-density semiconductor EHP at room temperature. The energy level of such bound e-h pairs is at the band gap of the semiconductors instead of near the Fermi-surface in aforementioned theory. In the following, I will briefly introduce the mechanism of the "condensate", and present how these bound e-h pairs stably exist at room temperature.

Here I present the conceptual mechanism of condensation, which the correlated e-h pairs form at the bottom of the semiconductor band gap E_g. In the model, it assumes that an electron and hole are attracted by the Coulomb force and move in a mean field of other particles and lattices. Spin states are neglected. The Coulomb interaction is screened with the Thomas-Fermi wave number k_{TF}. Fig.2.7 is the band structure diagram of a semiconductor with degenerate large-density EHP. In such a system, most states below Fermi-surface are filled up due to large density and Pauli exclusion. Now if a light field is resonant with E_g, such resonant electromagnetic field can enhance the correlation of electrons and holes. Occasionally the correlated bound states are generated from

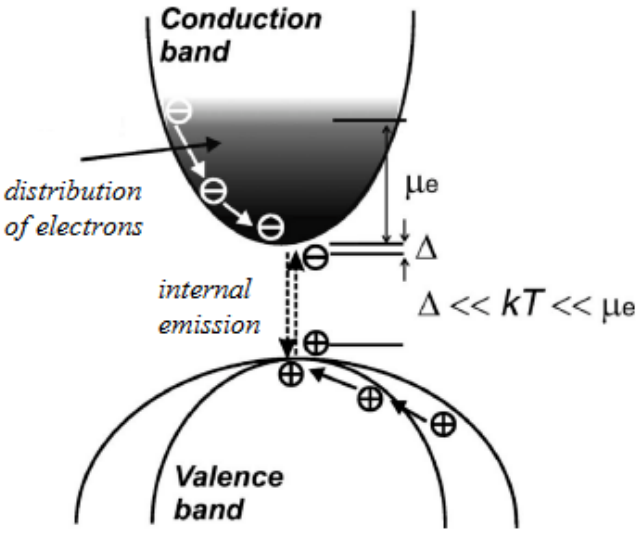

Figure 2.7 **Schematic of e-h condensation at band gap.** A condensate of e-h pairs form near the band gap with an assistance of light. The initial vacancy for formation of e-h pair will be replenished quickly from electrons and holes at upper band. The binding energy Δ is normally smaller than the thermal energy kT at room temperature, and kT is much smaller This figure is adapted from [49]

a fraction of electrons and holes near E_g, the energy of bound state is slightly lower than E_g due to binding energy Δ. After the formation of bound states, the vacancy of their initial state will be replenished by higher energy state quickly.

The binding energy of correlated e-h pairs is too large to be destroyed by thermal energy. The energy required to break the pairing of correlated bound states is equivalent to the excitation energy from the bound state near E_g to the free electrons and holes above the Fermi-surface. The excitation energy is typically more than 30 meV, so the internal fluctuation such as thermal energy hardly destroys the bound e-h pairs. The critical temperature T_C of transition is typically defined as the thermal energy diminishing the pairing, so in this model the T_C is determined by the chemical potential μ rather than related to order parameter Δ developing in BCS theory for superconductors.

In the reference [49], they further determine the probability of transition for destructing e-h pairing. The destruction of e-h pairs occurs due to collisions with optical phonons with simultaneous transitions of electrons and holes to state with larger energies. The authors used GaAs material to give an quantitative example. The energy of optical phonon in GaAs is $\hbar\Omega \approx 36 meV$,

and is almost constant for all phonons having wave number about $k_F \sim 10^7\, cm^{-1}$. Among the density $2-6\times 10^{18}\, cm^{-3}$ at room temperature, the destruction probability is less than 0.3. This result implies considerable density of correlated e-h pairs might stay for a while until they undergo cooperative decay to coherent radiation.

2.6.3 Review of superradiance

In quantum optics, superradiance is a phenomenon of a cooperative radiation produced from a group of N emitters (such as excited atoms) coupling with each other by means of photon exchange. The condition is fulfilled when the wavelength of the light is much greater than the separation of the emitters. The original idea was proposed by Dicke in 1954. However, the concept of superradiance has not only been extensively studied in the quantum optics field, but also applied in a variety of system including the quantum phase transition.

The system discussed in the following is focused on an optically created EHP in a semiconductors. In recent research [14, 15, 16], the ultradense EHP created by femtosecond laser pulse would give an ultrashort burst of coherent radiation upon a certain time delay after excitation, and such emission has a much higher intensity than the spontaneous emission of the same number of e-h pairs. In these experiments, the giant pulses of light is generated by a macroscopic dipole emitters developed from an non-resonant optical excitation and abrupt energy relaxation of e-h pairs.

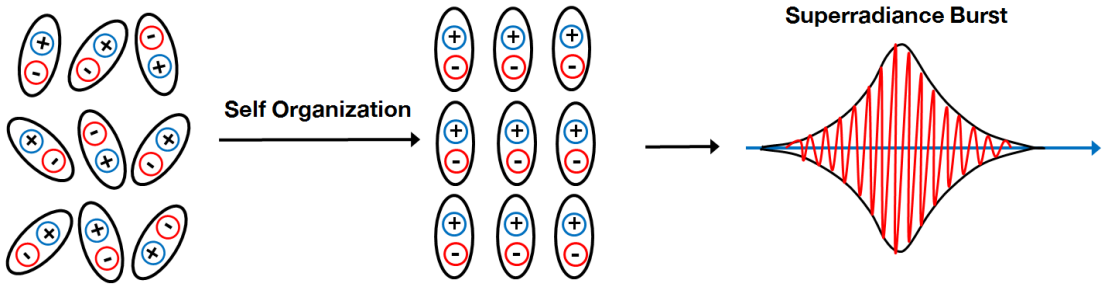

Figure 2.8 **Schematic of superradiance.** The photoexcited electric dipoles are incoherent in the beginning, but will self organize to form a collective state, resulting in superradiance burst. This figure is adapted from [14]

The unique characteristics of superradiance distinguished from another coherent light emis-

sion process are the existence of self-organization stage to spontaneously build up a macroscopic coherence (see Fig. 2.8). The self-organization coherence in phase manifests itself physically as a delay between the excitation and emission pulses. It is pure quantum mechanics driven by the quantum fluctuation in the system. Fig. 2.9 illustrates the typical dynamics of superradiance. Below the critical e-h pair density N_c, the emission rises up to the peak proportional to N, the number of the excited dipole in the ensemble, then exponentially decays with a time constant T_1. As the density exceeds N_c, a giant burst commences with a time delay after excitation. Its intensity peak in the time domain is proportional to N^2 with pulse width inversely proportional to N. After the first burst, a second pulse emission may occasionally commence depending on the density.

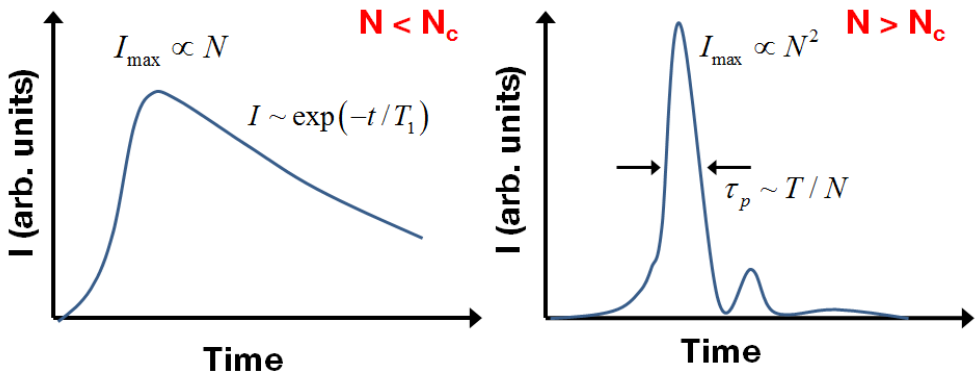

Figure 2.9 **Symbolic dynamics of superradiance.** A hand drawing describing the typical dynamics of superradiance. As dipole number N below N_c, the emission is a exponentially long decay with a time constant T_1. The peak of intensity is proportional to N. As N exceeds N_c, a giant burst pulse commences with a time delay after excitation. The peak intensity is proportional to N^2 but the pulse width is inversely proportional to N. A second pulse may appear after first pulses depending on the density. This figure is adapted from [14]

The sample in the series studies [14, 15, 16] was a stack of fifteen undoped QWs consisting of 8 nm $In_{0.2}Ga_{0.8}As$ wells and 15 nm GaAs barriers. The quantum confinement leads to quantized subbands for electrons in conducting band and holes in valence bands. The strain in their sample resulted in a large splitting of the heavy hole and light hole states, but only the heavy-hole states are relevant to the study. The optical excitation energy is chosen as 1.55 eV above the band gap of the GaAs barriers. Both the electrons and holes experience many scattering before relaxing into

QWs to form two-dimensional excitons.

As a giant pulse commences at pump flux larger than P_c (corresponding to critical dipole number N_c in Fig. 2.9), the emission characterized in spectral- and time- resolved measurement demonstrates the superradiance decays with energy relaxation in time domain at cryogenic temperature ($\sim 20K$) (see Fig. 2.10). The energy shift is about 13 meV, and the emission appears 50 ps after excitation and lasts more than 150 ps. The radiation intensity is enhanced with increasing pump flux but decreases with increasing temperature. The emission almost fades out at temperature above 150 K.

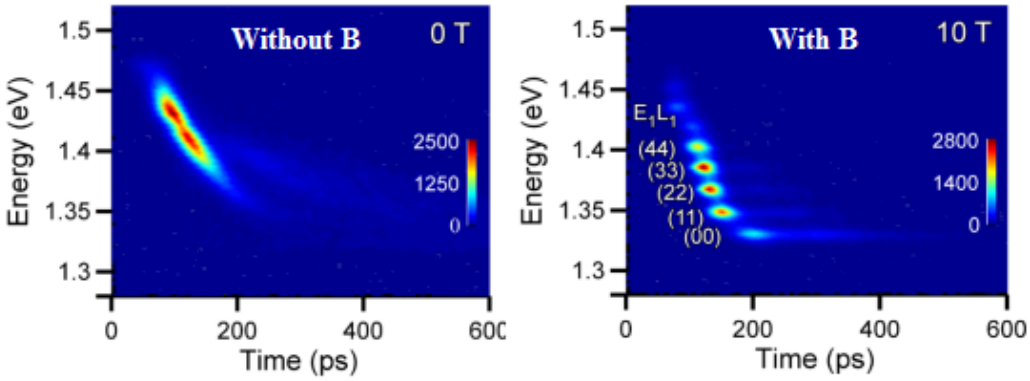

Figure 2.10 **Superradiance in QW with the magnetic field.** The image demonstrates superradiance from semiconductor quantum wells in the condition of without and with the magnetic field (B-field). Without B-field, the dynamical spectroscopy of luminescence is long-tail in time- and spectral- resolved image. With B-field, luminescence image transforms into discrete modes with envelope like a long tail. This figure is adapted from [16]

With the presence of magnetic field (B-field) along the confinement direction of QW, the emission image on energy-time diagram transforms from a continuous long tail to multiple lasing modes and each mode carries a tail (see Fig. 2.10). The number of lasing modes decreases with an augmenting B-field, but the overall intensity of individual mode enhances, and the maximum intensity of mode will shift from high to low energy. Again, these lasing will disappear as temperature rising above 150 K at $B = 10T$.

The phenomena of emission burst with dynamical red-shift in energy are attributed to Fermi-edge superfluorescence from a quantum degenerate e-h gas. The diagram of interpretation is shown

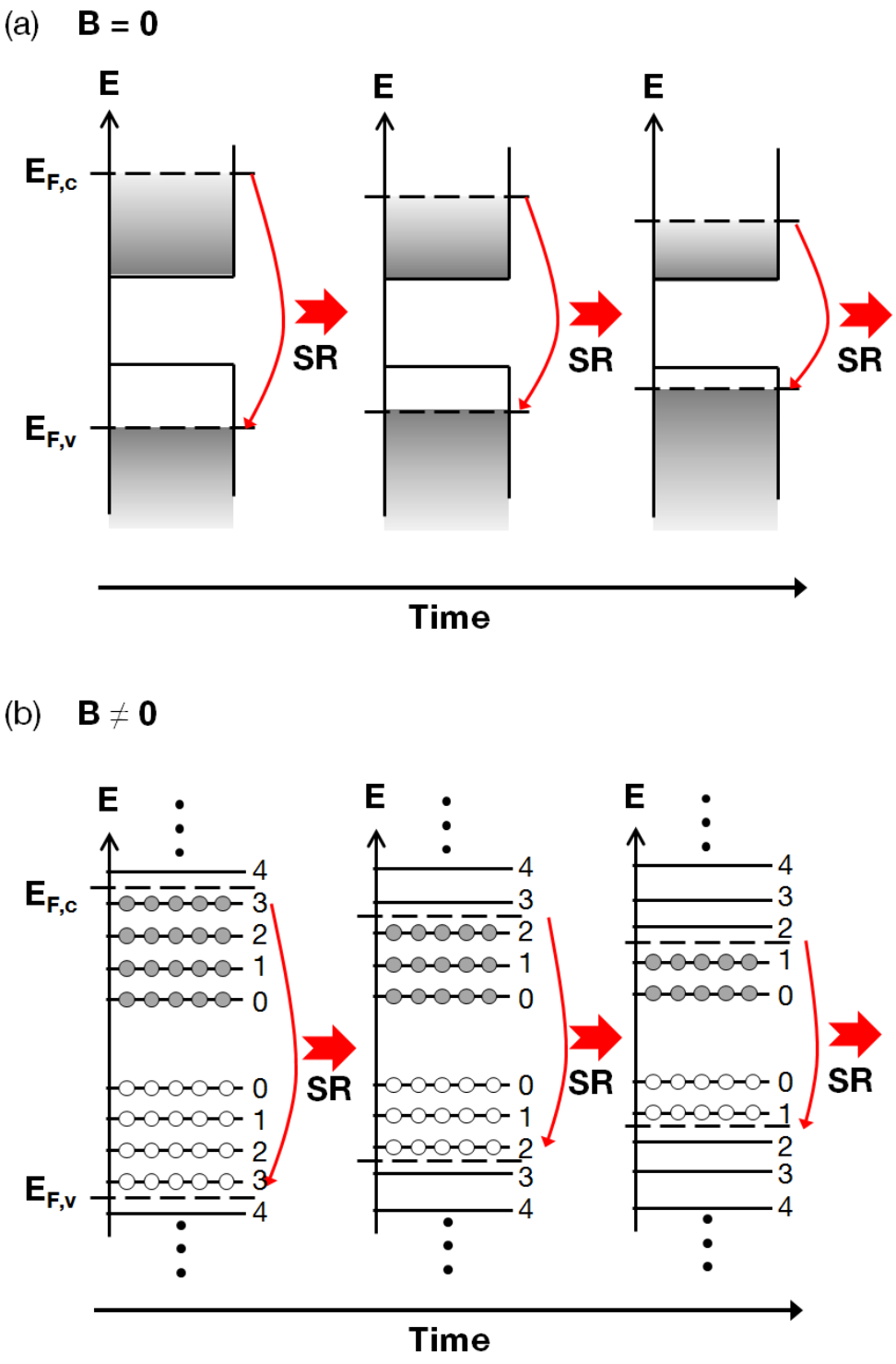

Figure 2.11 **Interpretation of superradiance with dynamically red-shifting energy**

in Fig. 2.11. The photoexcited electrons and holes fill up the conducting and valence bands. However, the Coulomb interaction enhances the correlation of e-h pairs near Fermi band edge. These e-h pairs collectively form a macroscopic dipole with self-organization as mentioned before. As the cooperative spontaneous recombination of electrons and holes occurs, the superradiance commences and the Fermi energy level drops due to consumption of e-h density. But the e-h pairs near new Fermi-edge again build up the macroscopic dipole and result in a giant burst pulse with lower energy. By repeating this steps, the superradiance with energy red-shift is observed in the experiment.

When applying the B-field, the energy levels are quantized into Landau levels. The e-h pairs at the highest occupied Landau level recombine first, again due to the many-body enhancement of gain, then they contribute to sequential burst of superradiance from high energy to low energy. With increasing the magnitude of B-filed, the density of Landau levels changes, causing to varying emission intensity with B-field.

2.7 Optical orientation and spin relaxation in semiconductors

In my dissertation project, I explored the spin dynamics of e-h pairs through measuring the polarizations of emission. Therefore in this section, I briefly introduce the semiconductor optics and a few spin relaxation mechanisms in the following paragraphs. I focus the case of the GaAs-based QW and GaAs material because GaAs constitutes the most part of our sample in this research.

The band structure of bulk GaAs is shown in Fig. 2.12 (a), here I only show the lowest conducting band (s-wave) and valence band (p-wave), which mostly determines the optical properties in semiconductors. The band gap of GaAs is about $E_g = 1.5\,eV$. Due to the spin-orbit coupling, the $j_h = 3/2$ and $j_h = 1/2$ bands are separated by $\Delta = 0.3eV$, where j_h is the angular momentum quantum number of hole in valence band. The $j_h = 3/2$ band has two degenerate bands corresponding to heavy hole ($m_h = \pm 3/2$) and light hole ($m_h = \pm 1/2$). Here m_h are magnetic quantum numbers of hole state.

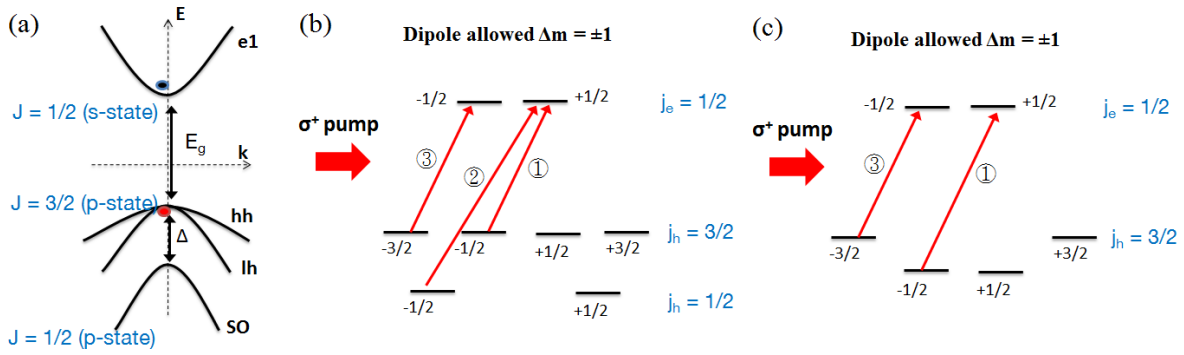

Figure 2.12 **Optical Orientation.** (a), band structure of bulk GaAs with lowest conducting and valence bands. The band gap $E_g \approx 1.5\,eV$, while the spin-orbit coupling splitting Δ is about 0.3 eV. The $j_h = 3/2$ contains two degenerate bands corresponding to heavy hole ($m_h = \pm 3/2$) and light hole ($m_h = \pm 1/2$). (b) Schematic of optical transition of GaAs bulk materials with circularly polarized light. According to angular momentum conservation, the transition obeys selection rule $\Delta m = \pm 1$. where m is the magnetic quantum number of e-h dipole state. The number attached with transition arrow is the probability ratio of transition path. (c) Due to the quantum confinement effect, the valance bands of light holes and heavy holes are split into two non-degenerate dispersions.

Under circularly polarized pumping, the optical transition of electron between conducting and valence band needs to obey selection rule according to angular momentum conservation. Assuming the pumping energy is larger than all difference of conducting and valence bands discussed here, in Fig. 2.12 (b) it shows possible transition paths with relative probability ratio attached on each path. The transition rule illustrates that the quantum number change $\Delta m = m_e - m_h$ is the same as magnetic quantum number of pump photon $m_\gamma = 1$, which is also called selection rule.

In the GaAs-based QW, the bands of the heavy hole and light hole are non-degenerate due to quantum confinement shown in the Fig. 2.12 (c). Since in most experimental studies, the pumping energy is smaller than $E_g + \Delta$, so I focus on the transition between $j_e = 1/2$ and $j_h = 3/2$. With pumping energy $E_g < \hbar\omega < E_g + \Delta$, the average electron spin is $\frac{-1}{2}\frac{3}{4} + \frac{1}{2}\frac{1}{4} = \frac{-1}{4}$, while the average hole spin is $\frac{5}{4}$. Their sum is 1 and equals to the angular momentum of the excited photon. The photo-excited electrons eventually recombine the majority of holes to emit photons, and the system goes back to the ground state. The transition of recombination is required to satisfy the selection rule. In semiconductors, these photo-excited carriers may redistribute their spin population

by carrier-carrier scattering, thus the emitted photon may not be totally right circularly polarized under right circularly polarized excitation. Normally the non-equilibrium spin polarization tends to redistribute equal population of two opposite spins, this phenomena is called spin-relaxation. In general, we could study the carrier spin dynamics through measuring emission polarization from the semiconductors.

The emission polarization from an optically pumped semiconductor is determined by the life-time of excitation dipole and spin relaxation time. Due to the angular momentum conservation, the emission polarization is the same as the polarization of radiative dipole in the system. The polarization of e-h dipole can be defined as the following equation and relates to dipole lifetime τ and spin relaxation time τ_s as:

$$P = \frac{n_+ - n_-}{n_+ + n_-} = \frac{P_0}{1 + \tau/\tau_s} \tag{2.16}$$

There are two limits to quickly get an insight from this equation. (1) Under the limit $\tau \ll \tau_s$, the spin relaxation is negligible compared to the electrons' and holes' lifetime. In this condition, the ensemble of optical-induced e-h dipole is almost not changed after excitation and give the emission with the same polarization as that of pump, or $P \approx P_0$. (2) Under the limit $\tau \gg \tau_s$, the carrier spin re-arranges quickly before e-h recombination with equal carrier population of spin up and spin down. Thus we obtain unpolarized emission with $P \approx 0$.

From Dyakonov's saying: "Spin relaxation can be generally understood as a result of the action of fluctuating in time magnetic fields". In most cases, there is no real magnetic field, but we could imagine an effective magnetic field existing in the system. Generally speaking, the effective magnetic field originates from spin-orbit coupling or exchange interaction.

The spin relaxation resembles the physics picture: the spin makes a precession around a random direction of magnetic field (or B-field) with a typical angular frequency ω and correlated time τ_c. After time τ_c, the direction and the amplitude of effective B-filed changes, and the spin precesses around the new B-field. After a certain number of such steps, the initial spin direction is completely forgotten.

In general, any fluctuation or inhomogeneity of spin interaction can induce spin relaxation.

The various origins lead to several spin relaxation mechanisms. In the spintronics study of III–V semiconductors, there are a few spin-relaxation mechanisms dominates than the others. Here I introduce selective but important mechanisms in the following paragraphs, they are (1) Elliott–Yafet mechanism (2) D'yakonov–Perel' mechanism (3) Bir–Aronov–Pikus mechanism. [74]

- **Elliott–Yafet mechanism (EY mechanism)**

  In the presence of spin-orbit coupling, the electronic eigenstates (Bloch states) mix spin-up and spin-down states. This leads to a finite probability of spin flip if the spatial part of electron wavefunction suffers a transition through scattering, even if the scattering process is spin-independent. In addition, as the spin-orbit interaction is induced by the periodic lattice ions, the lattice vibration (or phonon) could couple to carrier spin resulting in spin-flip. The spin relaxation rate $1/\tau_s$ is inversely proportional to the collisions time τ_p and relates to the scattering geometry ϕ^2. We could use simple form to illustrate this relation: $\frac{1}{\tau_s} \sim < \phi^2 > \frac{1}{\tau_p}$.

- **Dyakonov–Perel mechanism (DP mechanism)**

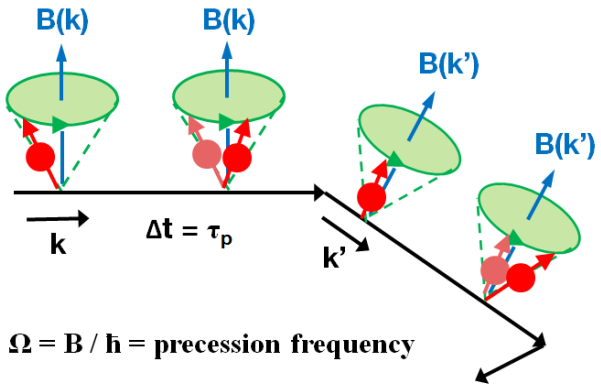

Figure 2.13 **Schematic of Dyakonov-Perel Spin Relaxation**

In III–V or II–VI semiconductors, the bulk inversion asymmetry in lattice structure results in spin-orbit coupling in the conducting band. The Hamiltonian of the spin-dependent term of electrons can be described by $\hbar\Omega(\mathbf{p})\mathbf{S}$, which is regarded as an energy of a spin in an effective magnetic field $\hbar\Omega$. This effective B-field changes its direction due to the electron

collisions. For convenience, I assume the correlation time is τ_p, and the spin relaxation time is τ_s. To obtain a simple relation between τ_s and τ_p, a spin can be imagined to go through a random spin process during time t with total square angle $\Delta\varphi^2$, which is equivalent to square of precession angle within τ_p times the number of steps (see Fig.2.13). That is $\Delta\varphi^2 = (\Omega\tau_p)^2 \times (t/\tau_p)$. The spin relaxation time is defined as $\varphi^2(\tau_s) \sim 1$, thus we get:

$$\frac{1}{\tau_s} \sim \Omega^2 \tau_p \tag{2.17}$$

This mechanism gives a counter-intuition that more electron collisions could enhance the spin relaxation time in the system.

- **Bir–Aronov–Pikus mechanism (BAP mechanism)**

  This mechanism is mostly seen in non-equilibrium electrons in p–type semiconductors due to the exchange interaction between the electron and hole spins. Therefore, the spin relaxation rate is proportional to the number of holes, meaning mechanism might be important in some p-doped semiconductors.

In a GaAs-based semiconductor, the spin relaxation time depends on numbers of factors, like temperature, momentum relaxation time, carrier density and carrier types like electron or hole. For example, in undoped GaAs/AlGaAs (100) QWs, the DP mechanism dominates at high temperature, while BAP mechanism is enhanced at low temperature or p-doped QWs. Even in the same material of semiconductors, different crystal orientation might have distinct spin relaxation times. The famous example is GaAs (110) QWs and GaAs (100) QWs [75]. The spin relaxation time at room temperature is about 2 ns in (110) QWs, but is around 70 ps in (100) QWs. The DP mechanism is thought to be important in these systems. The effective B-field through calculation is perpendicular to QWs plane in (110) QWs case, but lies in QWs plane in (100) QWs. Therefore, electron spins process relative stable effective B-field in (110) QWs, resulting in much longer spin relaxation time.

2.8 Transfer matrix method

The transfer matrix is a useful method to calculate the effective reflectance and transmission of layer-structure materials. In our project, we also implement it to simulate the reflectance of the semiconductor microcavity. Here I take a subsection to outline this method.

In the first step, one could consider how to obtain reflectance and transmission of a particular media, and the structure of the media is:

$$n(z) = \begin{cases} n_1, & z < 0 \\ n_2, & 0 < z < d \\ n_3, & d < z \end{cases} \tag{2.18}$$

Assume an electromagnetic plane wave propagates at xz-plane, and the electric field has the form:

$$\mathbf{E} = E(z) exp[i(\omega t - k_x x)] \tag{2.19}$$

where ω is angular frequency of wave, and k_x is the x-component of the wavevector. k_x is a constant for all layer to satisfy Snell's law in all interface, and we set $k_x \equiv \beta$ for convenience. The electric field can be either an s-wave (with $\mathbf{E} \parallel \mathbf{y}$) or a p-wave (with $\mathbf{H} \parallel \mathbf{y}$). The magnetic field $\mathbf{H}$ can be obtained by $\mathbf{H} = \frac{i}{\omega\mu} \bigtriangledown \times \mathbf{(E)}$. The incidence wave can be divided into right-traveling and left-traveling:

$$E(z) = Re^{-ik_z z} + Le^{ik_z z} = A(z) + B(z) \tag{2.20}$$

R and L are constants in each homogeneous layer. A(z) and B(z) represent the amplitude of right-traveling and left-traveling wave, respectively. $\pm k_z z$ is the z-component of the wavevector. In the i-th layer the z-component wavevector k_{iz} can be rewritten as $k_{iz} = \sqrt{[(\frac{n_i \omega}{c})^2 - \beta^2]} = (\frac{\omega}{c}) n_i \cos\theta_i$, where θ_i is the ray angle measured from the z-axis. We will need this term later. Suppose the right- and left- traveling waves in each layer have amplitude distribution illustrated in

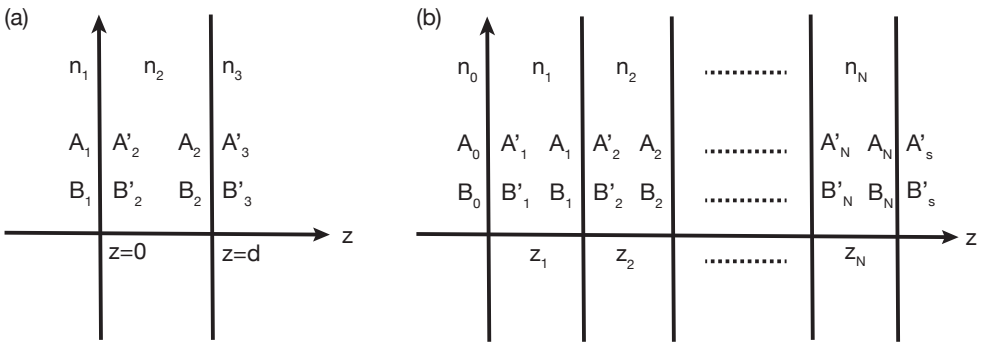

Figure 2.14 **Schematic of multilayer structure.** (a) Three layers structure which the thickness of middle layer is d. (b) Multilayer structure with N layers in the middle. The z_i here represents the thickness of i-th layer.

figure (a), then we define:

$$
\begin{aligned}
A_1 &= A(0^-) \\
B_1 &= B(0^-) \\
A_2' &= A(0^+) \\
B_2' &= B(0^+) \\
A_2 &= A(d^-) \\
B_2 &= B(d^-) \\
A_3' &= A(d^+) \\
B_3' &= B(d^+)
\end{aligned}
\tag{2.21}
$$

where 0^- (0^+) represents the left (right) side of the interface at x = 0, and the definition is similar to d^- (d^+). Now boundary condition requires that all the electromagnetic field and its first derivative are continuous at each interface. These requirements, $E(0^-) = E(0^+)$, $E'(0^-) = E'(0^+)$, $E(d^-) = E(d^+)$, and $E'(d^-) = E'(d^+)$, give the relation between A_i and B_i coefficients. If the two amplitude of E(z) are represented as column vector, we could organize these relations

as:

$$\begin{aligned}
\begin{pmatrix} A_1 \\ B_1 \end{pmatrix} &= D_1^{-1} D_2 \begin{pmatrix} A_2' \\ B_2' \end{pmatrix} \equiv D_{12} \begin{pmatrix} A_2' \\ B_2' \end{pmatrix} \\
\begin{pmatrix} A_2' \\ B_2' \end{pmatrix} &= P_2 \begin{pmatrix} A_2 \\ B_2 \end{pmatrix} = \begin{pmatrix} e^{i\phi_2} & 0 \\ 0 & e^{-i\phi_2} \end{pmatrix} \begin{pmatrix} A_2 \\ B_2 \end{pmatrix} \\
\begin{pmatrix} A_2 \\ B_2 \end{pmatrix} &= D_2^{-1} D_3 \begin{pmatrix} A_3' \\ B_3' \end{pmatrix} \equiv D_{23} \begin{pmatrix} A_3' \\ B_3' \end{pmatrix}
\end{aligned} \tag{2.22}$$

The matrices D_i describes the boundary condition at each interface, it is also called dynamical matrices in the book [76].The equations of D_i are:

$$D_i = \begin{cases} \begin{pmatrix} 1 & 1 \\ n_i \cos\theta_i & -n_i \cos\theta_i \end{pmatrix}, & \text{for s-wave} \\ \begin{pmatrix} \cos\theta_i & \cos\theta_i \\ n_i & -n_i \end{pmatrix}, & \text{for p-wave} \end{cases} \tag{2.23}$$

where $i = 1,2,3$ is index of each layer. The P_2 is a propagating matrix, which accounts for the propagation through the bulk of the layer. The phase ϕ_2 is:

$$\phi_2 = k_{2z} d = n_2 \frac{\omega}{c} \cos\theta_2 \, d \tag{2.24}$$

Combining coefficients in Eq. 2.22, we obtain:

$$\begin{pmatrix} A_1 \\ B_1 \end{pmatrix} = D_1^{-1} D_2 P_2 D_2^{-1} D_3 \begin{pmatrix} A_3' \\ B_3' \end{pmatrix} \tag{2.25}$$

Thus the column vectors represents the amplitude of leftmost and rightmost side of three layer structure connected by the product of 2×2 matrices in sequence. Each side of interference is represented by a D-matrix, and the bulk of materials is represented by a P-matrix. We could extend this formula for multilayer structure shown in figure (b), and obtain:

$$\begin{pmatrix} A_0 \\ B_0 \end{pmatrix} = D_0^{-1} \left(\prod_{i=1}^{N} D_i P_i D_i^{-1} \right) D_s \tag{2.26}$$

Assuming the incidence wave is right-traveling wave, and no left-traveling wave appears in substrate ($B'_s = 0$), we can express the reflectance R and transmission T with coefficient of A_0, B_0 and A'_s as:

$$T = \left|\frac{A'_s}{A_0}\right|^2 \quad , \quad R = \left|\frac{B_0}{A_0}\right|^2 \tag{2.27}$$

In my dissertation project, this method can be applied to simulate the reflectance of microcavity sample and compared to the experimental result. I also used this method to see the energy shift of cavity resonance in microcavity sample resulting from the refractive index change in middle materials.

CHAPTER 3

EXPERIMENTAL METHODS

Our goal is to explore the many-body physics in coupled $e-h-\gamma$ system at large density and room temperature. In this chapter, I present the sample design to approach the issue in semiconductor microcavity as well as the selection of optical excitation to avoid laser coherence imprinted on the system. After that, the experimental setup of imaging/spectroscopy, light polarization control, and beam shaping of excitation beam profile is mentioned. These methods are used to explore the excitation spatial intensity and polarization effect on the system, and also to characterize the emission properties. In addition, the carrier dynamics in the system is investigated by measuring the luminescence dynamics and absorption/gain spectrum with the corresponding setup illustrated.

3.1 Sample characteristics

In order to maintain high density carrier inside a microcavity and prevent carriers from radiative loss before lasing, one solution is designing cavity resonance far above quantum wells. On the other hand, my co-worker and I are interested in exploring the coherent states in high EHP but avoid optical excitation affecting the carrier correlation. Therefore the excitation is chosen at an energy much higher than emission energy, and such photoexcited carriers normally lose spin coherence after long relaxation. I will introduce sample characteristics in more details in the following paragraphs.

3.1.1 Sample structure and fabrication

The microcavity sample was designed by Dr. Chih-Wei Lai and was made by our collaborators Yi-Shan Lee and Sheng-Di Lin. The sample was grown on a semi-insulating (100)-GaAs substrate by using a molecular beam expitaxy method. The structure is entirely undoped and

(a)

Composition	# of monolayers	Thickness (nm)	Label	Description
GaAs	105	59	Cap	Cap layer
:	:	:	:	17 pair DBR
AlAs	135	76	DBR layers	(Top Mirror)
GaAs	105	59	DBR layers	
AlAs	57	44	DBR layers	Transitional layer
GaAs	21	12.0	Cavity/Barrier	QW active layer
$In_{0.15}GaAs$	10	6.0	Quantum Well	
GaAs	21	12.0	Cavity/Barrier	
$In_{0.15}GaAs$	10	6.0	Quantum Well	
GaAs	21	12.0	Cavity/Barrier	
$In_{0.15}GaAs$	10	6.0	Quantum Well	
GaAs	145	81.8	Cavity/Barrier	Spacer
$In_{0.15}GaAs$	10	6.0	Quantum Well	QW active layer
GaAs	21	12.0	Cavity/Barrier	
$In_{0.15}GaAs$	10	6.0	Quantum Well	
GaAs	21	12.0	Cavity/Barrier	
$In_{0.15}GaAs$	10	6.0	Quantum Well	
GaAs	145	81.8	Cavity/Barrier	Spacer
$In_{0.15}GaAs$	10	6.0	Quantum Well	QW active layer
GaAs	21	12.0	Cavity/Barrier	
$In_{0.15}GaAs$	10	6.0	Quantum Well	
GaAs	21	12.0	Cavity/Barrier	
$In_{0.15}GaAs$	10	6.0	Quantum Well	
GaAs	21	12.0	Cavity/Barrier	
AlAs	57	44	DBR layers	Transitional layer
GaAs	105	59	DBR layers	20 pair DBR
AlAs	135	76	DBR layers	(Bottom Mirror)
:	:	:	:	
GaAs	*Buffer layer (~100nm)*			
GaAs	*(100) semi-insulating substrate*			

(b)

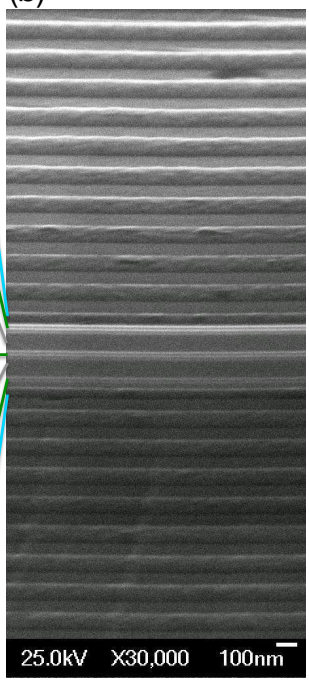

Figure 3.1 **Microcavity structure.** (a), Structure of the microcavity: InGaAs multiple quantum wells (MQWs) are embedded within a λ GaAS cavity between two distributed Bragg reflectors (DBRs). The thickness of GaAs and AlAs in DBRs are 61-nm and 78-nm, while the thickness of InGaAs and GaAs in MQW are 6-nm and 12-nm, respectively. We adjust the antinodes of the cavity light field to the MQW layers by adding two transitional AlAs layers and a GaAs cap layer. (b), A cross-sectional SEM image showing the active regime and adjacent layers of the DBRs .

contains a λ GaAs sandwiched by distributed Bragg reflectors (DBRs). The top (bottom) DBR consists of 17 (20) of GaAs/AlAs $\lambda/4$ layers, and the central cavity consists of three stacks of three $In_{0.15}Ga_{0.85}As$/GaAs multiple quantum wells (MQWs) each, positioned at the anti-node of the cavity light field. (Fig. 3.1) The bare cavity resonance is $E_c \approx 1.405$ eV ($\lambda_c = 883$ nm) and the QW bandgap ($E_g' \sim 1.33$ eV at room temperature) is tuned through a rapid thermal annealing process (at 1010 °C - 1090 °C for 5-10 ps), in which the InGaAs QW bandgap blueshifts because of the diffusion of gallium ions into MQW layers.

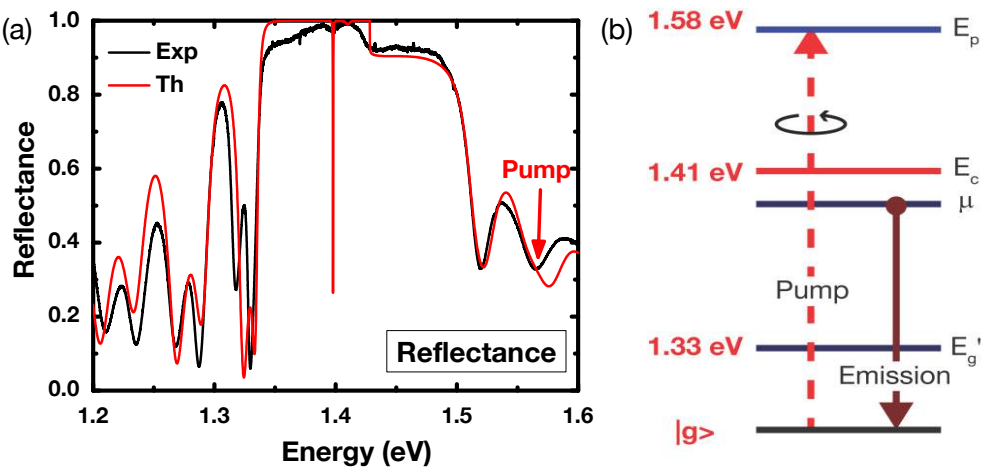

Figure 3.2 **Reflectance and laser spectral characteristics.** (a) Reflectance spectrum at $k_{||} = 0$ from the front surface of a microcavity sample with 1.405 eV lasing energy at the threshold: measured (black solid line) and simulated (orange solid line). This sample is an as-grown sample not subject to a rapid thermal annealing process. The simulation is performed via a transfer matrix method, including the optical absorption in the GaAs layers, but excluding the complex dielectric constant of excitons (*e*-*h* pairs) in MQWs. The cavity resonance (E_c) is about 1.41 eV. (b) Optical pumping scheme in the experiment.

3.1.2 Sample characteristics

Here I present our microcavity sample properties as well as the energy shift in MQWs under non-resonant pumping. Fig. 3.2 is measured reflectance spectrum from one of our samples. The cavity resonance E_c is around 1.405 eV with negligible TE and TM energy slitting at small emission direction (Fig 3.3 (a), the relation of in-plane momentum and emission angle will be explained in the section 3.2.1). The small TE-TM energy splitting contributes to laser polarization control and diminishes the crystalline field effect on light polarization. The pumping energy in the experiment is about 1.58 eV ($\lambda_p = 785$ nm), which is a local minimum of reflectivity. The choice of pumping energy is to prevent the correlation of carriers at emission levels from the lasing coherence effect, and in the mean time, to keep maximum transmitted flux as large as possible. The quantum well band gap is about 1.33 eV. At a low photoexcited density, the chemical potential μ is far off-resonant with respect to E_c, and the radiative recombination of e-h carriers is largely suppressed. μ advances toward E_c with increasing photoexcited density, then luminescence efficiency

nonlinearly enhances and results in laser radiation at the gain overcomes the cavity loss. Fig. 3.3 (b) demonstrates matter gain spectrum inside the microcavity.

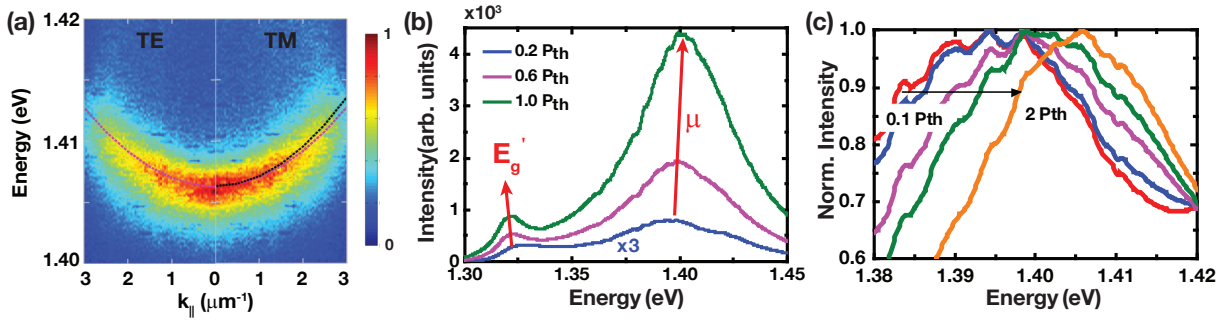

Figure 3.3 **Microcavity sample characterization.** (a) E vs. $k_{||}$ dispersions for the TE (left) and TM (right) modes under a circularly polarized pump at 1.579 eV and $P = 0.6\ P_{th}$. The photoexcited density at P_{th} is $\sim 2-3\times10^{12}$ cm^{-2} per quantum well *per pulse*. The simulated TE and TM dispersions are shown as magenta and black curves, respectively. The TE-TM energy splitting is less than 50 μeV at $k_{||}=0$, allowing the effective control of lasing polarization by optical pumping. (b) To determine the density-dependent spectral characteristics of PL in the InGaAs/GaAs MQWs, we measure the time-integrated and time-resolved PL in the sample, with the top DBR mirror layers removed, by selective wet etching [77]. PL spectra at $P = 0.2$ (blue), 0.6 (magenta), and 1 P_{th} (green) in the absence of the top DBR mirrors. Here, PL is attributed to the spontaneous radiative recombination of photoexcited carriers in the InGaAs/GaAs MQWs. The dual PL spectral peaks are attributed to the first and second quantized energy levels in the MQWs, respectively. The QW bandgap (E_g') corresponds to the ground state, the transition between the first quantized energy levels of the electron and the heavy-hole ($e1hh1$). E_g' can decrease with the increasing photoexcited density (band gap renormalization). μ can be deduced from PL from the excited state (second quantized levels, $e2hh2$ transition). With an increasing density, E_g' redshifts slightly because of band gap renormalization, whereas μ blueshifts considerably ($\sim$ 10 meV) as a result of phase space filling (Pauli blocking) at a high photoexcited density ($\gtrsim 10^{12}$ cm^{-2} per QW). (c) Normalized PL spectra near 1.40 eV, which displays a significant spectral blueshift of 15–20 meV with the increasing photoexcited density (0.1 to 2 P_{th}).

To better understand how the matter in InGaAs/GaAs MQWs affects cavity, determining the density-dependent spectral characteristics of MQWs is necessary. Time integrated photoluminescence (PL) in the sample with top DBR mirrors layers removed is shown in Fig. 3.3 (b). The μ blue shifts in energy because of band filling of electrons and holes, and it approaches to E_c as pump flux closed to critical magnitude (called lasing threshold P_{th}, which lasing effect initiates in microcavity). The spectral blue shifts could be as large as 15-20 meV with increasing photoex-

cited density (0.1-2 P_{th}). The PL and spin dynamics in MQWs are investigated in Fig. 3.4. Under non-resonantly circularly polarized pumping (E_p is about 200 meV above E_g), unequal orthogonal circularly polarized emissions are observed within 10 ps after excitation, indicating imbalance carriers spins exists in MQWs. The spin relaxation of e-h carriers can be determined by the decay of emission intensity difference between two orthogonal circular components, which displays relaxation time less than 10 ps.

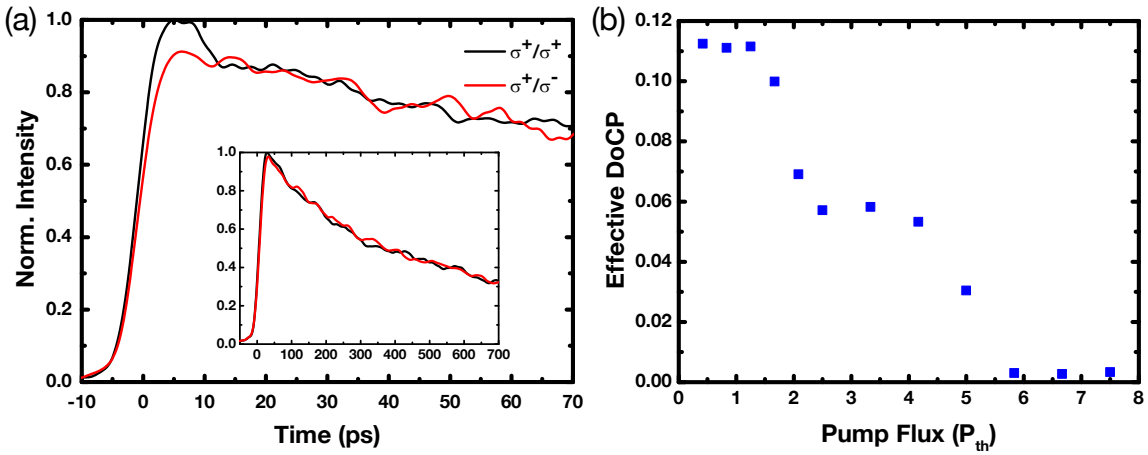

Figure 3.4 **Time-dependent polarized PL in InGaAs/GaAs MQWs.** (a) Time-resolved polarized PL $I^{\pm}(t)$ (black lines: $I^{+}(t)$, co-circular σ^{+}/σ^{+} component; red lines: $I^{-}(t)$, cross-circular σ^{+}/σ^{-}). Time-dependent *DoCP* $\rho_c(t)$ has a finite value of 0.12 when PL intensity increases to its maximum in about 10 ps, and then decays rapidly with a spin relaxation time $\tau_s <$ 10 ps. On the other hand, the carrier decay time is much larger, $\tau_n \sim 1$ ns, as deduced from the overall decay of time-dependent PL intensity $I(t)$ (inset). (b) Effective initial stationary *DoCP*, $\bar{\rho}_c^* = \int_{t=0}^{t=10\,ps} \frac{I^{+}(t)-I^{-}(t)}{I^{+}(t)+I^{-}(t)}\,dt$, as a function of pump flux. We determine $\bar{\rho}_c^*$ to be always less than 0.1 in InGaAs MQWs with similar photoexcited e-h carrier densities. The photoexcited density at P_{th} is $\sim 2-3\times10^{12}$ cm^{-2} per quantum well *per pulse*. The diminishing $\bar{\rho}_c^*$ with increasing pump flux above 2 P_{th} suggests that the spin relaxation time τ_s decreases further as compared to carrier lifetime τ_n at high photoexcited densities, owing to increasingly dominant spin-flipping carrier-carrier scatterings.

3.2 Experimental setup

In order to analyze the radiation properties from our microcavity sample, we built a combination of few experimental setups to measure the light spectrum, polarization and dynamics. The imaging

spectroscopy setup detects angular and spectral properties of light. A combination of liquid crystal devices helps with controlling/analyzing the excitation/luminescence polarizations. The heating effect and carrier diffusion are both suppressed in thermal management setup. Temporal image obtained from Streak camera reveal light dynamics and provides information of radiative carrier dynamic in microcavity. On the other hand, the absorption/gain spectrum is measured by two-color pump-probe setup to explore whether a gap opens under intense excitation in microcavity. We will also study the total carriers (including non-radiative carriers) spectral and temporal dynamics as well as the transient cavity resonance in the system.

3.2.1 Image spectroscopy setup

We measure the angular and spectral properties of luminescence in the reflection geometry (see Fig. 3.5). In a planar microcavity, carriers coupled to the cavity light field are characterized by an in-plane wave number $k_{||} = k\sin(\theta)$ because of the 2D confinement of both photons and carriers. The leakage photons can be used to directly measure the angular distribution of optically active carriers. Angle-resolved luminescence imaging and spectra of these leakage photons are measured through a Fourier transform optical system. A removable f = 200 mm lens (lens L2 in Fig. 3.5) enables the projection of either momentum-space (k-space) or real-space (r-space) luminescence onto the entrance plane of the slit of the spectrometer. Luminescence is collected through an objective lens, separated from the reflected specular or scattered pump laser light with a notch filter, and then directed to an imaging spectrometer. A single circular transverse lasing mode with a spatial mode diameter $\approx 8\,\mu m$ is isolated in measurement by a pinhole positioned at the conjugate image plane of the microcavity sample surface (referred to whole experimental setup in Fig. 3.6). The spectral resolution is $\approx 0.1nm$ ($150\mu eV$), which is determined by the dispersion of the grating (1200 grooved/mm) and the entrance slit width ($\sim 200\mu m$). The spatial (angular) resolution is $\approx 0.3\mu m$ (6 mrad) per CCD pixel.

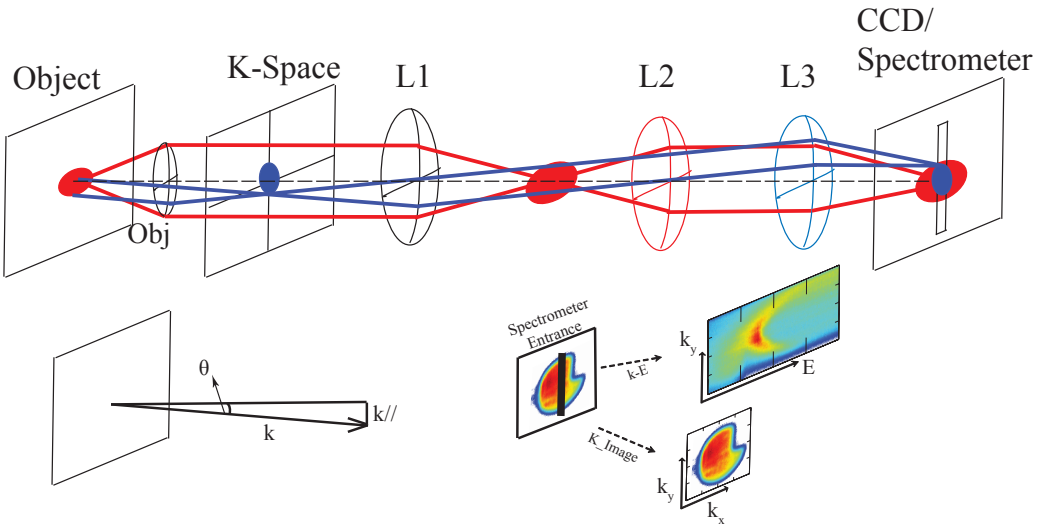

Figure 3.5 **Angle-resolved imaging/spectroscopy setup.** Luminescence from the microcavity is collected by a microscope objective. The luminescence with field distribution $F(X,Y)$ is Fourier transformed into a far-field image in the back focal plane of the objective with coordinates (u,v). This plane is mapped into k-space with (k_X,k_Y), where k_X or $k_Y \equiv k_{||}$, the in-plane momentum. The field distribution in this plane is relayed to the entrance plane of the spectrometer using a pair of lenses L1 and L3 (blue line path). To measure the real-space imaging plane (r-space) on sample, the L2 lens is inserted to form two telescopes and the image is projected on the entrance plane of the slit (red line path).

3.2.2 Thermal management

At a high pump flux, the steady-state incident power transmitted to the sample at the 76 MHz repetition rate of the laser will exceed 50 mW and result in significant thermal heating and carrier diffusion. The techniques we use to control the thermal heating and diffusion of the photoexcited carriers are (1) temporally modulating the pump laser intensity to suppress the thermal carrier heating and (2) spatially shaping the pump beam profile to enable lasing in a single transverse mode. Steady-state thermal heating can inhibit laser action and lead to spectrally broad red-shift luminescence. To suppress steady-state thermal heating, we temporally modulate the 2-ps 76 MHz pump laser pulse train with a duty cycle (on/off ratio) < 0.5 % by using a double-pass acousto-optic modulator (AOM) system [78]. The time-averaged power is limited to below 0.2 mW for all experiments. Multiple transverse modes can simultaneously lase because of the diffusion of

photoexcited carriers and crystalline disorder, which lead to instability and complex lasing characteristics. To control carrier diffusion, we holographically generate a flat-top pump beam profile (area $\approx 300\ \mu m^2$) at the sample surface with a spatial beam shaper consisting of a two-dimensional (2D) liquid-crystal spatial light modulator (SLM) [79].

3.2.3 Optical control and beam shaping

Besides controlling carrier diffusion through flattop beam profile, SLM allows us to design other shape of beam profile to affect lasing behaviors. For example, we can generate double-hump-shaped beam profile serving as optical confinement, and photons inside the confinement could form quantum-oscillator-like lasing modes. These experimental results will be explicitly described in Chapter 6. The optical excitation setup including SLM is shown in Fig. 3.6. The front surface of the microcavity is positioned at the focal plane of a high-numerical-aperture microscopy objective lens (N.A. = 0.42, 50×, effective focal length 4 mm). A 3× telescope, a Faraday rotator, a polarizing beam splitter, and the objective lens form a reflected Fourier transform imaging system. The light fields at the SLM and sample surface form a Fourier transform pair. The 2D SLM (1920×1080 pixels, pixel pitch = 8 μm) enables us to generate arbitrary pump geometries with a $\approx$2 μm spatial resolution at the sample surface using computer-generated phase patterns. A small gold mirror inserted in front of objective lens is used to direct laser pumping microcavity sample with a small incident angle, and is positioned to block luminescence light path as small as possible but maintain pump flux in the mean time. The pump flux can be varied by more than two orders of magnitude using a liquid-crystal attenuator.

3.2.4 Polarization control

The polarization state of the pump/luminescence is controlled/analyzed by a combination of liquid crystal devices, such as variable retarders, polarization rotators, and Glan-Taylor/Glan-Thomson polarizers without mechanical moving parts. A polarization compensator (Berek's variable wave

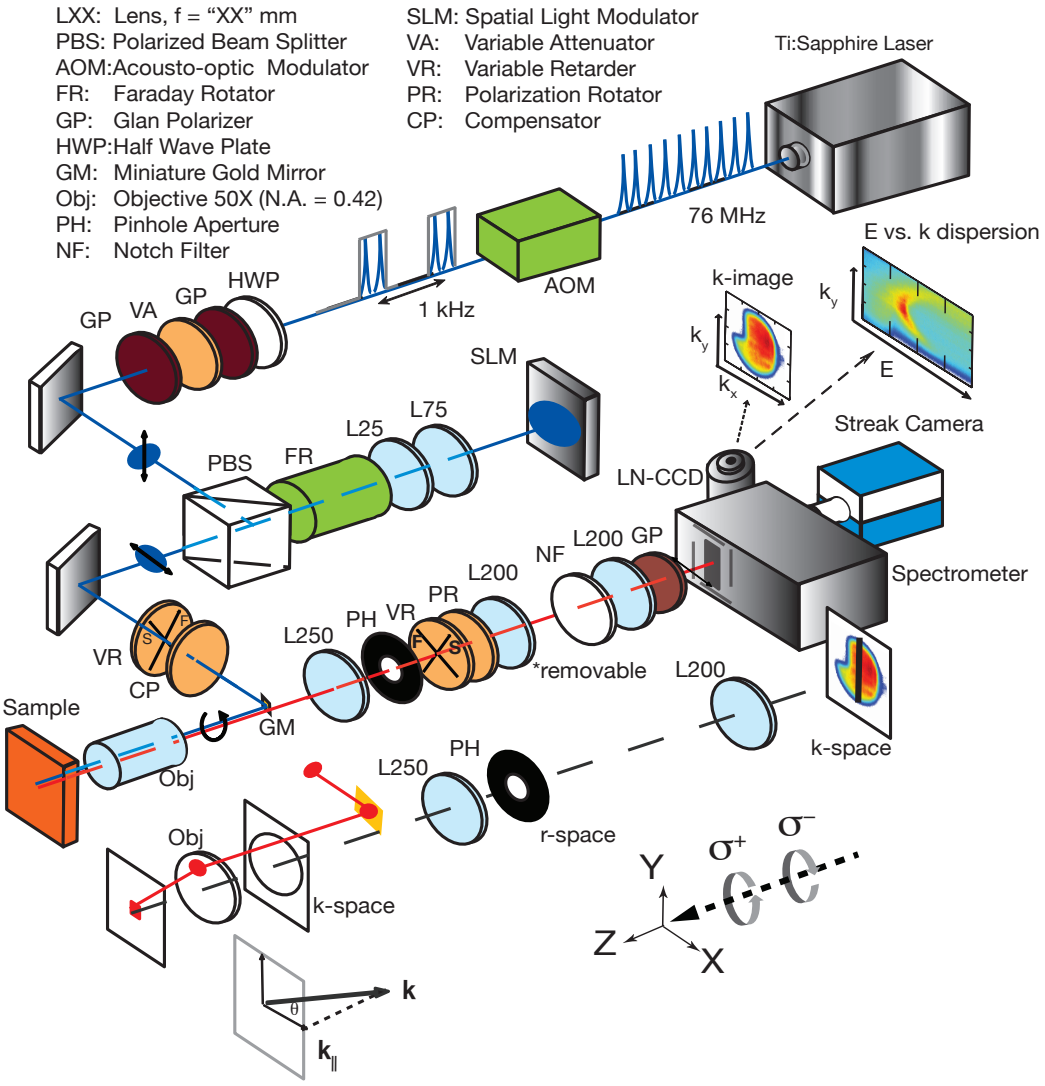

Figure 3.6 **Whole Experimental Set-up.** Luminescence from the microcavity is collected by a microscope objective (N.A. = 0.42, effective focal length $f_0 = 4$ mm). The collection angle is up to $\theta \approx 25^\circ$ in air. The measurement of imaging/spectroscopy can be referred to Fig. 3.5, with the lens labeled with focal length (ex: L200 means $f = 200$ mm). In the conjugate real-space imaging plane (r-space), we place a 600-μm diameter circular aperture to spatially isolate luminescence and a single transverse mode within a circular $\approx$10-μm diameter area on the sample. The image at the entrance plane can be directed to the LN-CCD for time-integrated imaging/spectroscopy or to the streak camera system for time-resolved measurements. In this configuration, we measure the angular distribution of luminescence as k-space images (k-images) or spectra (E vs. $k_{||}$ dispersions) using respectively the 0-order or 1st-order diffracted light from the grating. By inserting a removable 200 mm focal-length lens (L200), we project the r-space luminescence to the entrance plane of the spectrometer.

plates) is used to compensate for the phase retardance induced by the reflection from the miniature gold mirror surface. The circularly polarized pump or luminescence with angular momentum $+\hbar$ ($-\hbar$) along the pump laser wavevector $\hat{k} \parallel \hat{z}$ is defined as σ^+ (σ^-). Linearly polarized light with horizontal (vertical) polarization is defined as σ^X (σ^Y). The polarization state is characterized by the Stokes vector $\{S_0, S_1, S_2, S_3\}$. S_0 is the flux and is determined as $S_0 = I^+ + I^- = I^X + I^Y = I^{45^\circ} + I^{135^\circ}$. The Stokes vector can be normalized by its flux S_0 to the Stokes three-vector $s = \{s_1, s_2, s_3\}$. $s_1 = (I^X - I^Y)/(I^X + I^Y)$, $s_2 = (I^{45^\circ} - I^{135^\circ})/(I^{45^\circ} + I^{135^\circ})$, and $s_3 = (I^+ - I^-)/(I^+ + I^-)$. $I^+, I^-, I^X, I^Y, I^{45^\circ}$, and I^{135° are measured time-integrated or temporal intensities of the circular or linear polarized components. The polarization state is represented by using the following three quantities: the degree of circular polarization ($DoCP \equiv \rho_c = s_3$), degree of linear polarization ($DoLP \equiv \rho_l = \sqrt{s_1^2 + s_2^2}$), and degree of polarization ($DoP \equiv \rho = \sqrt{s_1^2 + s_2^2 + s_3^2}$). The accuracy of the measured polarization state is $\approx$1-2%.

3.2.5 Temporal measurement setup

To know carrier energy and spin relaxation between excitation and radiative emission, we performed time-resolved measurement on luminescence intensity, transient spectral distribution, and polarization. Two ways are utilized in temporal measurement: (1) spectroscopy detected through Streak camera (2) absorption of reflective spectrum measured through pump-probe technique. Our Streak camera enables time-resolved luminescence measurement in real- and momentum space as well as spectrally time-resolved image measurement with 5-ps time resolution in overall system setup. This method provides quick investigation on radiative carrier dynamics inside the system, but it can not explore non-radiative carrier dynamics as well as the fast e-h spin relaxation if spin-relaxation time is less than 5 ps.

To compensate the shortage of Streak spectroscopy measurement and to investigate the potential existence of carrier correlation in the system (detail motivation is introduced in chapter 7), we performed two-color pump-probe experiment with setup shown in Fig. 3.7. The pump-probe setup is based on previous setup with few modifications: (1) add probe laser with about 20 fs pulse

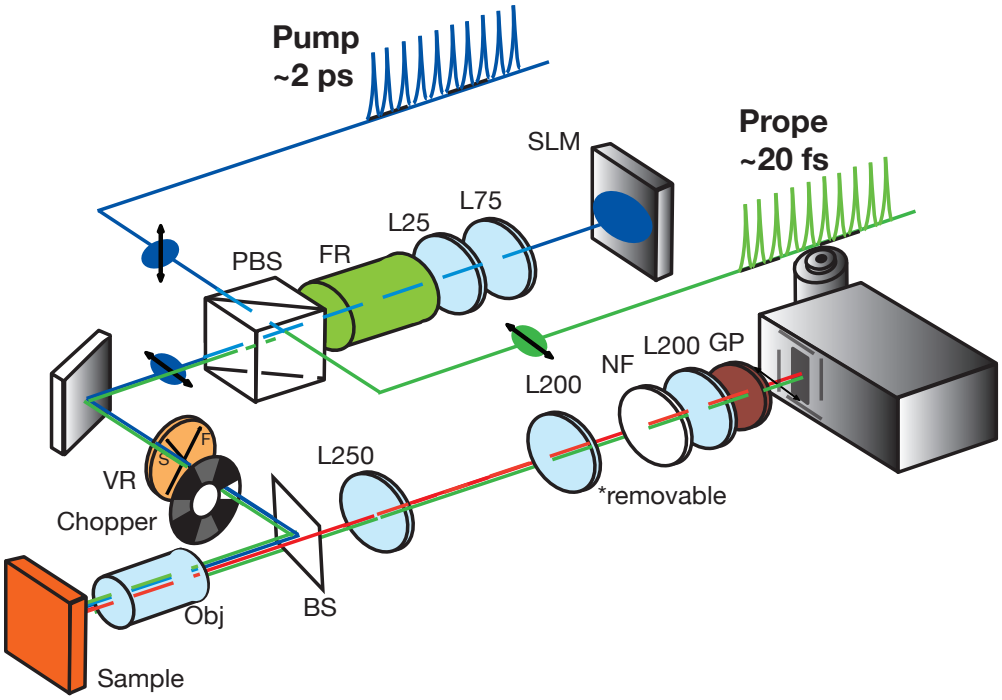

Figure 3.7 **Pump-probe setup.** The setup is similar to Fig. 3.6, but the compensator is replaced by chopper due to limited space, and the gold mirror is swapped with beam splitter (BS). The probe pulse laser with horizontal polarization enters in system through the other side of polarized beam splitter (PBS), then merges with pump excitation from Ti:sapphire laser. Thus in pump-probe setup here the polarizations of pump and probe pulse are orthogonal. To simplify the diagram, liquid crystal device and pinhole along optical axis through spectrometers are hidden.

width from the other face of polarized beam splitter (PBS), and the light path of probe laser merges with that of pump laser after PBS. In this case, the polarizations of pump and probe laser pulses after objective lens are always orthogonal; (2) remove AOM setup in pump light path, and replace compensator with a chopper due to limited space in original setup. The "on-and-off" ratio through chopper is set about 1:100; (3) swap gold mirror (GM) with beam splitter (BS). For simplicity, few optical components are hidden in Fig. 3.7. The probe laser hitting on the microcavity can be translated with its position or oriented its incoming angle with respect to the sample surface by tuning two mirrors set before the probe passes through the PBS. In the experiment, the laser spots from pump and probe laserare assured to be spatially overlapped for each adjustment of the probe laser. The usage of BS allow us to have larger tuning angle of probe laser, but it also affects the ac-

curacy of light polarization measurement because the transmittance of horizontally and vertically polarized light are not the same.

3.3 Conclusion

In summary, the large detuning of cavity resonance and QW bandgap significantly prohibits radiative loss from cavity and enhances the accumulation of photoexcited e-h pairs in MQWs. The negligible TE-TM splitting results in a straightforward implement of spin-control lasers. Non-resonantly pumping can avoid laser coherence imprint on carrier correlation, which helps us to study the phase of e-h-γ system at high density. Image spectroscopy setup accompanied with polarization control design enable to measure angular and spectral characteristics of light as well as its polarization, and these physical quantities reveals the E-vs-$k_{||}$ dispersion and spin relaxation of radiative carriers in MQWs. The Streak image offers a fast insight in carrier energy and spin dynamics at the same time. On the other hand, absorption/gain spectrum measured by two-color pump-probe setup uncover the evolution of cavity resonance shifting and its dispersion. All these measurements bring a comprehensive understanding of photoexcited carrier spin and energy dynamics in our system, and further help with analyzing the lasing mechanism inside the system.

CHAPTER 4

SPIN-POLARIZED LASING IN A HIGHLY PHOTOEXCITED SEMICONDUCTOR MICROCAVITY

In this chapter, I demonstrate room-temperature spin-polarized ultrafast pulsed lasing in a highly photoexcited planar semiconductor microcavity. The emission above critical threshold exhibits angularly narrow pulsed lasing with the pulse width about 20 ps. The radiation shows energy blue shift and spectral broadening with increasing pump flux. In addition, the emission polarization can be controlled by excitation intensity as well as polarizations. The emission polarization is highly circularly polarized under elliptically polarized pumping and can exceed the input circular polarization degree. All these results will be presented in the following sections followed by a theoretical explanation.

To investigate the laser action in microcavity with high-density photoexcited carriers, we optically pump the sample nonresonantly by using 2 ps Ti:Sapphire laser pulses at E_p = 1.579 eV ($\lambda_p = 785$ nm) with flattop square beam profile. The laser pump flux is varied by two orders of magnitude, which the created photoexcited density ranges from approximately 5×10^{11} to 10^{13} cm^{-2} per QW *per pulse* and corresponds to a 2D density parameter $r_s = 1/(a_0\sqrt{\pi n_{th}}) \approx 5.3$–$1.2$ for $a_0 \approx$15 nm in InGaAs QWs [80].

4.1 Spin-polarized lasing at room temperature

The laser is characterized in terms of the angular distribution and energy as functions of the in-plane momentum [angle-resolved (k-space) images and E vs. $k_{\|}$ dispersions] (Fig. 4.1). At the threshold, the emission of the microcavity investigated here becomes angularly and spectrally narrow for the co-circular σ^+/σ^+ component, where σ^+/σ^+ is the helicity of the pump/emission, respectively. An intense radiation mode emerges within an angular spread $\Delta\theta < 3^\circ$, corresponding to a standard deviation $\Delta k = 0.3\ \mu$m^{-1} in k-space. Approximating such a partially coherent beam

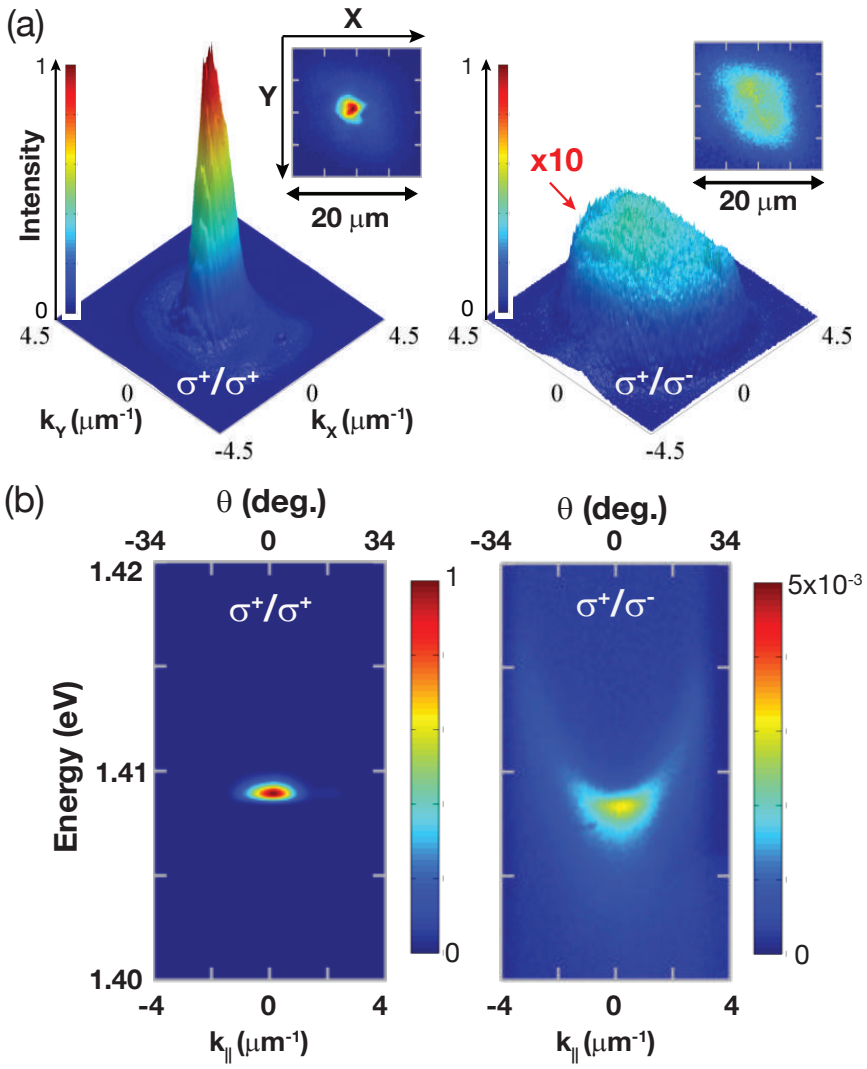

Figure 4.1 **Spin-polarized lasing at room temperature.** (a) Angle-resolved [k-space (k_X, k_Y)] luminescence images at the lasing threshold ($P = P_{th}$) for co-circular (σ^+/σ^+, left panel) and cross-circular (σ^+/σ^-, right panel) components. Here, $\sigma^\pm/\sigma^\pm$ represents the polarization of pump/luminescence, respectively. $P_{th} \approx 2.5 \times 10^8$ photons *per pulse* (over an area of 80 μm^2), resulting in a photoexcited density $n_{th} \approx 3 \times 10^{12}$ cm^{-2} per QW *per pulse* for an estimated absorption of 10% for nine QWs. Insets are the corresponding real space (r-space) luminescence images. (b) Energy (E) vs. in-plane momentum ($k_{||}$) dispersions along the k_Y axis ($k_X = 0, k_Y = k_{||}$).

as a Gaussian Schell-model source [81], we can determine a spatial coherence length of 4 μm, which is close to the spatial dimension of the lasing mode. On the contrary, no lasing action occurs for the cross-circular σ^+/σ^- component, which exhibits an angularly broad intensity distribution

and a parabolic E vs. $k_{||}$ dispersive spectrum. Accordingly, the radiation at the threshold has a highly circular polarization.

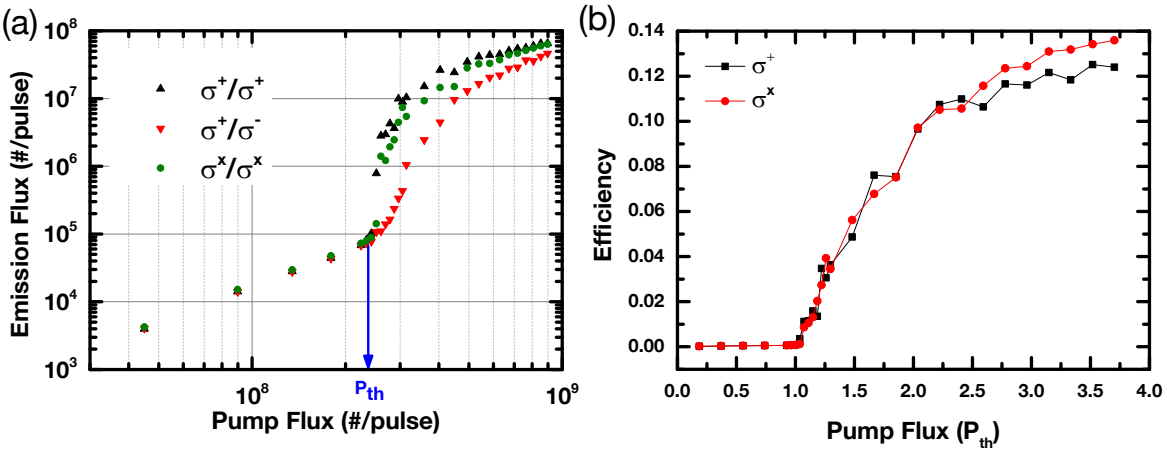

Figure 4.2 **Nonlinear input-output.** (a) Emission flux integrated over $\left|k_{||}\right| \lesssim 3\mu m^{-1}$ under σ^+ (circularly) or σ^X (linearly) polarized pump. (b) Radiative emission efficiency vs. pump flux under a circularly (σ^+) and linearly (σ^X) polarized pump.

Next, I will describe the nonlinear input-output and polarization characteristics with varying pump flux. Fig. 4.2 (a) shows the emission flux (output) vs. the pump flux (input) under a circularly (σ^+) polarized excitation. The pump flux is the photon flux per pulse transmitted into the microcavity within a circular 10 μm diameter area. The output nonlinearly increases by one order of magnitude for an increase in the input by less that 20% near the critical photoexcited density. The onset of such a nonlinear output for the co-circular component (σ^+/σ^+) is defined as the threshold P_{th} (indicated by an arrow in the figure). For $P \gtrsim 1.5\,P_{th}$, the cross-circularly polarized component (σ^+/σ^-) also lases. Under a linearly polarized pump (Fig. 4.2(a), green dots), the laser action commences at a slightly higher pump flux ($P = 1.05\,P_{th}$). This 5% threshold reduction with the optical injection of the spin-polarized carriers is small but significant compared with the $<$1% reduction predicted for an InGaAs-MQW-based conventional spin lasers [82]. In general, such a threshold reduction is less than 5% in most locations and samples studied in this work.

The total emission under a circularly polarized pump is close to that under a linearly polarized one (Fig. 4.2 (b)). The overall efficiency (the ratio of the emission flux emanating from the front

surface [output] to the pump flux transmitted into the microcavity [input]) reaches a plateau of $\sim$ 10% at $P \gtrsim 3P_{th}$. In the plateau regime, the output linearly increases with the input and resembles the characteristics of a conventional semiconductor laser. The maximal efficiency ranges from 3% to 11% depending on excited locations and detuning of the QW and cavity resonance. An efficiency greater than 10% can be obtained. Absorption in the nine 6-nm thick $In_{0.15}Ga_{0.85}As$/GaAs MQWs in the cavity is 12% at $\lambda_p = 785$ nm at room temperature. Therefore, an efficiency greater than 10% implies that essentially all of the carriers photoexcited in the MQWs can recombine radiatively and contribute to laser action.

In a nutshell, the radiation exhibits angularly and spectrally narrow lasing at lasing threshold. The laser radiation is simply a result of matter gain in the active region of cavity exceeding the radiative recombination loss. The emission flux nonlinearly increases with increment pump flux, and the lasing thresholds are different for orthogonal circular components,σ^+/σ^-, of emissions under circularly polarized pumping. Such difference comes from unequal spin-carrier injection in the reservoir of the system. The efficiency 10 % indicates all photoexcited carriers in MQWs contributes to laser radiation.

4.2 Spectral characteristics

Here I present E vs. $k_{||}$ dispersion with photoexcited density dependence and study spectral characteristics of emission. Fig. 4.3 displays normalized dispersion spectra of co-circular emission at selective pump flux. Far below lasing threshold, luminescence from GaAs layers dominates and forms an isotropic angular distribution (not shown). Slightly below lasing threshold, a parabolic E vs. $k_{||}$ appears, which is equivalent to effective cavity resonance modified by carriers in InGaAs MQWs. At the threshold, the radiation becomes spectrally narrow. Far above a threshold, the energy of radiation blue shifts with increasing spectral linewidth while the radiation remains highly directional with the pump flux.

In Fig. 4.4, I study the spectral characteristics. When the pump flux is increased from P = 0.5

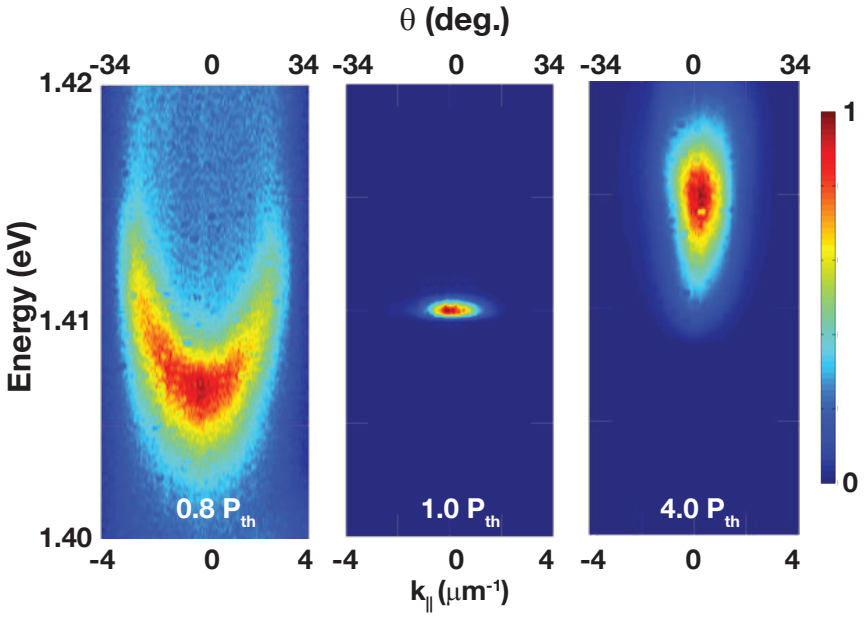

Figure 4.3 **E vs. $k_{||}$ dispersion.** Angle-resolved spectroscopy at P = 0.8, 1 and 4 P_{th}.

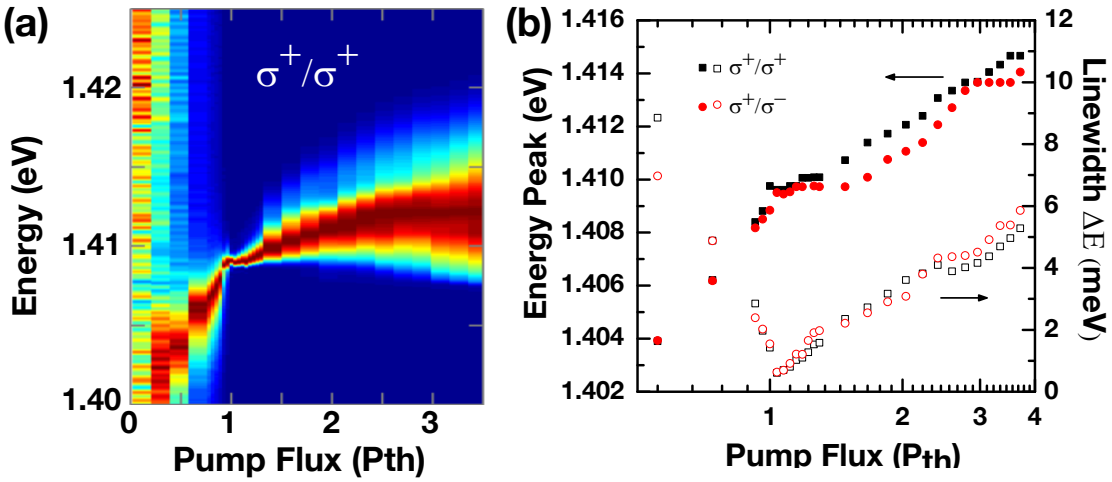

Figure 4.4 **Luminescence characteristics.** (a) 2D false-color images of microcavity luminescence/lasing spectra vs. the pump flux for co-circular (σ^+/σ^+, left panel) and cross-circular (σ^+/σ^-, right panel) components. Spectra are normalized with respect to the co-circular component (σ^+/σ^+) for each pump flux. Note that the intensities of the σ^+/σ^- spectra for $0.8\ P_{th} < P < 1.3\ P_{th}$ (shaded area) are scaled up by a factor of 10. (b) Spectral linewidths ΔE (FWHM) and peak energies determined from the emission spectra in (a).

P_{th} toward the threshold, luminescence blue shifts by ≈5 meV, whereas the linewidth ΔE decreases from about 10 meV to 0.3 meV. Fig. 4.4(b) shows the linewidth ΔE and the peak energy of the co-

and cross-circularly polarized spectra at $k_{\parallel} = 0$ under a circularly polarized (σ^+) pump. The linewidth is defined as full width at half maximum (FWHM) of the spectral distribution. Slightly above the threshold ($P_{th} < P < 1.5\,P_{th}$), spectrally narrow ($\Delta E \approx 0.3$ – 1.0 meV) radiation emerges with a nonlinear growth in magnitude, whereas the peak energy remains constant. Far above the threshold ($P > 1.5\,P_{th}$), the spectral linewidth increases to more than 2 meV. The overall emission energy shifts with the increasing pump flux are more than 10 meV, which is significantly larger than the corresponding energy shift of the cavity stop band (<2 meV). The large energy shift originates from photo-modulated cavity resonance shifting, which will be explicitly presented in Sec. 4.5. The spectral broadening is attributed to (1) more energy region reaches lasing condition (the gain exceeds radiative loss in the active region of the cavity) under more photoexcited carriers injected; (2) time-integrated spectral shift of emission due to the time-dependent cavity resonance change. It is noticed that in far above the threshold region, co- and cross-circular components both lase with the rising peak energy while retaining an energy splitting of ≈1–2 meV. The splitting is a result of different time-integrated spectral dynamics for σ^+ and σ^-, and I will explain it in detail at the end of Sec. 4.4 with Fig. 4.11.

4.3 Emission polarization properties

As aforementioned in the previous section, a spontaneous buildup of the circularly polarized radiation occurs at a critical photoexcited density. Here I discuss the emission polarization properties as functions of photoexcited density as well as excitation polarization change. The polarization state can be characterized by the Stokes three-vector $s = \{s_1, s_2, s_3\}$, which is defined in Sec. 3.2.4.

Fig. 4.5 demonstrates the degree of circular polarization *DoCP* (s_3 component in Stokes three-vector) with pump flux dependence. Below the threshold, the radiation is unpolarized ($\bar{s}_3 \approx 0$). Slightly above the threshold ($P_{th} < P < 1.2\ P_{th}$), the radiation is highly circularly polarized ($\bar{s}_3 > 0.95$). For $P > 1.5\,P_{th}$, the radiation becomes elliptically polarized with reduced $\bar{s}_3$ as a result of increasing radiation with an opposite helicity. When the helicity of the circularly polarized

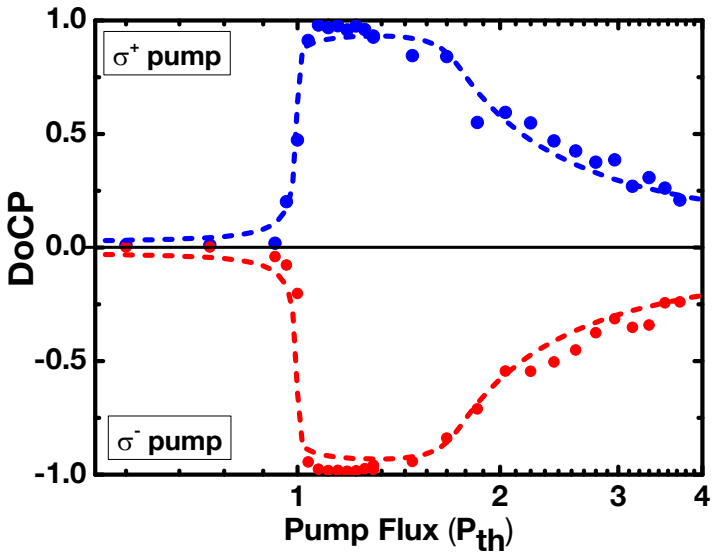

Figure 4.5 **Emission polarization vs. pump flux.** The degree of circular polarization *DoCP* ($\bar{\rho}_c$), determined from the luminescence integrated near $k_{||} \approx 0$ ($|k_{||}| < 0.3\ \mu\text{m}^{-1}$) under a σ^+ or σ^- circularly polarized pump. The dashed lines are the calculated emission flux and the $\bar{\rho}_c$, with a spin-dependent stimulated process assumed (see Section: Theoretical Model)

pump is switched, *DoCP* changes in sign but maintains the same magnitude, i.e., the polarization state is symmetric with respect to the helicity of the pump. The pump flux-dependent *DoCP* is quantitatively reproduced (dashed lines in Fig. 4.5) by a rate-equation model assuming a spin- and density-dependent stimulated process, which is further described in Sec. 4.5.2.

Another manifestation of the spin-dependent process is highly circularly polarized lasing even under a nonresonant elliptically polarized optical excitation (Fig. 4.6). Here, the pump flux transmitted into the microcavity sample is kept constant with varying pump circular polarization (s_3^p, represented by the pump Stokes vector tracing a meridian at the Poincaré sphere shown in Fig. 4.6(a)). When the initial spin-dependent population imbalance is controlled by variation of s_3^p, the *DoCP* of the lasing radiation ($\bar{s}_3$) can exceed that of the pump for $1.0P_{th} < P < 1.5P_{th}$ (Fig. 4.6(b)). Such a spin amplification arises from the "gain" anisotropy in the presence of two threshold pump fluxes for two helicities of laser radiation, typically denoted as $JT1$ and $JT2$ in the literature on spin-controlled VCSELs [83, 84, 85]. Highly circularly polarized lasing ($\bar{s}_3 > 0.8$) occurs even when the s_3^p is as low as 0.5 (altitude $\phi = 30°$). Next, I consider a polarization-dependent external

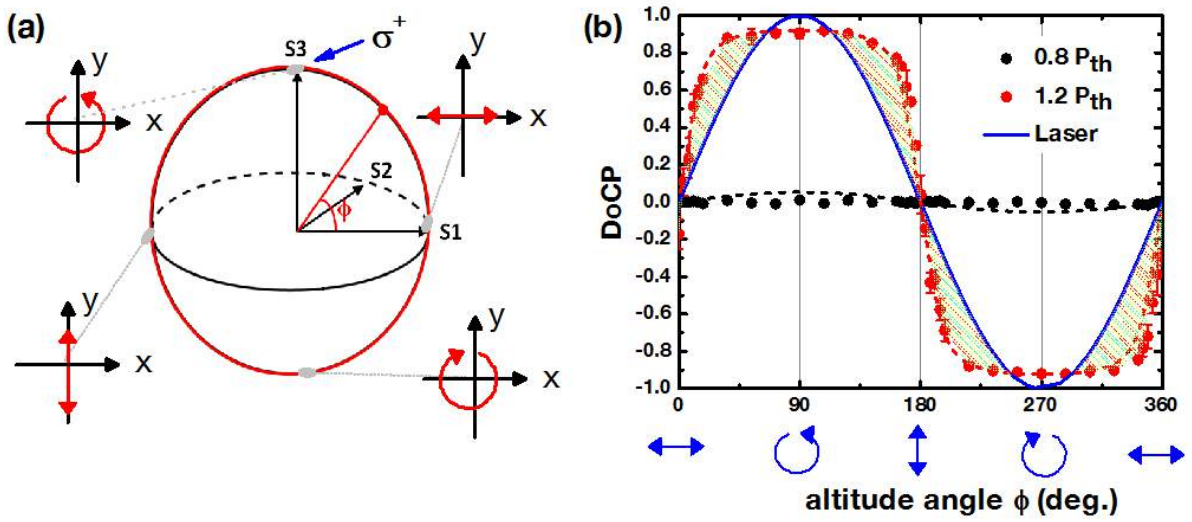

Figure 4.6 **Spin-amplification effect.** (a) Representation of polarization states (Stokes vectors) in a Poincaré sphere. The pump polarization is varied along the meridian in the s_1-s_3 (x-z) plane. (b) The time-integrated *DoCP* of the spin-polarized laser radiation as a function of pump *DoCP* (ρ_c^p) (blue line) at 0.8 (black dots), 1.0 (magenta dots), and 1.2 P_{th} (red dots). The pump flux is maintained at a constant when ρ_c^p is varied. For a specific ϕ, only the η_{ex} of the majority polarized emission component is shown (σ^+ for $0^\circ \leq \phi < 180^\circ$ and σ^- for $180^\circ \leq \phi < 360^\circ$).

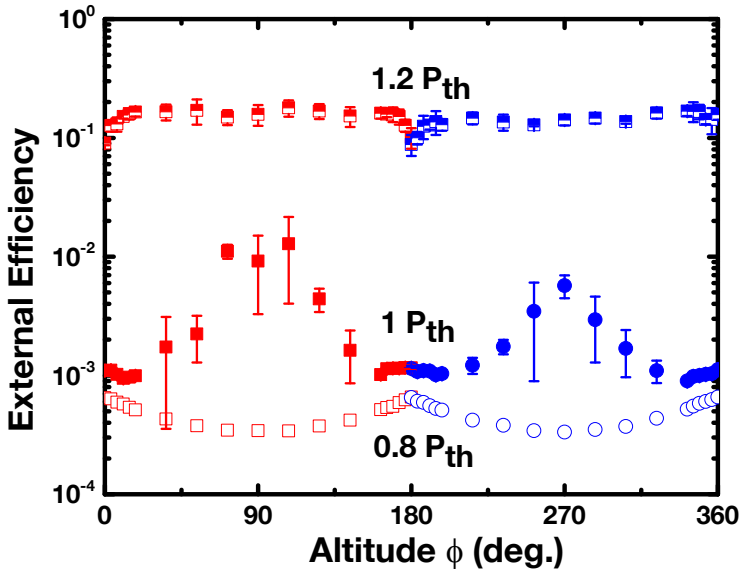

Figure 4.7 **External Efficiency.** External quantum efficiency (η_{ex}) vs. pump *DoCP*, represented by the altitude ϕ) at 1.2, 1.0, and 0.8 P_{th}. For a specific ϕ, only the η_{ex} of the majority polarized emission component is shown (σ^+ for $0^\circ \leq \phi < 180^\circ$ and σ^- for $180^\circ \leq \phi < 360^\circ$). η_{ex} of the minority component is not shown because of a low signal-to-noise ratio for $\rho_c^p \sim \pm 1$. Error bars represent the standard deviation of η_{ex} over five measurements.

efficiency ($\eta_{ex}^{\pm}$) (Fig. 4.7), which is defined as the ratio of the polarized emission flux emanating from the front surface (output) to the pump flux transmitted into the microcavity of the same polarization (input). The external efficiency η_{ex} of the majority polarized emission component is less than 10^{-3} below the threshold, and increases by two orders of magnitude at 1.2 P_{th}. In both cases, η_{ex} is insensitive to s_3^p. At the threshold, η_{ex} exceeds 10^{-2} for $s_3^p \approx 1$ ($\phi = 90°, 270°$), whereas it remains $\sim 10^{-3}$ for $s_3^p \approx 0$ ($\phi = 0°, 180°$). The low η_{ex} below the threshold is due to significant loss through nonradiative recombination, reabsorption, and emissions into other nonlasing modes. With the increasing pump flux, a stimulated process dominates over the loss and yields a dramatic increase in η_{ex} above the threshold. A competition between loss and spin-dependent stimulation can result in the observed "spin amplification" ($\bar{s}_3 > s_3^p$) effect under elliptically polarized pumping, which is qualitatively reproduced by the aforementioned model.

4.4 Dynamics and energy relaxation of luminescence

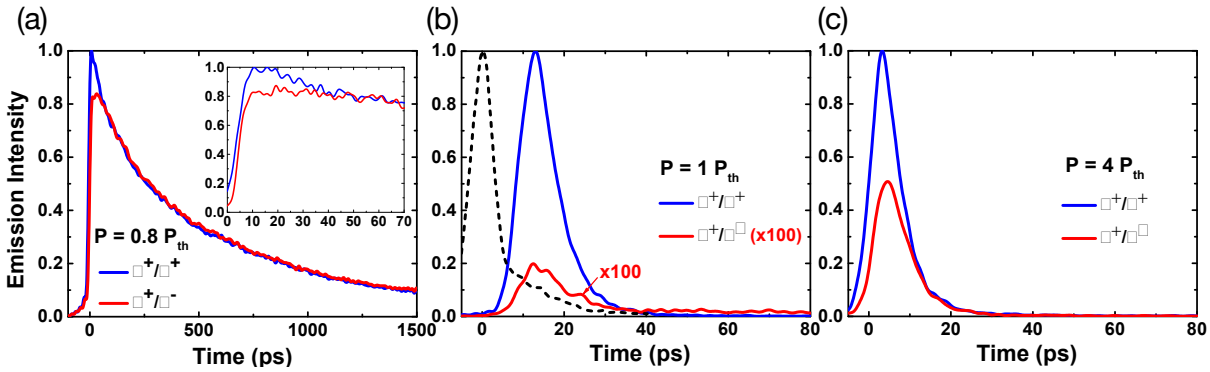

Figure 4.8 **Luminescence dynamics.** Polarized time-dependent luminescence at $k_{||} = 0$ for selective power $P = 0.8$, 1 and 4 P_{th} under a circular polarized (σ^+) pump. Blue (red) curves represent the co-circular $I^+(t)$ [cross-circular $I^-(t)$] components. Note that the cross-circular component shown at $P = P_{th}$ is multiplied by a factor of 100. The time zero is determined from the instrument response (black dashed curve), which is measured via pump laser pulses reflected off the sample surface. The time traces are spectrally integrated (temporal resolution $\approx$ 5 ps).

To understand the mechanism of the spin-polarized laser action, studying the polarization dynamics through time-resolved polarimetry and spectroscopy is needed. Fig. 4.8 shows the selected

time-resolved co- and cross-circularly polarized luminescence [$I^{\pm}(t)$] under a σ^{+} circularly polarized pump. Below the threshold, the time-dependent $s_3(t)$ reaches ~0.1 when the luminescence reaches its peak, and then it decays with a time constant less than 10 ps, as demonstrated by the minimal transient difference between $I^{+}(t)$ and $I^{-}(t)$ at $P = 0.8\ P_{th}$ (Fig. 4.8(a)). At the threshold, the co-circular component commences the pulsed laser action within 30 ps, whereas the cross-circular component remains negligible [$I^{+}(t)/I^{-}(t) > 100$] (Fig. 4.8(b)), resulting in high $s_3(t)$ within first 30 ps. The cross-circular laser pulse commences at $P > 1.5 P_{th}$ (Fig. 4.8(c)).

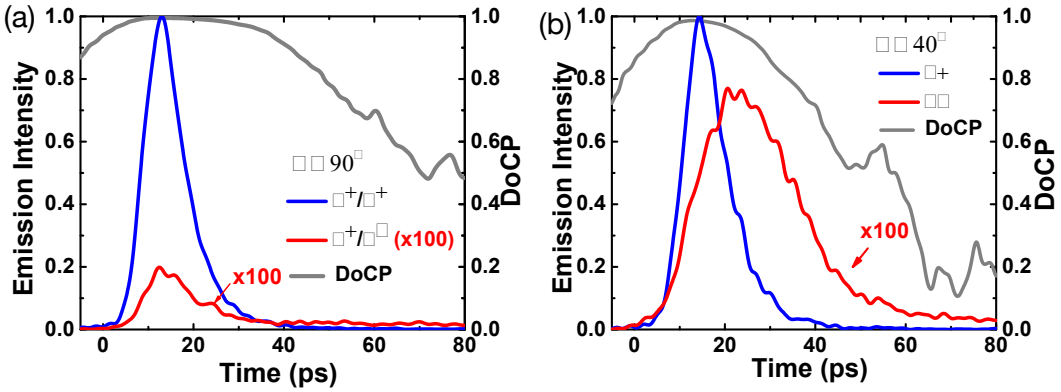

Figure 4.9 **Spin dynamics of photoexcited carriers at lasing threshold.** Polarized time-dependent luminescence at $k_{||} = 0$ for $P = P_{th}$ under circularly ($\phi = 90°$) and elliptically $\phi = 40°$ polarized pump. The corresponding DoCP(t) are represented by gray lines.

Fig. 4.9 illustrates $s_3(t)$ of emission (gray lines) at circularly and elliptically polarized excitation at lasing threshold. The maximum of $s_3(t)$ is closed to unity, and spin relaxation times (decay time of $s_3(t)$) under two excitation cases are about 70 ps. These results are indicative of a spin-dependent stimulated process through which spin polarization is amplified [56, 57, 86, 87, 88, 89].

The temporally and spectrally resolved measurements are further conducted, as shown in Fig. 4.10. At the threshold, the radiation remains spectrally narrow, with a peak energy that is nearly constant with time. Above the threshold, the radiation expands spectrally when the laser action commences, and it gradually red shifts with time. In addition, polarimetric measurements reveal a circularly polarized high-energy component during the initial 10–20 ps pulsed radiation, followed by an unpolarized low-energy one for $P > 1.5\ P_{th}$. Fig. 4.11 presents cross-sectional transient spec-

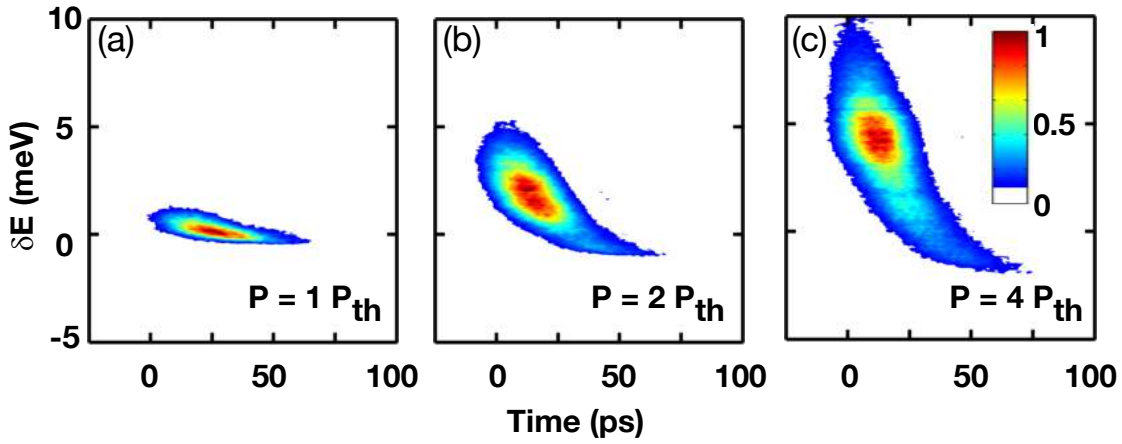

Figure 4.10 **Dynamics and energy relaxation.** Temporally and spectrally resolved streak spectral images of the co-circular component $I^{+}(\delta E, t)$ at P = 1.0, 2.0, and 4.0 P_{th}. The y-axis (δE) is offset with respect to 1.408 eV, the lasing energy at P_{th}. The temporal resolution is ≈30 ps because of the grating-induced dispersion.

tra at 4 P_{th} for σ^{+}/σ^{+} (red) and σ^{+}/σ^{-} (blue) emission components and reveals aforementioned polarization properties. Moreover, the time-integrated transient spectra results in different mean energies for these two components, giving energy splitting shown in Fig. 4.4 (b).

4.5 Theoretical model

To understand the spin-dependent polarization and spectral characteristics, we propose that when the chemical potential of EHP exceeds the bare cavity resonance E_c, a fraction of e-h pairs near the effective E_c forms correlated e-h pairs. Fig. 4.12 shows the energy levels of QWs and E_c. Under high-intensity pumping, the chemical potential as high as 80 meV above band gap exceeds the second quantized level of QWs. The E_c shifts resulting from effective refractive index change in the system due to high-density EHP. Near the E_c a fraction of the reservoir of EHP converse to correlated e-h pairs n_0, giving radiative decay. Once the conversion overcomes the decay and n_0 exceeds critical density, a stimulated emission prevails and results in nonlinearly population increase in n_0 and in laser radiation. In the following section, we briefly introduce the connection of experimental result with our tentative explanation.

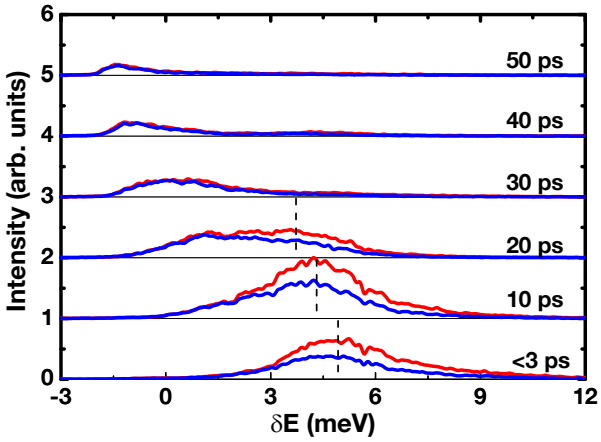

Figure 4.11 **Transient lasing spectra at $P = 4P_{th}$.** Cross-sectional transient spectra at specified time delays extracted from the temporally and spectrally resolved streak images of a sample. Transient spectra are averaged over 5 ps and normalized to the maximal peak intensity of the co-circular component. The spectra are equally scaled but offset vertically by 1. Red lines represent the co-circular (σ^+/σ^+) component, while blue lines represent the cross-circular (σ^+/σ^-) one. The energy scale is measured with respect to 1.408 eV, which is the peak lasing energy at the threshold P_{th}. In initial time delay of few ps after pulse excitation, the emission is spectrally broad and blueshifts by about 5 meV. For delays less than 20 ps, the co- and cross-circular components have the same spectral peak energy (vertical dashed lines), suggesting carriers interactions with same spins and opposite spins are comparable magnitudes. The spectral peak energy is determined by the total carrier density instead of individual spin-up or spin-down population. On the other hand, the intensity of the co-circular component is higher than the cross-circular component within 20 ps after pulse excitation because the ineffective spin-flipping in reservoir results in imbalance spin-population. The emission spectrum reaches a maximum at about 10 ps, and then gradually decreases in overall magnitude and redshifts with time. The temporal energy redshift in spectra is attributed to a descending chemical potential μ with a decreasing carrier density..

4.5.1 Carrier-induced strong nonlinearity

The observed density- and time-dependent lasing energy shift can be regarded as a result of index-induced cavity resonance shift. The cavity resonance shift (δE_c) is related to the change in the refractive index (δn_c) approximately through $\delta E_c/E_c = -\delta n_c/n_c$, where n_c is the effective refractive index averaged over the longitudinal cavity photon mode. Therefore, a cavity resonance shift $\delta E \sim$10 meV (Fig. 4.4) requires a sizable reduction of the refractive index, i.e., $|\delta n_c/n_c| \sim 0.7\%$. So far quite a few paper have reported significant Δn change ($\Delta n \sim 0.1$) in bulk semiconductors or

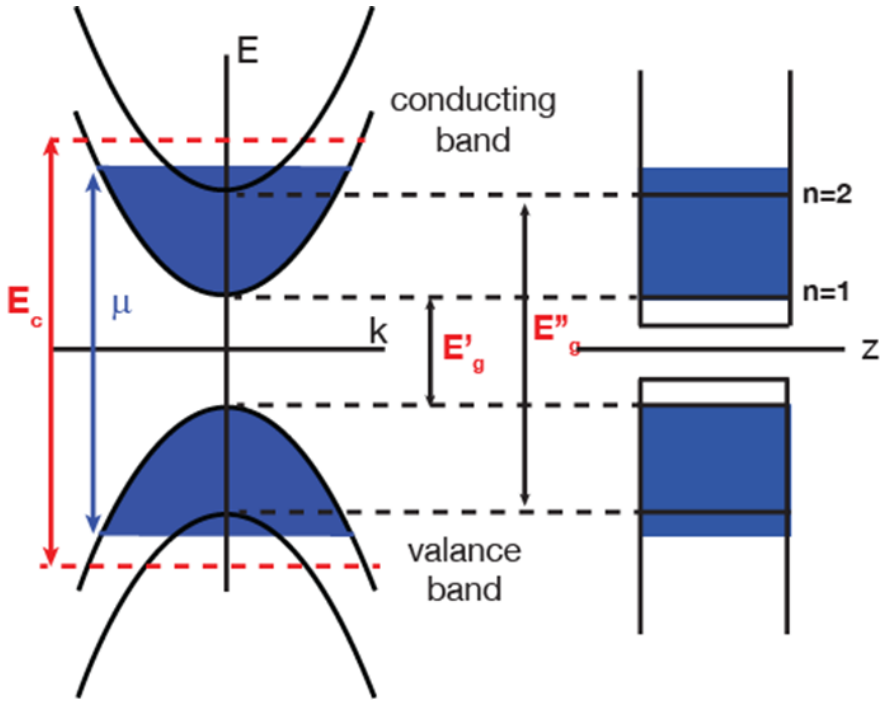

Figure 4.12 **Energy levels of sample.** Schematic of simple band structure of quantum wells in k-space (left) and r-space (right). $E_g^{'}$ and $E_g^{"}$ represent the first and second quantized levels of quantum wells, respectively. In the experiment studied here, the chemical potential μ is about 80 meV above $E_g^{'}$ and is closed to $E_g^{"}$ and bare cavity resonance E_c. The μ may be beneath or exceed E_c, and new cavity resonance $E_c^{'}$ presences as a result of photo-modulated index change. The correlated e-h pairs form near $E_c^{'}$ and play important roles in strong nonlinearity effect observed in research.

QWs [90], but as far as we know none have reported on large Δn in microcavity.

To examine the possibility of the large δE_c with rising chemical potential μ, I would like to illustrate our simulation result based on transfer matrix calculation and carrier band filling effect in QWs. The simulation was developed by my co-worker, Wei Xie, and the result is presented on Fig. 4.13. The effective refractive index change δn in QWs (Fig. 4.13 (a)) can be changed to 0.1 as carrier density increases to 2 P_{th}, where the P_{th} corresponds to e-h density $D_{eh} = 1 \times 10^{18}\, cm^{-3}$. The E_c blue shifts in energy about 10 meV due to the aforementioned index change δn as shown in reflectance spectrum (Fig. 4.13 (b)), which the reflectance is calculated by transfer matrix method. The simple model was performed under two assumption (1) the δn in MQWs mostly results from band filling effect due to μ located near the higher quantized levels of QWs; (2) the refractive

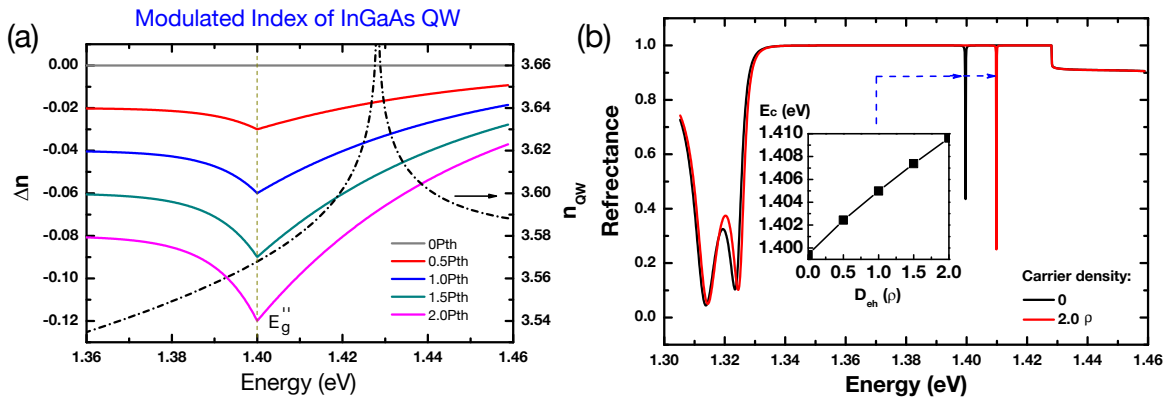

Figure 4.13 **Simulated cavity shifting with band filling.** (a) Effective refractive index change δn in MQWs (solid line) with increasing pump flux. The dashed line represents the refractive index of MQWs without excitation. $E_g^{''}$ is the second quantized level of quantum well. (b) Reflectance spectrum change without (black) and with (red) presence of carrier density. The inset exhibits the cavity resonance shift with increasing photoexcited density. D_{eh} is the photoexcited density at threshold under excitation flux P_{th}.

index of GaAs varies little, as μ is below the band gap of GaAs. Once taking into account the aforementioned assumptions, the model predicts the 10 meV energy blue-shift with $\delta n/n \sim 0.3\%$, and the result indicates the sizable cavity shift is possible with high-density carriers accumulated in QWs.

4.5.2 Spin-dependent stimulated process

To model the spin-controlled lasing processes, we use a set of rate equations with *spin-dependent* stimulated processes. We consider two states populated with spin-polarized electron-hole (*e–h*) pairs: a nonradiative EHP reservoir ($M_{eh}^{\pm}$) and radiative correlated *e–h* pairs at $k_{\|} \approx 0$ ($n_0^{\pm}$). The *e–h* pairs nonresonantly photoexcited by a 2 ps pulsed pump laser at 1.58 eV relax rapidly (<5 ps) to the reservoir via, for example, a spin-preserved scattering process with LO optical phonons. Therefore, we assume that spin-polarized *e–h* pairs are optically injected into the reservoir at a generation rate of $G_p P^{\pm}$, where $P^{\pm}$ is the pump laser flux of helicity $\pm$. The spin flipping time of the *e–h* pairs, $1/W_{sf}$, is less than 10 ps, as demonstrated by the polarized time-dependent PL below the threshold (Fig. 4.8) as well as in a sample without the top DBR mirror layers (Fig. 3.4). The *e–h* carriers in the reservoir can also dissipate through reabsorption and nonradiative recombination (Γ_{loss}). We further assume that a fraction of *e–h* pairs near the effective E_c optically induce

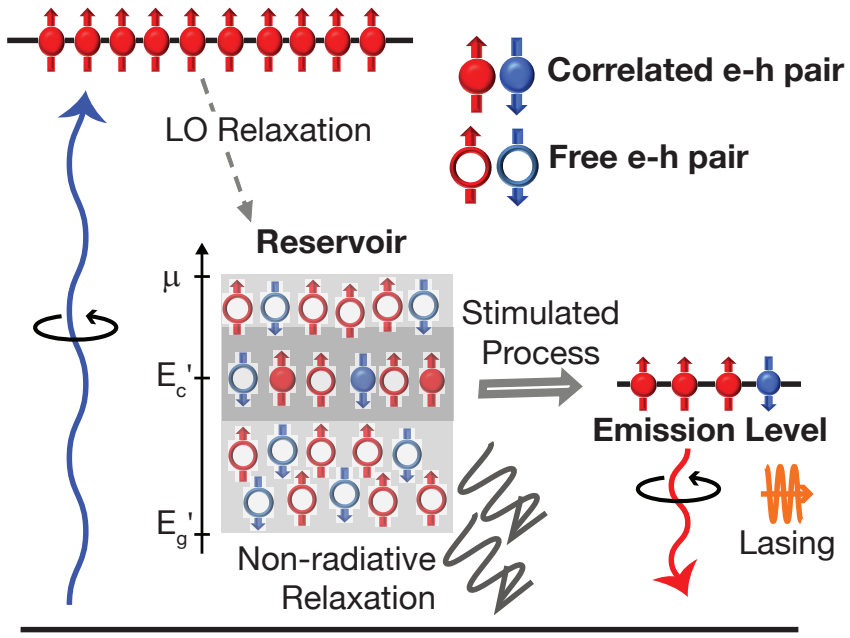

Figure 4.14 **schematics of spin-dependent stimulated emission:**

correlated *e–h* pairs ($N_{eh}^{\pm} = \beta M_{eh}^{\pm}$). The conversion of carriers from N_{eh} to the radiative n_0 state is enabled by the following processes: (a) W_k, a spontaneous conversion from N_{eh}, and (b) W_{ss}, a spin-dependent stimulated scattering from N_{eh}. The n_0 state contributes to the leakage photons measured experimentally at a rate associated with the cavity photon decay rate Γ_c. The lasing dynamics can then be described by the following set of coupled rate equations:

$$\frac{dM_{eh}^{\pm}(t)}{dt} = G_p(t)P^{\pm} \mp W_{sf}\left[M_{eh}^{+}(t) - M_{eh}^{-}(t)\right] - \Gamma_{loss}M_{eh}^{\pm}(t) - W_{ss}(n_0^{\pm})N_{eh}^{\pm}(t)\,n_0^{\pm}(t) - W_k N_{eh}^{\pm}(t)\,,$$
$$\frac{dn_0^{\pm}(t)}{dt} = W_{ss}(n_0^{\pm})N_{eh}^{\pm}(t)\,n_0^{\pm}(t) + W_k N_{eh}^{\pm}(t) - \Gamma_c\, n_0^{\pm}(t).$$

The generation rate of carriers, $G_p(t)$, from a 2 ps pulsed laser pump is represented by a Gaussian distribution with a standard deviation σ = 2 ps. The spin-dependent stimulation rate $W_{ss} = W_0 \times (1 - n_0^{\pm}/n_{sat})$ is phenomenologically set to decrease with density, where the saturation density n_{sat} is obtained by fitting of the pump flux-dependent, stationary *DoCP* ($\bar{s}_3$).

The fittings parameters are as follows: $W_0 = 1/10$ [ps^{-1}], $W_{sf} = 1/10$ [ps^{-1}], $W_k = 10^{-4}$ [ps^{-1}], $\Gamma_{loss} = 1/1000$ [ps^{-1}], $\Gamma_c = 1$ [ps^{-1}], β = 0.015, and n_{sat} = 200. Given a spatial mode area of 10–20 μm^2 for the n_0 state, the calculated threshold density is about $5 - 10 \times 10^5$ μm^{-2},

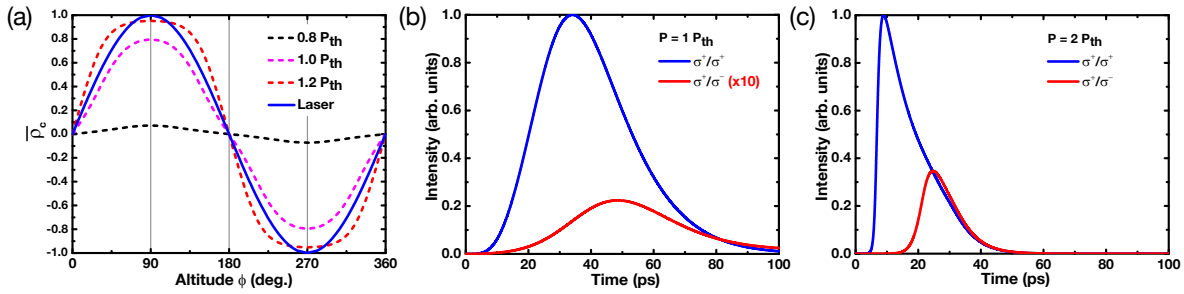

Figure 4.15 **Spin-dependent stimulation.** (a) Calculated stationary *DoCP* ($\bar{\rho}_c$) with varying pump polarization ρ_c^p (represented by the altitude) for $P = 0.8$, 1.0 and 1.2 P_{th}. (b-c) Calculated polarized time-dependent radiation intensity for co-circular σ^+/σ^+ $[I^+(t)]$ and cross-circular σ^+/σ^+ $[I^-(t)]$ components under a σ^+ pump for $P = 1.0$ and 2.0 P_{th}. The theoretical P_{th} is set to the pump flux when the stationary $\bar{\rho}_c = 0.5$ under a fully circularly polarized pump ($\rho_c^p = 1$).

consistent with experimentally measured carrier density per QW at the threshold. This model reproduces the polarized laser output fluxes ($I^{\pm}$) and *DoCP* ($\bar{s}_3$) as a function of pump flux P (Fig. 4.5) and as a function of pump polarization s_3^p (Fig. 4.6 and Fig. 4.15 (a)). The polarized time-dependent PL is also reproduced qualitatively (Fig. 4.8 and Fig. 4.15 (b–c)).

4.6 Discussion and conclusion

The spin-polarized laser studied here has a structure similar to vertical-cavity surface-emitting lasers (VCSELs) [91] and microcavities used for studies of exciton-polariton condensates [17, 20, 19, 34, 26, 21]. In VCSELs, the lasing energy is typically determined by the bare cavity resonance and has limited energy shifts [92, 93] and linewidth broadening [94, 95, 96] with increasing carrier density (see also the Appendix A). The polarization properties of VCSELs are typically affected by crystalline anisotropies [97], but quite a few spin-controlled lasers are reported in the past ten years. [54, 58, 51, 52, 56, 86, 87, 88].

In contrast to conventional spin-controlled lasers (spin lasers), the spin-polarized lasing presented in this study displays (1) substantial *energy blue shift* of more than 10 meV with increasing photoexcited density, (2) spin-dependent energy splittings in the absence of an external magnetic field, (3) ultrafast *sub-10-ps* pulsed lasing, and (4) a high external quantum efficiency of $\sim 10\%$,

which matches the fraction of carriers photoexcited in the MQWs. We attribute the spin-polarized lasing to a spin-dependent stimulated process of correlated e-h pairs formed near effective cavity resonance in a high-density EHP.

CHAPTER 5

TRANSIENT DUAL-ENERGY LASING IN A SEMICONDUCTOR MICROCAVITY

A homogeneous excitation in an inhomogeneous structure may cause exotic luminescence under high-photoexcited injection. In this chapter, I demonstrate sequential lasing at two well-separated energies in the microcavity with the same structure presented in the last chapter. Two spatially overlapped lasing states with distinct polarization properties appear at energies more than 5 meV apart. Under a circularly polarized nonresonant pumping, an ultrafast transient circularly polarized high-energy (HE) state emerges quickly after excitation. This HE state is followed by a pulsed state with a much longer lifetime at a low energy (LE) state. The HE state is highly circularly polarized as a result of a spin-preserving stimulated process while the LE state shows a significantly reduced circular polarization because of a diminishing spin imbalance. In the following sections, these results will be presented in details.

5.1 Spectral characteristics

First, I will introduce the density-dependent energy shifts and linewidths of emission. Fig. 5.1 (a) shows the co-circular σ^+/σ^+ luminescence spectra $[S^+(E)]$ at $k_{\|} \approx 0$ as a function of pump flux. Above the bifurcation pump flux $P_b \equiv 1.1\ P_{th}$, radiation bifurcates into a doublet (*two-state lasing*) with a dominant HE state. In Fig. 5.1 (b), the emission flux of the LE state reaches a plateau near above $1.5 P_{th}$, whereas the emission flux of the HE state continues to increase linearly with the pump flux. Spectrally, the HE and LE states display distinct energy shifts with increasing photoexcited density. Fig. 5.1 (c) illustrates the peak energies of the two states with increasing pump flux. Below P_b, the emission is single-peaked and blueshifts by 6 meV when the pump flux increases from 0.5 P_{th} to $\sim 1.1\ P_{th}$. When the pump flux increases gradually from 1.0 P_{th} to 3.5 P_{th}, the HE state blue shifts linearly by 5 meV, whereas the LE state red shifts by less than 0.5

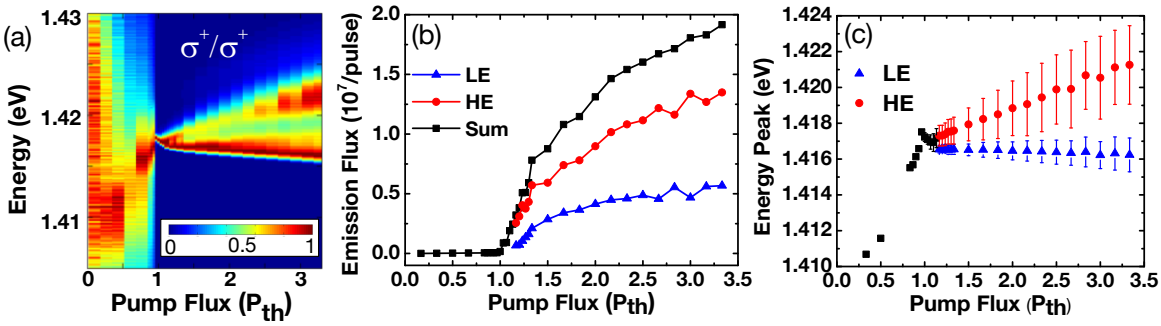

Figure 5.1 **Spectral characteristic of dual lasing.** (a) Normalized time-integrated spectra of the co-circular (σ^+/σ^+) emission component for $|k_{||}| < 3\ \mu\text{m}^{-1}$. (b) Emission flux of the HE state (solid red circles), the LE state (solid blue triangles), and the sum (solid black squares). (c) Peak energies (solid shapes) and linewidths (error bars) of the HE state (solid red circles) and LE state (solid blue triangles). The peak energies below the threshold are represented by the solid black squares. The emission fluxes, peak energies, and linewidths are determined by fitting of the spectra with multiple-Gaussian functions. The photoexcited density at the threshold pump flux (P_{th}) is $n_c \approx 2 \times 10^{12}$ cm^{-2} per quantum well *per pulse*.

meV. This result indicates that the energy difference between the HE and LE states enhances with increasing photoexcited density. Above P_b, the linewidth of the HE state increases from ~0.3 meV at P_{th} to 3 meV at 4 P_{th}. On the other hand, the LE state remains spectrally narrow with a linewidth of 1 meV or less.

Next, I illustrate the spectral characteristics in k-space and r-space. Fig. 5.2 (a) shows the k-space imaging spectra of the co-circular emission component for selected pump fluxes. A nearly parabolic energy versus in-plane momentum (E vs. $k_{||}$) dispersion curve emerge slightly below the threshold ($P \approx 0.8\ P_{th}$). At the threshold (pump flux $P = P_{th}$), the radiation becomes directional (angular-spread $\Delta k_{||} \leq 1\mu m^{-1}$) and spectrally narrow (linewidth $\Delta E \leq 0.3$ meV) (Fig. 5.2 (b)). The time-integrated emission spectra appear to bifurcate into a doublet when the pump flux is increased above 2 P_{th}. The two lasing states are spatially overlapped in-plane, as evidenced in the r-space imaging spectra (Fig. 5.2 (c)).

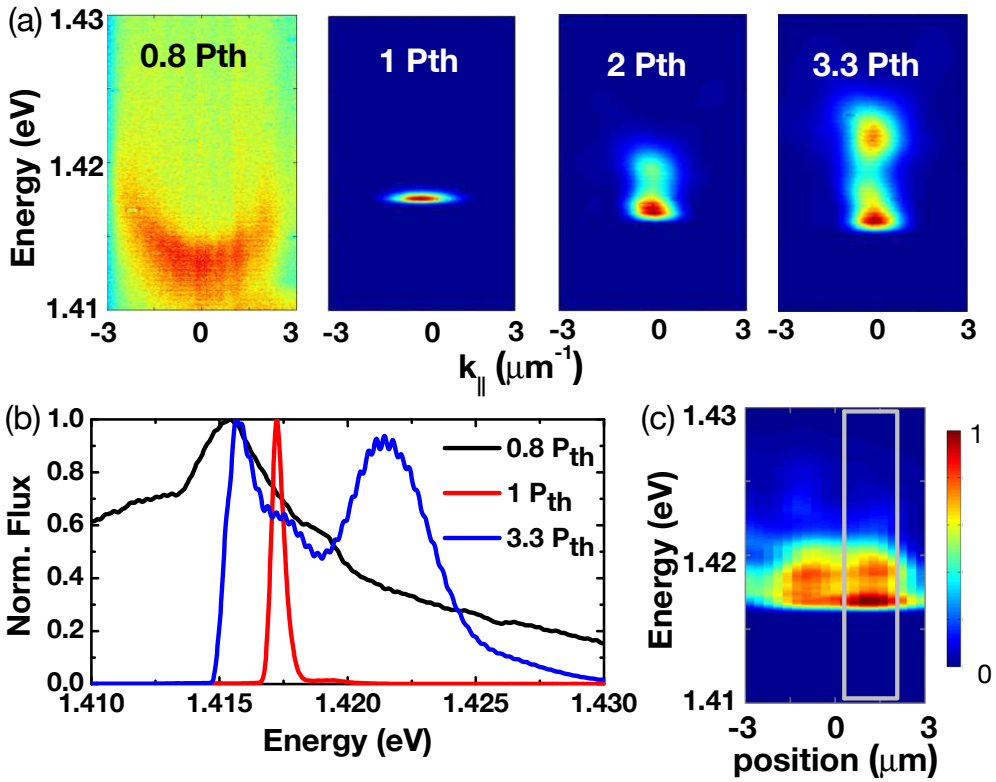

Figure 5.2 **Two-state lasing in a microcavity.** (a) Angularly resolved (k-space) imaging spectra of the co-circular (σ^+/σ^+) emission component at $P = 0.8$, 1.0, 2.0, and 3.3 P_{th}. (b) Time-integrated spectra at 0.8 (solid black line), 1.0 (solid red line) and 3.3 P_{th} (solid blue line). (c) Real-space (r-space) imaging spectra at 2.0 P_{th}. The k-space spectra shown in (a–b) are measured through a pinhole, as represented by the gray box.

5.2 Dynamics of dual-energy lasing

The spectral doublets that appear in time-integrated spectroscopy measurements are temporally separated, as shown in the time-dependent polarized luminescence spectra at $k_{||} \approx 0$ (Fig. 5.3). When two-state lasing occurs, luminescence from the HE state appears within 10 ps after pulse excitation and decays with a time constant $\tau_d' \sim$10 ps. After the HE state diminishes, the LE state appears and then decays with a time constant $\tau_d'' \sim$30–50 ps.

Here I discuss the density and time dependence of the peak energies of the HE and LE states. In the highly photoexcited microcavity studied here, EHP of density ≈ 1 to 5×10^{12} cm^{-2} per QW per pulse are formed following *nonresonant* 2 ps pulse excitation as a result of rapid (<10 ps) energy

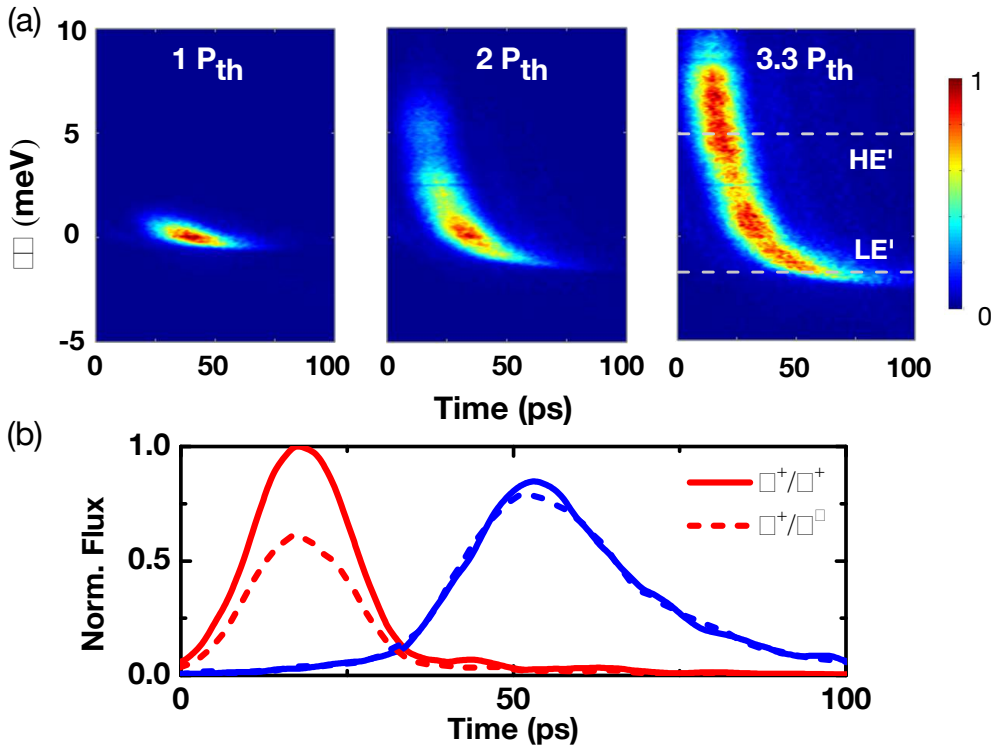

Figure 5.3 **Dynamics of dual lasing.** (a–c) Time-dependent spectra of the co-circular component at $k_{\parallel} \approx 0$ under $P = 1.0$, 2.0, and 3.3 P_{th}. The energy δE is measured with respect to 1.415 eV, the lasing energy at the threshold. (d) Polarized time-dependent luminescence of the HE state at $\delta E = 5$ meV [HE' as indicated in (c)] (solid and dashed red lines) and the LE state $\delta E = -5$ meV [LE' as indicated in (c)] (solid and dashed blue lines) for $P = 3.3\ P_{th}$.

dissipation through optical phonons. When the chemical potential μ of the EHP approaches E_c, the average refractive index near E_c can be considerably modified; the result is a sizable blue-shift of the effective cavity resonance (E_c'). The peak energy of the HE state increases with the pump flux (Fig. 5.1), which can be understood as a result of the light-induced refractive index change and the consequent effective cavity resonance shift [98]. Furthermore, under pulse excitation, the effective cavity resonance E_c' decreases over time toward the bare cavity resonance E_c owing to the temporal decay of the reservoir carriers (Fig. 5.3). Slightly above the threshold, the HE state emerges as a burst of spectrally broad $\sim$10 ps pulsed radiation, spurred by the stimulation of the majority of the optically active carriers. This rapid depletion of the optically active e-h pairs in the reservoir precipitates a drop in E_c'. Afterwards, the LE state ensures the radiation from a local

confinement which is replenished with *e-h* carriers via spatial diffusion (Fig. 5.2 and 5.3). The prolonged replenishment of *e-h* pairs from the reservoir causes a temporal red-shift of the LE state over $\gtrsim$ 50 ps (Fig. 5.3). The increasing pump flux results in an apparent time-integrated spectral red-shift (Fig. 5.1 (c) and 5.3 (b–c)). At cryogenic temperatures, similar multiple bursts of radiation have also been observed in localized exciton-polariton condensates formed in a spatially inhomogeneous microcavity. These dynamic relaxation oscillations appear as the result of the interplay between carrier diffusion (gain) and Bose stimulation (depletion) [31].

5.3 Polarization of dual-energy lasing

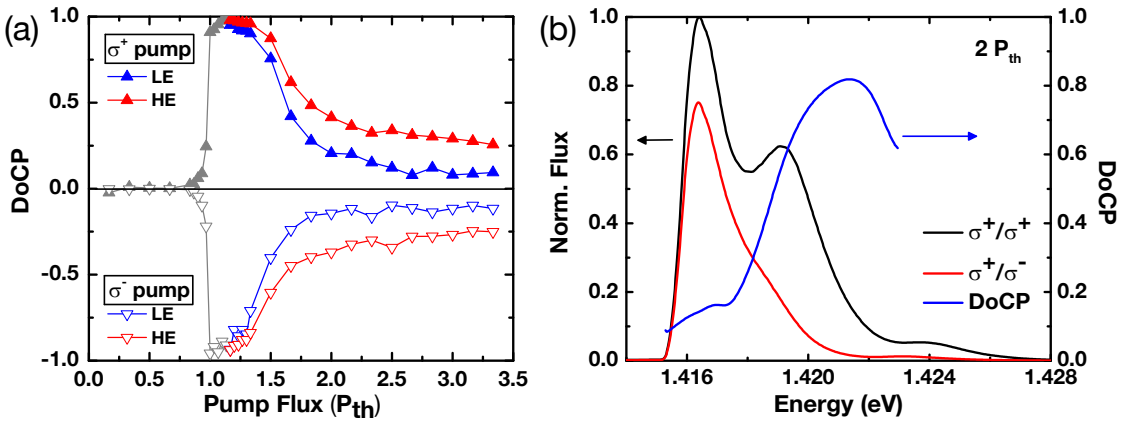

Figure 5.4 **Polarization properties of dual lasing.** (a) Stationary degree of circular polarization ($DoCP = \bar{\rho}_c$) of the HE state (solid and open red triangles) and LE state (solid and open blue triangles) under circularly polarized σ^+ pump (upper part, solid triangles) or σ^- pump (lower part, open triangles). $DoCP = \bar{\rho}_c = (A^+ - A^-)/(A^+ + A^-)$, where $A^\pm$ refers to the areas of co-circular (A^+) and cross-circular (A^-) components of the HE and LE spectral peaks and are obtained by fitting of the time-integrated spectra (Fig. 5.2) with multiple-Gaussian functions. The $\bar{\rho}_c$ of the HE states increases from zero to near unity for $P_{th} < P < 1.2P_{th}$ and decreases gradually to 0.25. The $\bar{\rho}_c$ of the LE states is relatively high (>0.8) initially, but it decrease rapidly to less than 0.1 when the pump flux is increased above 2.0 P_{th}. (b) The time-integrated polarized spectra $S^\pm(E)$ of the co-circular ($\sigma^+/\sigma^+ \rightarrow S^+(E)$, black curve) and the cross-circular ($\sigma^+/\sigma^- \rightarrow S^-(E)$, red curve) components at $P = P_{th}$. The energy-dependent $DoCP(E) = \bar{\rho}_c(E) = [S^+(E) - S^-(E)]/[S^+(E) + S^-(E)]$ (blue curve) shows a maximal $\bar{\rho}_c(E) \approx 0.8$, which is significantly larger than the spectrally averaged $\bar{\rho}_c$ shown in (a).

In Fig. 5.4, I study the polarization properties of the two lasing states. Fig. 5.4 (a) shows the

$\bar{\rho}_c$ of the HE and LE states as a function of pump flux. The $\bar{\rho}_c$ of the HE state rises from nearly zero to unity at threshold, remains above 0.9 for $P_{th} < P < 1.2\ P_{th}$, and decreases gradually to 0.25 at 4 P_{th}. The LE state appears with a sizable $\bar{\rho}_c$ slightly above 1.1 P_{th}, and shows rapidly diminishing $\bar{\rho}_c$ for $P \gtrsim 1.7 P_{th}$. Moreover, an apparent spin-dependent energy splitting of $\sim$1 meV between the co-circular and cross-circular components of the HE state appears, as demonstrated by the selected polarized emission spectra at 2.0 P_{th} shown in Fig 5.4 (b) (see also Ref. [99]). The spectrally resolved $DoCP(E) = \bar{\rho}_c(E)$ also shows the energy-dependent $\bar{\rho}_c$, in which the HE state reaches a maximal $\bar{\rho}_c(E) \approx 0.8$, even at a high photoexcited density. Such a high $\bar{\rho}_c(E)$ occurs despite the sub-10-ps spin relaxation times of electrons and holes in InGaAs/GaAs QWs, a result that is indicative of sub-10-ps carrier cooling and spin-dependent stimulated processes. The rapid cooling results in a sizable spin imbalance in the cavity-induced correlated *e-h* pairs formed near the Fermi edge of the high-density plasmas, whereas the spin-dependent stimulation of these *e-h* pairs amplifies such optical spin polarization in the presence of non-radiative loss [99]. By contrast, the LE state has a vanishing $\bar{\rho}_c$ because of the lack of spin imbalance at a time delay of 50 ps or more after the optical injection of the spin-polarized carriers.

5.4 Discussion

In this study, the HE state is dominated by a macroscopic population of “hot" *e-h* pairs near the Ferm edge via the spin-dependent stimulation. The LE state forms in a confined area of a lateral dimension of $\sim$2–5μm, which is defined by natural crystalline in-plane inhomogeneities (Fig. 5.2). After the radiative recombination of these “hot" *e-h* pairs, the remaining “cold" *e-h* pairs form the LE state that gives spectrally narrow and directional radiation. Therefore, the formation of the LE state hinges on the population of the remaining “cold" *e-h* pairs, which typically becomes significant in samples in which the chemical potential μ can exceed the bare cavity resonance significantly (i.e., $\mu \sim E_g'' \gtrsim E_c$).

Spectral functions resembling the two-state lasing spectra presented here have been calculated

for *e-h* systems in the presence of a cavity by Littlewood et al. [100] and Ogawa et al. [101, 102]. Excitations in exciton condensates [103, 13, 100, 104] or BCS-like *e-h* states [105, 106, 101, 102, 107, 108] can lead to spectral multiplets. Moreover, analogous frequency shifts and doublings of the optical excitations have been reported in Bose gasses [109, 110, 111], in which condensate and thermal components coexist. In general, the doublet in the absorption spectra for normal and condensate components in a cold Bose gas is fundamentally related to the two-fluid model of superfluid helium [112]. In contrast to the aforementioned states of thermal equilibrium, the transient dual-energy lasing presented here is a non-equilibrium phenomenon, in which carrier injection by photoexcitation, energy relaxation, spatial diffusion, and dissipation by both spontaneous and stimulated processes should all be considered. In general, a coupled *e-h*-photon system like the one described here can exhibit diverse energy distributions and polarization properties. For example, the crossover from photon (i.e., weak coupling limit) to exciton-polariton (i.e., strong coupling limit) lasing with decreasing photoexcited density has been studied in terms of the spectral and angular distributions, dynamics, and polarizations of emissions from a microcavity at cryogenic temperatures[107, 113, 67, 68, 114]. In semiconductor quantum wells, 10–100 ps bursts of superfluorescence [115, 116] have been observed in high-density magneto-plasma in the absence of a cavity structure [117, 118, 14, 15].

To clarify the mechanisms of the two-state lasing effect found in the samples studied here, it is necessary to conduct further temporally and spatially resolved spectroscopies to characterize the energy distribution and relaxation of nonradiative *e-h* carriers. For example, one could use a pump-probe spectroscopy to show any time- or density-dependent resonances of the high-density EHP that is coupled to the cavity light field. Eventually, it will become possible to develop multiple-pulse lasing with energies and polarizations that can be controlled by external optical stimulus [99] and lateral confinement [98].

CHAPTER 6

MULTIPLE-PULSE LASING FROM AN OPTICALLY INDUCED HARMONIC CONFINEMENT

Optical trapping contributes to the study of inter-particle interactions in quasiparticle condensate, and can be exploited to create optoelectronic devices. Due to the advance of beam shaping technique, optically induced confinement with controllable size and shape has become possible. In this section, I report the optical visualization of macroscopic quantized states from an optically induced harmonic confinement in a highly photoexcited microcavity at *room temperature*. Photoexcitation creates mainly free pairs of electrons and holes in an III-V-based semiconductor QW as a result of thermal ionization at high temperature [119, 120]. In the highly photoexcited microcavity studied here, the nonlinearly photo-modulated refractive index results in a sizable effective cavity resonance shift, which enables optically induced confinement. In an optical confinement initiated by spatially modulated nonresonant ps pulse excitation, sequential multiple-pulse lasing radiation commences at several quantized energy levels. The transverse optical modes in a spatially modulated refractive index can also be understood as an optically induced potential for a fictitious quasiparticle, e.g., correlated *e-h* pairs resulting from the effective coupling to the cavity light field. Multiple-pulse lasing radiation from quantized states in a harmonic confinement (potential) manifests as a result of the time- and energy-dependent competition between the gain and reservoir carrier relaxation. In the following, I will detail these results. The experimental setup is the same mentioned in chapter 4, but the beam profile is swapped by a double-hump-shaped beam to fixate the orientation of the optically defined potential (Fig. 6.1 (a–b)).

6.1 Visualization of harmonic oscillators in optical trapping

Real-space (r-space) imaging spectra provide direct visualization of the optical potential. Fig. 6.1 (c–d) shows the r-space imaging spectra of a narrow cross-sectional strip across the trap. A nearly

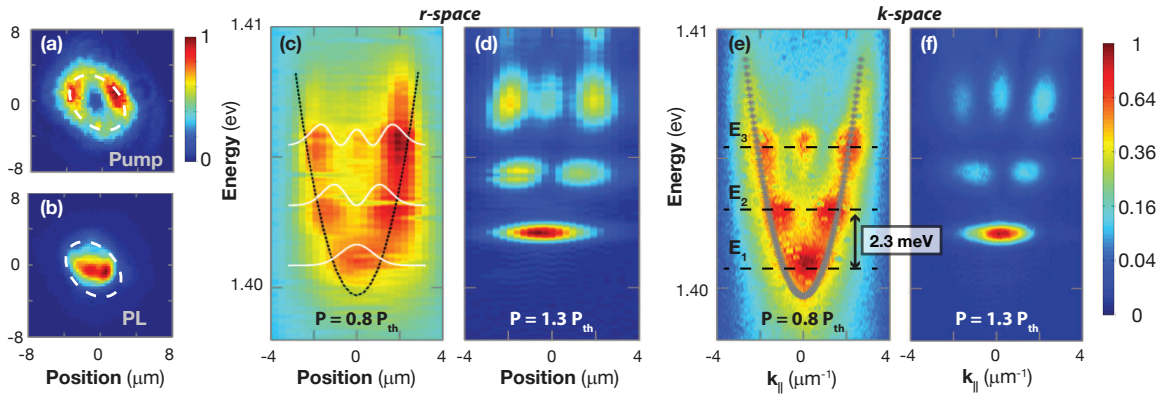

Figure 6.1 **Visualization of the macroscopic harmonic states.** (a) Intensity image of the ring-shaped pump laser beam. (b) Photoluminescence (PL) image under a pump flux of about 1.3 P_{th}, where the threshold pump flux $P_{th} = 1.8 \times 10^8$ photons per pulse. The white dashed line represents the intensity peak of the pump. PL emerges at the center with a minimal overlap with the annular pump laser beam. (c–d) r-space imaging spectra at $P = 0.8\ P_{th}$ and $1.3\ P_{th}$. The black dashed line represents the harmonic confining potential $V(x)$, whereas the white lines represent the spatial probability distributions of the lowest three states of a corresponding harmonic oscillator. (e–f) k-space imaging spectra. The energy splitting is $\hbar\omega \approx 2$ meV, consistent with the quantized energy of a quantum oscillator for a particle with mass $m^* = 3 \times 10^{-5}\ m_e$, as determined by the E vs. $k_{||}$ dispersion (doted grey line). The quantized modes spectrally blue shift about 1 meV from $P = 0.8$ to $1.3\ P_{th}$, whereas the quantized energy splitting remains the same. The potential and spectral shifts are due to a density-dependent increase in the chemical potential of the high-density e-h plasma in the reservoir.

parabolic potential well of $\sim$10 meV across 3 μm is revealed. Such a quasi-1D harmonic potential, $V(x) = 1/2\ \alpha x^2$, is spontaneously formed under 2 ps pulse excitation. The resultant radiation appears in-between the two humps, a few micrometers away from the pump spot. The r-space intensity profiles agree with the probability distributions of the quantized states of a harmonic oscillator (harmonic states). The deviations of the actual potential from a perfectly harmonic trap result in slightly asymmetric luminescence intensity distributions. These standing wave patterns form in the self-induced harmonic optical potential when a macroscopic coherent state emerges. At a critical density, the occupation number of correlated e-h pairs (n_i) in these quantized harmonic states approaches unity when the conversion from the reservoir (N_{eh}) overcomes the decay of the harmonic states. Consequently, when a stimulated process ($\propto N_{eh} n_i$) prevails, n_i and the resultant radiation increase nonlinearly by a few orders of magnitude with the increasing N_{eh}.

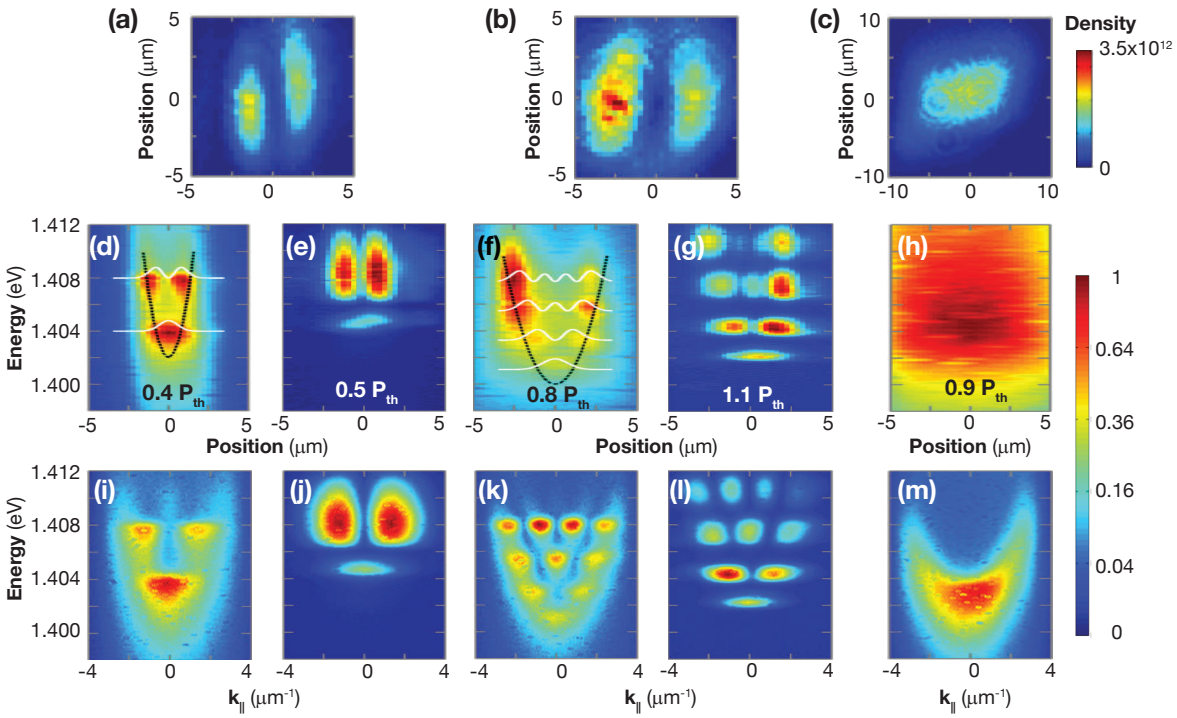

Figure 6.2 **Quantized states in optically controlled confining potentials.** (a–c) Optical images of pump beam profiles at the front sample surface for two double-hump-shaped and one flat-top focal spots. The false color represents the photoexcited density (cm^{-2}) per quantum well per pulse at 0.4 P_{th} for (a) and at 0.8 P_{th} for (b). $P_{th} = 1.8 \times 10^8$ per pulse, as defined in the main text. The lasing thresholds are 0.4 P_{th} for (a) and 0.8 P_{th} for (b). The peak-to-peak distances of these two double-hump-shaped pump beams are 5 μm and 3 μm, respectively. (d, f, h) Real-space imaging spectra measured below the threshold. The black dashed line shows the effective harmonic potential, whereas the white lines represent the spatial probability distributions of the lowest few states of a corresponding quantum oscillator. The quantized energy splittings for (d) and (f) are 4.0 and 2.2 meV, respectively. The false color represents the square root of intensity. (e, g) Real-space imaging spectra under above-threshold pump. (i-n) Corresponding k-space imaging spectra under below-threshold (i,k,m) and above-threshold (j, l)

An even more regular pattern appears in k-space imaging spectra (Fig. 6.1 (e–f)). The E vs. $k_{||}$ dispersion measured below the threshold allows the direct measurement of the effective mass $m^* = 3 \times 10^5\, m_e$, where m_e is the electron rest mass. Moreover, the strength of the optically defined harmonic potential α can be tuned through a variation in the spatial distance between two humps of the pump beam (Fig. 6.2). The energy quantization ($\hbar\omega$) varies with $\sqrt{\alpha/m^*}$, while the emission patterns evolve into the probability distributions for a particle with an effective mass m^* in $V(x)$ (Fig. 6.2).

6.2 Dynamics of multiple-pulse lasing

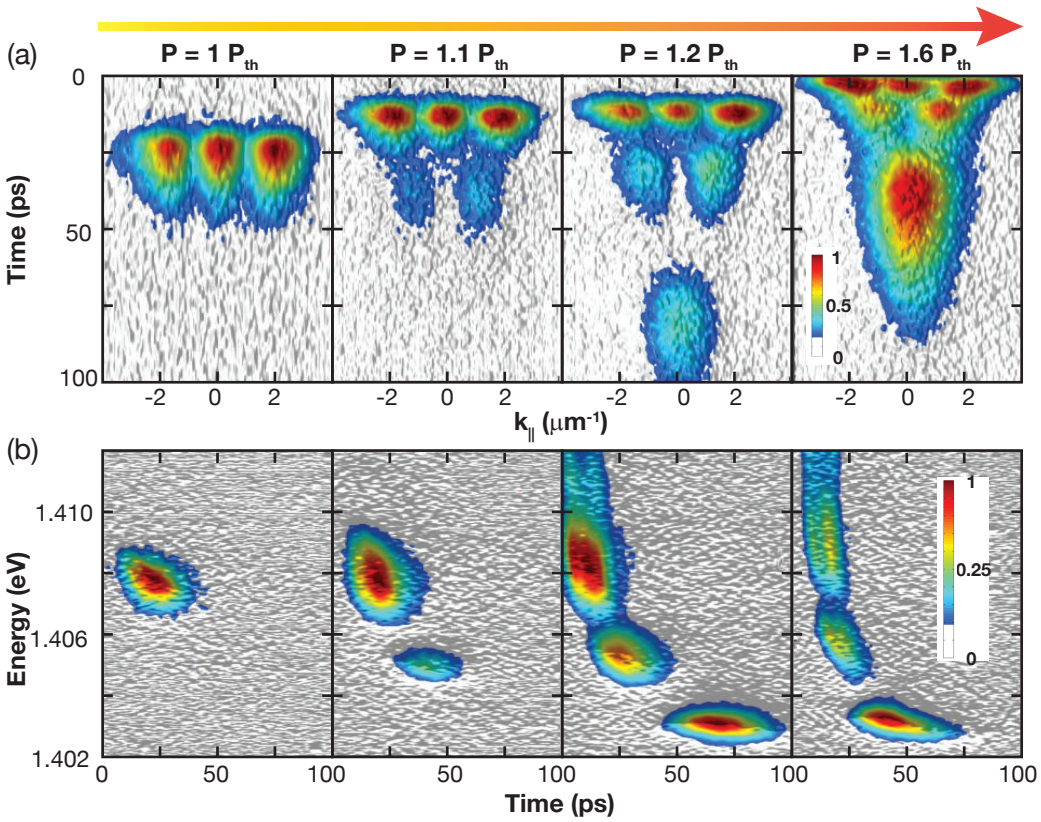

Figure 6.3 **Dynamics of harmonic states.** (a) Time-dependent luminescence in k-space at $P = 1.0$, 1.1, 1.2 and $1.6P_{th}$. The E_3, E_2 and E_1 states appear sequentially with the increasing pump flux. The rise times decrease with the increasing pump flux for all states. (b) Time-dependent spectra in r-space. The false color represents normalized intensities.

Temporally, these harmonic states emerge sequentially and display distinct density-dependent dynamics. In Fig. 6.3 (a), we study the time evolutions of three harmonic states in the k-space, and Fig. 6.3 (b) is the time-resolved spectra revealing the energy relaxation of these three states. The corresponding time-integrated imaging spectra in k-space are shown in Fig. 6.4. At a critical photoexcited density, the high-energy E_3 state arises $\sim$ 25 ps after pulse excitation and lasts for $\sim$ 20 ps. The corresponding pump flux is defined as the threshold (P_{th}). With the increasing pump flux, the E_2 state emerges $\sim$ 25ps after E_3 at 1.1 P_{th}, whereas the *ground* E_1 state appear 50ps after E_2 at 1.2 P_{th}. In the optically induced harmonic confinement studied here, the effective cavity reso-

nance E_c' decreases with time as a result of the decay of reservoir carriers. However, the conversion from the reservoir to specific confined E_i state can be efficient only when E_c' is resonant with E_i. Such a temporal decrease in E_c' results in a time- and energy-dependent conversion efficiency for these confined harmonic states (Fig. 6.5) and consequent multiple-pulse lasing radiation above the critical density threshold.

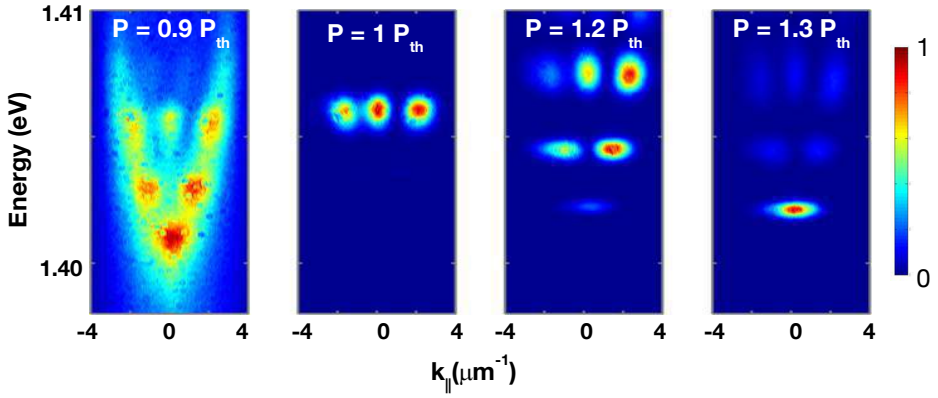

Figure 6.4 **K-space imaging spectra.** The energy vs. in-plane momentum $k_{||}$ dispersion corresponding to the data set in the main paper with the increasing pump flux from 0.9 to 1.3 P_{th}. The quantized E_3, E_2, and E_1 states lase in sequence with the increasing pump flux. E_3-state lasing commences first, followed by E_2-state lasing at about 1.2 P_{th}, and then E_1-state lasing appears at 1.3 P_{th} and dominates over the other two states at a higher pump flux.

6.3 Harmonic oscillators properties with density dependence

We further analyze the emission flux and energy of these harmonic states by using time-integrated spectra measured with increasing photoexcited density (Fig. 6.6 and Fig. 6.7). Far below the lasing threshold ($P < 0.4\ P_{th}$), emission is dominated by luminescence from GaAs spacer layers. When the pump flux is increased, the emissions from the correlated e-h pairs states become increasingly dominant, and the E_3 state eventually lases at the threshold. The emission fluxes of all three states increase nonlinearly by more than two orders of magnitude across a threshold and then reach a plateau at a saturation density (Fig. 6.6 (a)). On the other hand, the emission energy of these three states increases to a constant with the increasing pump flux (Fig. 6.6 (b)). The energy spacing $\hbar\omega$

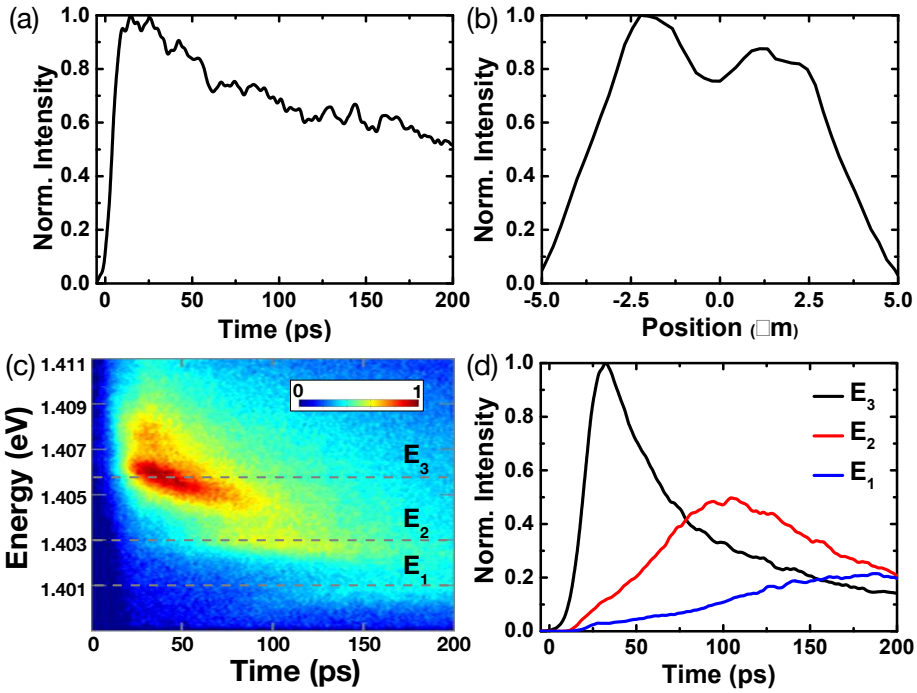

Figure 6.5 **Harmonic oscillator: below-threshold dynamics.** (a) Time-dependent spectrally and spatially integrated luminescence at $P = 0.9\ P_{th}$. The luminescence decays with a > 500 ps time constant largely because of the nonradiative loss. (b) Spatial luminescence distribution integrated up to a delay of 50 ps after pulse excitation, revealing a double-hump-shaped profile. (c) Time-dependent luminescence spectra at $P = 0.9\ P_{th}$. The false color represents the square root of the luminescence intensity. (d) Time-dependent luminescence intensity for the E_3 (black), E_2 (red) and E_1 (blue) harmonic states. The intensity is integrated over a spectral range of 1 meV centering the energies, as indicated by the dashed lines in (c).

only increases slightly with density. The spectral linewidths increase slightly for the E_1 state, by about a factor of 10 for the E_3 state. Next, we study the density-dependent dynamics. Fig. 6.6 (c) shows the rise times and pulse durations for E_3, E_2, and E_1. The product of the variances of the spectral linewidth (ΔE) and the pulse duration (Δt) is found to be close to that of a transform-limited pulse: $\gtrsim 4\hbar$ and $\approx 1\hbar$ for the E_3/E_1 and E_2 states, respectively. These harmonic states are macroscopically coherent states with finite phase and intensity fluctuations induced by interactions.

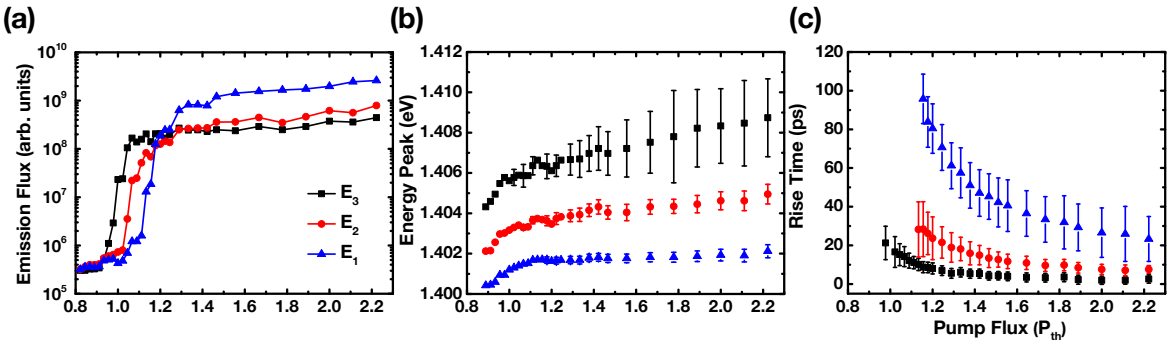

Figure 6.6 **Density dependence of harmonic states.** (a) Temporally and spectrally integrated emission flux vs. pump flux. All three modes display non-linear increases in intensity by more than two orders of magnitude, and saturate at 1.1, 1.2 and 1.3 P_{th}, respectively. (b) Peak energy (solid shapes) and linewidths $2\Delta E$ (error bars) vs. pump flux. These states spectrally blue shift by 1 to 4 meV. The spectral linewidths (ΔE) and pulsewidths (Δt) are reciprocal with a product of $\Delta E \times \Delta t \approx 4\hbar$ ($\hbar$) for E_3 and E_1 (E_2), which is closed to the uncertainty (Fourier-transform) limit. (c) Rise time vs. pump flux for the three states E_1 (blue), E_2 (red) and E_3 (black). The error bar represents $2\Delta t$.

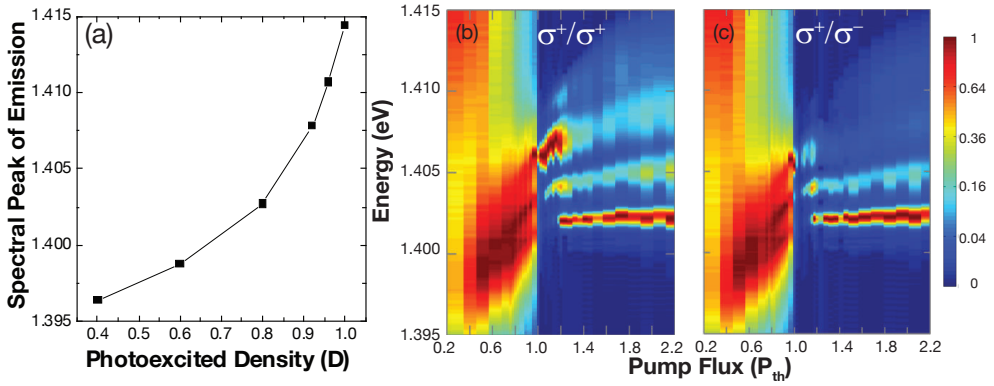

Figure 6.7 **Pump-flux-dependent resonance energy and polarized luminescence spectra.** (a) Resonance energy (the energy of emission mode at $k_{||} \approx 0$ in K-space spectral mapping) versus photoexcited density under a tightly-focused circular pumping beam (radius ~ 1 μm). The spectral peak can be considered as the effective cavity resonance and displays a sizable spectral blueshift with increasing the photoexcited density. Such an energy shift with photoexcited density is the basis of optically induced harmonic confinement (potential) using a spatially modulated pump beam profile. $D \approx 4 \times 10^{12}\,\mathrm{cm}^{-2}$ per quantum well per pulse. (b,c) Normalized spectra integrated over k-space as a function of pump flux in the double-hump-shaped pumping case: Co-circularly (b) and cross-circularly (c) polarized component. Quantized harmonic states are formed above $\sim 0.8P_{th}$. Below the threshold, the luminescence from all states is unpolarized. Above the threshold, the E_3 state is highly circularly polarized, where as the E_1 state has a diminishing circular polarization. The fourth quantized state (E_4) is weakly confined.

6.4 Theoretical model

Here I present a theoretical explanation of section 6.1 from a view of quasiparticle, and give simulation results of luminescence dynamics and time-integrated flux.

6.4.1 Optically induced potential and refractive index changes

The transverse optical modes confined by a spatially modulated refractive index can also be understood as an optically induced potential for a fictitious quasiparticle.

Considering the electromagnetic fields in a planar Fabry-Pérot cavity with a medium of a 2D spatially modulated effective refractive index profile $n(r)$, we can express the Helmholtz equation for the electric field in the following simplified form:

$$\frac{\partial^2 F(r,\varphi,z)}{\partial r^2} + n^2(r)\cdot k_0^2 \cdot F(r,\varphi,z) = 0 \tag{6.1}$$

The electric field F in the cavity can be decomposed into lateral and transverse components, and approximated as $F(r,\varphi,z) \propto \psi(r)\cdot\exp[-in(r)k_z(r)\cdot z)]$, where $k_0^2 = k_z^2(r) + k_{||}^2(r)$, and $k_{||}(r)$ and $k_z(r)$ are transverse and longitudinal wavenumbers in the vacuum, respectively. For simplicity, we consider the 1D case and reduce Eq. 6.1 to:

$$\frac{\partial^2 F(x,z)}{\partial x^2} + n^2(x)\cdot[k_0^2 - k_z^2(x)]\cdot F(x,z) = 0 \tag{6.2}$$

Applying the effective-mass approximation for small $k_{||}$, we express the in-plane dispersion $E_c(k_{||})$ in terms of an effective mass m^* for the excitation: $E_c(k_{||}) = E_{c0} + E_{||} = \frac{(n\hbar k_z)^2}{2m^*} + \frac{(n\hbar k_{||})^2}{2m^*}$, where $m^* \equiv \frac{\hbar^2 n^2 k_z^2}{2E_{c0}} = \frac{\hbar n^2 k_z}{2c}$.

Eq. 6.2 can then be mapped to a time-independent Schrödinger equation by replacing the electric field amplitude with the probability wavefunction ϕ of a hypothetical quasiparticle with an effective mass m^* in the presence of a potential $V(x)$, thus:

$$\frac{-\hbar^2}{2m^*}\cdot\frac{\partial^2\phi(x)}{\partial x^2} + [V(x) - E_c]\cdot\phi(x) = 0 \tag{6.3}$$

Replacing the effective mass for an optical cavity mode with longitudinal wavenumber k_z, we obtain

$$\frac{\partial^2\phi(x)}{\partial x^2} + \frac{n^2 k_z}{\hbar c} \cdot [E_c - V(x)] \cdot \phi(x) = 0 \tag{6.4}$$

Comparing Eqs. 6.2 and 6.4 gives

$$V(x) = \hbar c \cdot k_z(x) = E_{c0}(x) \tag{6.5}$$

Therefore, $E_{c0}(x)$ and $E_{\|}$ correspond to the potential $V(x)$ and the kinetic energy of a quasi-particle of mass m^*. Considering $E_{c0}(x) \propto \frac{\hbar c}{n(x)\,L_c}$, where L_c is the effective cavity length, we can relate the potential to the spatially modulated refractive index $\frac{\Delta n(x)}{\bar{n}}$ as follows: $V(x) = \overline{V} \cdot [1 + \frac{\Delta V(x)}{\overline{V}}] = \frac{\overline{E}_{c0}}{1+\Delta n(x)/\bar{n}} \approx \overline{E}_{c0}\,(1 - \frac{\Delta n(x)}{\bar{n}})$, where $\bar{n}$ and $\bar{V}$ are the refractive index and potential at $x = 0$. Thus, the spatial modulation of the potential ($\Delta V(x)$) and refractive index ($\Delta n(x)$) have a one-to-one correspondence: $\frac{\Delta V(x)}{\bar{V}} \approx -\frac{\Delta n(x)}{\bar{n}}$.

6.4.2 Phenomenological modeling

As discussed in section 6.4, the spatial modulation of the refractive index can be considered a spatially dependent effective potential for a quasiparticle with an effective mass associated with the bare cavity resonance and mean refractive index. The multiple transverse optical modes are equivalent to harmonic states in harmonic confinement (potential). We use a set of rate equations that consider a stimulated process and the spatial distribution of *e-h* carriers. We consider the temporal evolution of the reservoir distribution $N_R(x,t)$ and quantized sates $n_i(t)$. The *e-h* pairs photoexcited non-resonantly by a 2 ps pulse laser cool down rapidly (<5 ps) to the band edge. The cooled carriers in the reservoir $N_R(x,t)$ are subject to non-radiative loss (Γ_{nr}) and thus result in a slow decrease ($\sim$0.1 meV/ps) in the chemical potential μ. A fraction of the reservoir carriers [$N_{eh}(x,t) = \beta N_R(x,t)$] could couple effectively to the cavity light field when μ advances toward the cavity resonance E_c (Fig. 6.8), resulting in fictitious quasiparticles coined as correlated *e-h* pairs. The double-hump-shaped spatial distribution of *e-h* plasma results in the establishment of a harmonic chemical potential profile ($V(x) \propto x^2$) in which the standing waves of a macroscopic

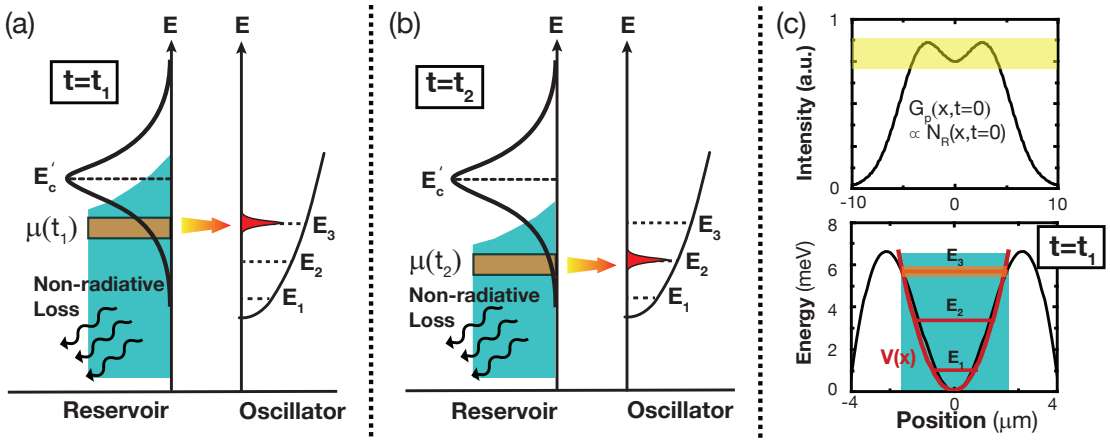

Figure 6.8 **Schematic diagrams for the theoretical framework.** (a–b) Energy level diagrams at delays t_1 and t_2 ($t_1 < t_2$) after injection of *e-h* carriers in the reservoir. The chemical potential $\mu(t)$ at a fixed location decreases with time largely because of the nonradiative loss. The formation efficiency of the correlated *e-h* pairs is approximated by a Lorentzian function centering at the cavity resonance E_c, whereas the conversion efficiency of correlated e-h pairs into quantized harmonic states is represented by a Gaussian function centering at quantized energies E_3, E_2, and E_1. (c) (top panel) The initial spatial distribution of *e-h* carriers in the reservoir ($N_R(x,t=0^+) \propto G_p(x,t=0^+)$). (bottom panel) The confining potential $V(x)$ (solid blue line), which is assumed to be stationary. The spatial μ at t_1 (solid black line) and t_2 (dashed black line). The correlated e-h pairs with μ close to the energies of E_i can scatter effectively into the E_i states.

coherent state are formed. However, only the correlated e-h pairs near in resonance with the quantized states of the harmonic potential can spontaneously be scattered into a specific E_i state at a rate W_s. Above threshold, the population of E_i states increases nonlinearly as a result of spin-dependent stimulation ($\propto W_{ss}\, N_{eh}\, n_i$). The consequent leakage photons from the decay of these confined correlated e-h pairs at a rate associated with the cavity photon decay rate Γ_c are then measured experimentally. The dynamics of the quantum oscillator of correlated e-h pairs can then be described by the following set of coupled rate equations:

$$\frac{dN_R(x,t)}{dt} = G_p(x,t)P - \Gamma_{nr}\, N_R(x,t) - \sum_{i=1}^{3} \eta_i\, \zeta\, N_{eh}(x,t)\,[W_{ss}\, n_i(t) + W_s]\,, \tag{6.6}$$

$$\frac{dn_i(t)}{dt} = \int dx\, \eta_i\, \zeta\, N_{eh}(x,t)\,[W_{ss}\, n_i(t) + W_s] - \Gamma_c\, n_i(t). \tag{6.7}$$

The spatial generation rate $G(x,t)$ follows the 2 ps Gaussian temporal and double-hump-shaped

Parameter		Parameter	
β	0.0125	W_s	1.0×10^{-4} ps^{-1}
Γ_{nr}	$1/700$ ps^{-1}	W_{ss}	1.0×10^{-2} ps^{-1}.
Γ_c	0.5 ps^{-1}	$\Delta\mu$	10 meV
E_1	1.401 eV	ΔE_1	1 meV
E_2	1.403 eV	ΔE_2	1 meV
E_3	1.405 eV	ΔE_3	1 meV
E_c	1.410 eV		

Table 6.1 **Fitting parameters**

beam profile (Fig. 6.8(c) and Fig.6.9(c)). P is the pump flux of helicity $\pm$. ζ is an energy dependent effective formation efficiency of the correlated e-h pairs. We approximate ζ as a Lorentzian function $\zeta = 1/[1+(\mu - E_c)^2/\Delta\mu^2]$, where $\Delta\mu$ is the energy range that correlated e-h pairs are formed. $\eta_i = \exp\left[-(\mu - E_i)^2/(2\,\Delta E_i^2)\right]$ is the coupling efficiency of the correlated e-h pairs to the E_i state, where ΔE_i is the spectral linewidth of the E_i state.

The fitting parameters are listed in the table. 6.1. In this simulation, we neglect the spin degree of freedom and only consider the density regime above 0.8 N_R^{th} and $|\mu(x,t) - E_c| < 15$ meV ($N_R^{th} \sim 500$, corresponding to the occupation number at $P = P_{th}$). We approximate $\mu(x,t) = \mu_0 + g\,N_{eh}(x,t)$, where μ_0 and g are determined by the following initial conditions: $\mu(x=0,t=0)$ = 1.4 eV and $\mu(x=\pm3\mu m,t=0)$ = 1.407 eV.

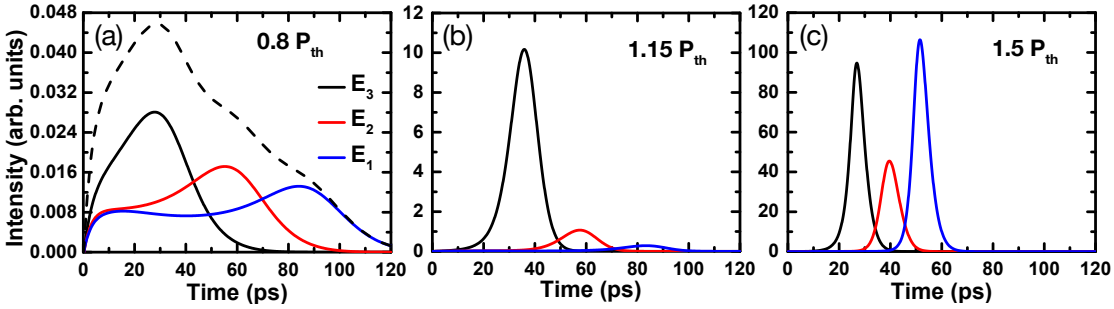

Figure 6.9 **Simulated dynamics of the harmonic states.** (a) The time-dependent occupation number of harmonic states E_3 (solid black line), E_2 (solid red line), E_1 (solid blue line), and the sum of the three states (dashed black line) for P = 0.8 P_{th}. (b–c) Similar to (a), but for P = 1.15 and 1.5 P_{th}. For simplicity, the spin degree of freedom is neglected in these calculations. Additionally, the radiative decay rates of these states are assumed to be identical and equal to Γ_c, resulting in an identical pulse duration.

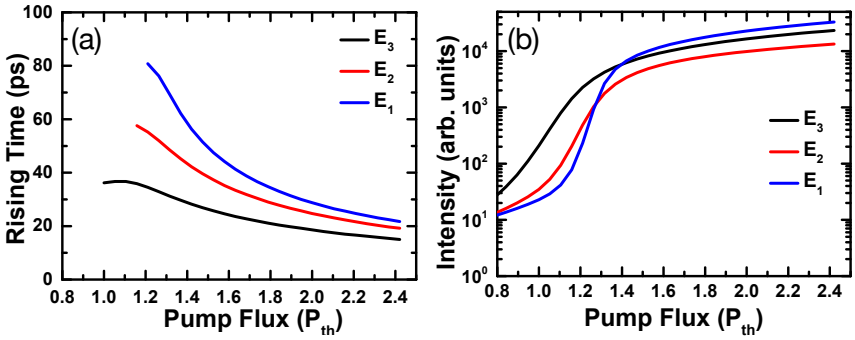

Figure 6.10 **Simulated rise times and time-integrated flux of the harmonic states.** The calculated rise times (a) and time-integrated flux (b) of the E_3 (solid black line), E_2 (solid red line), and E_1 (solid blue line) states as a function of pump flux.

This model reproduces the time evolution of the quantized states with increasing photoexcited density (Fig. 6.9). Below the threshold, the scattering of the correlated e-h pairs into the quantized states occurs through a spontaneous decay process. The radiative quantum efficiency is low ($< 10^{-4}$) because of the dominant non-radiative recombination loss. Above the threshold, the quantum efficiency increases by two to three orders of magnitude as a result of stimulation. This model reproduces qualitatively the rise times and the time-integrated emission fluxes of the multiple pulse lasing from the quantized states when the pump flux is varied (Fig. 6.10).

6.5 Conclusion and discussion

In conclusion, I report the observation of macroscopic harmonic states in an optically induced confinement in a highly photoexcited semiconductor microcavity at room temperature. The spatially photo-modulated refractive index changes result in the visualization of harmonic states in a micrometer-scale optical potential. The quantized energies of the harmonic states can be up to 4 meV, even in the weak-coupling plasma limit. I characterize the time evolution of the harmonic states directly from the consequent pulse radiation and identify sequential multiple $\sim$10 ps pulse lasing with different emitting angles and frequencies.

Our group develops the rate-equation model to describe the dynamic formation of quantized states in an optically defined harmonic confinement (Sec. 6.4). This phenomenological model

reproduces qualitatively the dynamics and integrated emission flux of the harmonic states when photoexcited density is varied (Figs. 6.8, 6.9, and 6.10). Non-equilibrium polariton condensates have been modeled by a modified Gross–Pitaevskii (GP) (or complex Ginzburg–Landau [cGL]) equation that accounts for the finite lifetime of polaritons [121, 104]. However, cGL-type equations are inapplicable for the multiple dynamic states examined in this study. Additionally, the formation of a BEC-like condensate that underpins the GP- or cGL-type equation is not necessarily justified in room-temperature experiments.

Transverse light-field patterns and confined optical modes have been identified in nonlinear optical systems [122], VCSELs [123, 124], and microscale photonic structures [125]. In principle, the multiple transverse mode lasing in a high-density EHP described in the present study can be modeled by a self-consistent numerical analysis with Maxwell-Bloch equations developed for conventional semiconductor lasers [126, 127]. This approach is valid provided that the strong optical nonlinearities induced by Coulomb many-body effects, such as screening, bandgap renormalization, and phase-space filling, are all considered. For example, one can consider the formation of index-guided multiple transverse modes as a result of an optically-induced refractive index reduction ($\Delta n_c(x)$). The cavity resonance shift (δE) can be estimated from $\delta E_c/E_c = -\Delta n_c/n_c$, where n_c is the effective refractive index averaged over the longitudinal cavity photon mode which spans over $\sim \mu$m in the growth direction. Therefore, $\delta E \sim$10 meV (Figs. 6.1 and 6.2) corresponds to $|\Delta n_c/n_c| \sim 1\%$. Such a significant refractive index is probably with resonance-enhance optical nonlinearity from the *e-h* correlation [12, 128, 129, 102] or carrier-induced change in refractive index at a high carrier density (of $\sim 10^{19}$ cm^{-3} or more) [130, 90, 131]. Further characterizing the photoexcited density distribution is necessary to uncover the microscopic formation mechanisms, and the mechanisms include a sizable spatial modulation in refractive index or equivalent effective harmonic confinement under pulse excitation. This can be implemented with the use of other ultrafast spectroscopic techniques, such as a pump-probe spectroscopy, is necessary.

CHAPTER 7

OPTICALLY INDUCED RESONANCES IN A SEMICONDUCTOR MICROCAVITY

So far I have demonstrated spin-polarized lasing in a highly photoexcited semiconductor microcavity, and the large energy shift with increasing pump flux is attributed to the combination effect of both E_c shift and electron-hole interaction. The E_c shift can be equivalent to refractive index change with simple formula $\left|\frac{\delta E_c}{E_c}\right| = \left|\frac{\delta n_c}{n_c}\right|$. The essential question is whether coherent state exists under such e-h-γ system. On the other hand, theoretical work on QWs system predicted that a quasiparticle gap forms at the conduction-electron and valence-hole Fermi surface in an interacting system [12, 13], which can be reflected on the absorption spectrum. To explore the existence of coherent state as well as the quasiparticle gap in our system, that motivate us to perform the optically time-resolved pump-probe reflectance spectroscopy measurement.

The principle of pump-probe technique here is in the following. The strong pumping pulse generates high-density photoexcited carriers in the sample. The presence of carriers may modify the optical properties of a sample, which can be revealed on the transmission or reflection by shining a weak light (probe) on the sample. By monitoring the probe signal as a function of time delay between pump and probe, it is possible to characterize the time-dependent optical change due to the pump. In the experiment, the measurement reveals a transient optically induced resonance near the cavity resonance (E_c) after non-resonant pumping with a few picosecond pulsed excitation. Such resonance red shifts in energy and decays slowly with a long time constant. I will detail the characteristics of the resonance in the following section.

The experimental setup is mentioned in section 3.2.5 with figure shown in Fig. 3.7. Fig. 7.1 demonstrates the optical pumping scheme in the pump-probe measurement. The pump is chosen as 2-ps laser pulse with peak energy 0.2 eV above E_c. The probe is a 20-fs laser pulse with broadband energy covering from 1.39 to 1.55 eV. The repetition rates of pump and probe laser pulses are synchronized through a piezo-driven end mirror in the light path inside the probe laser

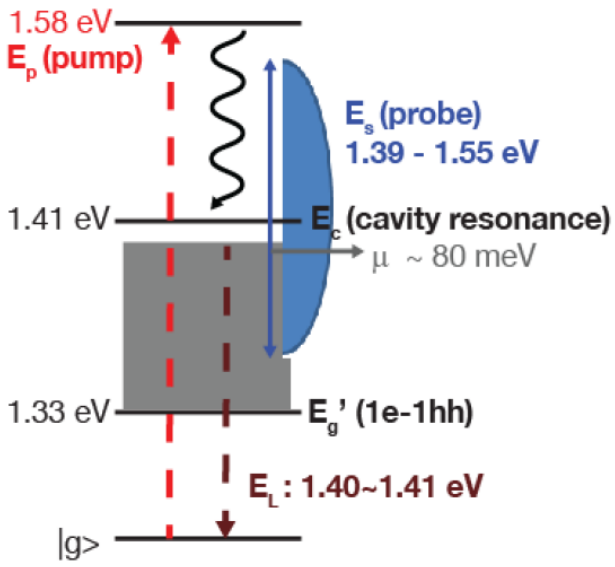

Figure 7.1 **Pumping scheme of pump-probe measurement.** In the experiment, the microcavity sample is non-resonantly pump by 2-ps laser pulse and is probed by a 20-fs broadband laser pulse. The pump energy is about 0.2 eV above cavity resonance $E_c \sim 1.41eV$. The energy band of probe laser covers from 1.39 to 1.55 eV. The gray area represents the accumulation of e-h carriers with the top edge as chemical potential μ.

system. However, the arrival time of two laser pulses at sample surface is controlled by tuning the light path of probe laser. The time difference of these two arrival time is defined as time delay $\Delta t = t_r - t_p$, which t_r and t_p are the time of probe and pump pulse arriving at sample surface, respectively. The pump and probe laser beams are linearly or elliptically polarized, and their polarizations are always orthogonal to each other. The pump flux is $\sim 3 \times 10^9$ photons per pulse, while the probe flux is adjusted to about two-thousandth of the pump. The pump beam passes through a holographic phase-only 2D spatial light modulator (SLM), and is focused on the sample with a flat-top shape of 10×10 μm^2 or a focused spot of 2 μm diameter. The probe beam is always focused to a spot of 2 μm diameter without passing through the SLM. In the experiment, the luminescence and reflecting probe laser were measured in real space or momentum space by a Fourier-transform optical setup equipped with an imaging spectrometer and ps streak camera system. The time resolution is limited by the 2 ps of pump laser (Ti: sapphire laser).

7.1 Resonance in microcavity

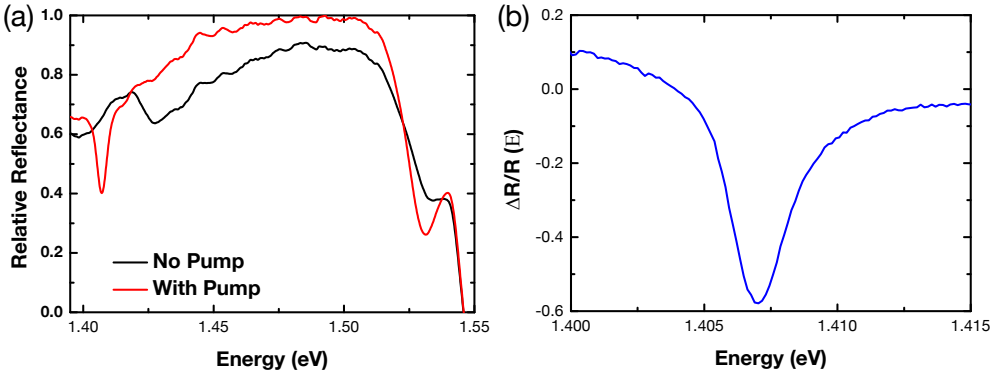

Figure 7.2 **Differential reflectance.** (a) Reflectance spectra with no pump (black) and with pump (red), denote them as R and R' respectively. (b) Calculated differential reflectance $\Delta R/R = (R' - R)/R$, which indicate a presence of large resonance under high electron-hole plasma density.

First, I will discuss the reflectance change of microcavity sample under non-resonantly optical pumping. Fig. 7.2 (a) shows the reflectance of microcavity in the absence of pumping (black line, $R(E)$) and in the presence of pumping (red line, $R'(E)$) at $\Delta t \sim 5ps$. The pumping flux here is about 0.85 P_{th}, which P_{th} corresponds to photoexcited density $\sim 1 \times 10^{19}\, cm^{-3}$. The reflectivity of stop band is significant enhanced under pumping, and a large dip appears at E_c. These results demonstrate the Q-factor of microcavity becomes better with a large density of photoexcited carriers. The differential reflectance change defined as $\Delta R/R = [R'(E) - R(E)]/R(E)$ can exceed 50 % shown in Fig. 7.2 (b). For convenience, the $\Delta R/R$ is called as resonance in the following sections. The large $|\Delta R/R|$ and enhancement of Q-factor are attributed to the combination effect of decreasing light absorption in DBR layers and e-h correlation. The reduction of light absorption in DBR increases the transparency near the E_c and the reflectivity in stop band, which is proven by simulation introduced in laser section. The e-h correlation effect is not obvious, which needs more experimental results to be illustrated.

The resonance shape is asymmetric in Fig. 7.2 (c), and is quite different to the symmetric Lorentzian shape in most conventional laser systems. Such asymmetric shape can be fitted well

by a Drude model with a Fano-shaped Lorentz oscillator, this simulation will be demonstrated in the later section. The Fano-resonance typically occurs in an interacting system resulting from the light interference between a background and a resonant scattering process. This result indirectly implies the photoexcited carriers generated in the microcavity sample is not purely free electrons and holes.

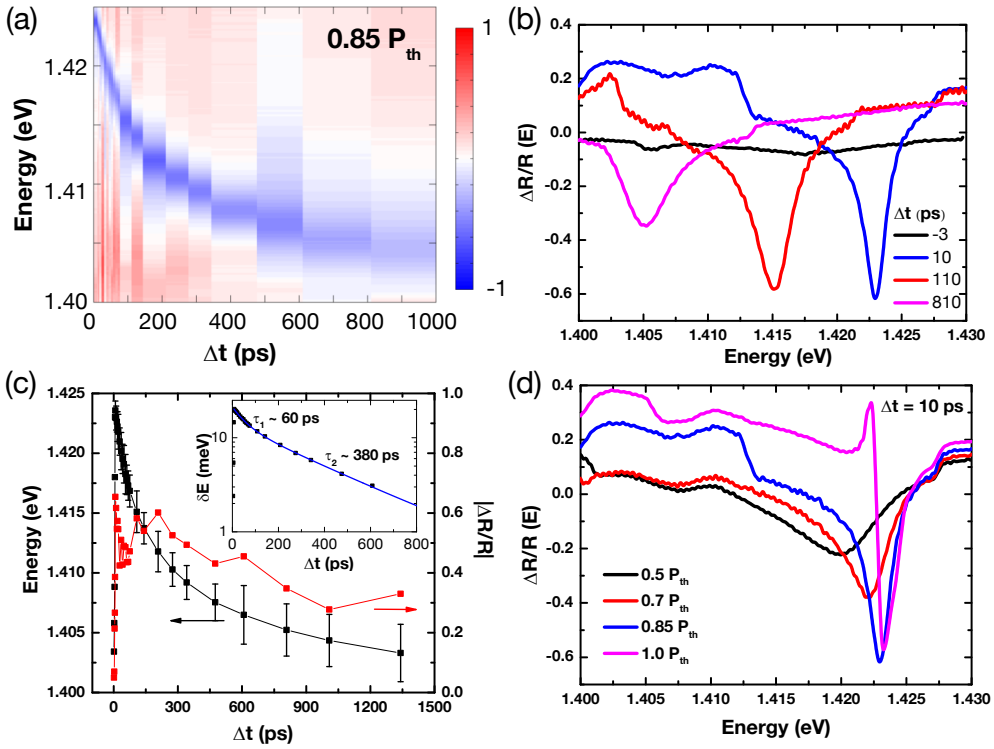

Figure 7.3 **Dynamic of the resonance.** (a) 2D image of differential reflectance spectra with delay time dependence at pumping $P = 0.85\,P_{th}$. Each slice represents to normalized spectrum at particular delay time $\Delta t = t_r - t_p$, which t_r and t_p are the time of probe and pump pulse arriving at sample surface, respectively. The pump here is a focused spot of 2 μm. (b) Selected differential reflectance at pumping 0.85 P_{th}. The resonance exists in a long time about 1 ns. (c) The energy peak (black) and depth (ref) of resonance as a function of Δt. The long-lived resonance red-shifts in energy in about 20 meV. The inset is energy shifting δE (the difference between energy peak and bottom energy) as a function of Δt in log scale. It illustrates two-step decay process with fast relaxation time $\tau_1 \sim 60$ ps and slow relaxation time $\tau_2 \sim 380$ ps.(d) Differential reflectance with selected pump flux. The resonance blue shifts in energy accompanied with depth increment as pump flux increases.

Next, I discuss the dynamics of transient optically induced resonance, it is long-lived and can have a significant spectral shift with time. To investigate how the resonance evolves with relaxing

carriers in energy, here the beam profile of the pump is chosen as a tightly focused spot. Fig. 7.3 (a) illustrates the 2D image of resonance as a function of Δt and energy at pump power 0.85 P_{th}. The optically induced resonance can last more than 500 ps. Fig. 7.3 (b) shows differential reflectance spectra at selective Δt. As Δt increases, the resonance red-shifts 20 meV in energy accompanied with broadening linewidth of depth. Fig. 7.3 (c) tracks the energy peak of resonance (black) and the magnitude of depth (red) with Δt dependence. The resonance appears within 5 ps after pumping and then decays with fast and slow processes. The decay time constant of these two processes shown in the inset of Fig. 7.3 (c) are 60 ps and 380 ps, respectively. On the other hand, the magnitude of differential reflectance can maintain 0.4 even at $\Delta t > 500ps$. Fig. 7.3 (d) represents density-dependent resonance at $\Delta t \approx 0^+$ and selective pump flux near and below threshold. The energy peak of resonance blue shifts in about 3 meV when pump flux increases from 0.5 to 1 P_{th}, and the linewidth of depth narrows gradually.

The energy peak of the resonance varies with different probing angles, and such angle-resolved resonance appears to be a parabolic curve. This curve resembles the angle-resolved spectrum of luminescence from the microcavity sample. Fig. 7.4 demonstrates the angular dispersion of the resonance under pump power 0.9 P_{th} at $\Delta t = 10$ ps (black) and 680 ps (red). The error bars represent the FWHM of the depth. The black and red dashed lines are fitting parabolic curves for angle-resolved resonance energy peak, while the blue line represents the fitting curve of luminescence spectral peak at different angles shown in the inset. The consistency of the black dashed line and the blue line indicates the luminescence spectrum matches to the resonance at 10–50 ps after the excitation.

7.2 Polarization-dependent resonance in microcavity

Under circularly polarized pumping, the differential reflectance change by probing with orthogonal circularly polarized components are different, indicating our microcavity under high photoexcitation is chiral characteristics. Fig. 7.5 (a) shows the differential reflectance change below lasing

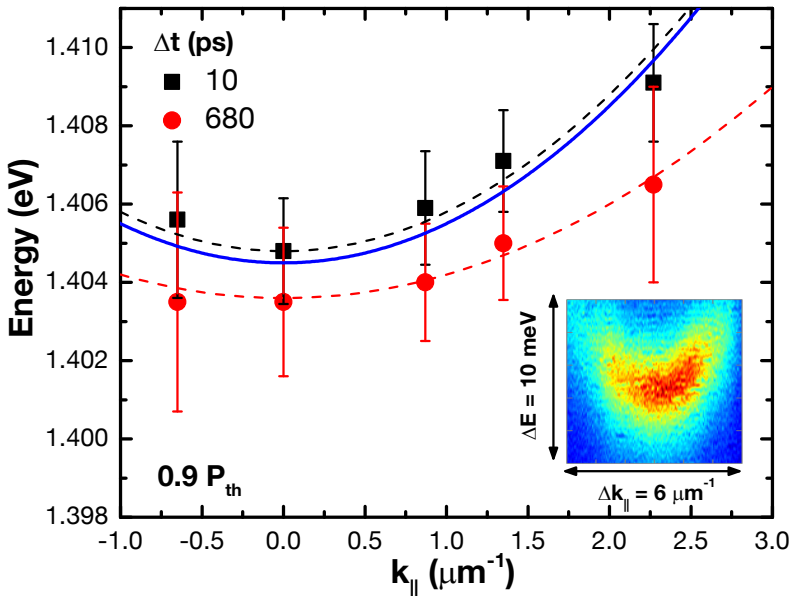

Figure 7.4 **Angular dispersion of the resonance.** Angle-resolved resonances (the peak of the differential reflectance spectrum) at Δt = 10 ps (black) and $\sim$ 700 ps (red) under pumping P = 0.9 P_{th}. The error bar represent the full width half maximum (FWHM) of the differential reflectance. Dashed lines are simulated parabolic curves, while blue line is fitting parabolic curve of angular dispersion spectrum (inset figure) of photoluminescence at 0.9 P_{th}.

threshold (0.9 P_{th}) at $\Delta t = 0$ under circularly polarized σ^+ and linearly polarized σ^x pumping. A energy peak difference about 0.8 meV appears between σ^+/σ^+ (red) and σ^+/σ^- (blue) components of transient induced resonance. Fig. 7.5 (b) traces down the energy peak of resonance for different components. The transient spin-dependent splitting decreases from 0.8 meV to zero with decay time in about 50 ps. The splitting of transient resonance reveals that the optical responses of microcavity for two orthogonal circularly polarized light are different. Under circularly polarized pumping, it creates an unbalanced population of spin-up and spin-down carriers in reservoir within 0-50 ps. When the microcavity is probed by circularly polarized light, the σ^+ can only respond to spin-up carriers. Therefore, the unequal spin-polarized carriers results in energy splitting in pump-probe reflecting spectroscopy, and such splitting decreases due to the reducing population difference of spin-polarized carriers. The delay time is related to spin relaxation time of photoexcited carriers, and is larger than lasing lifetime $\sim 10ps$. The unbalanced spin carriers is the

essential requirement to initiate spin-dependent stimulation and the spin-polarized lasing presented in Chapter 4.

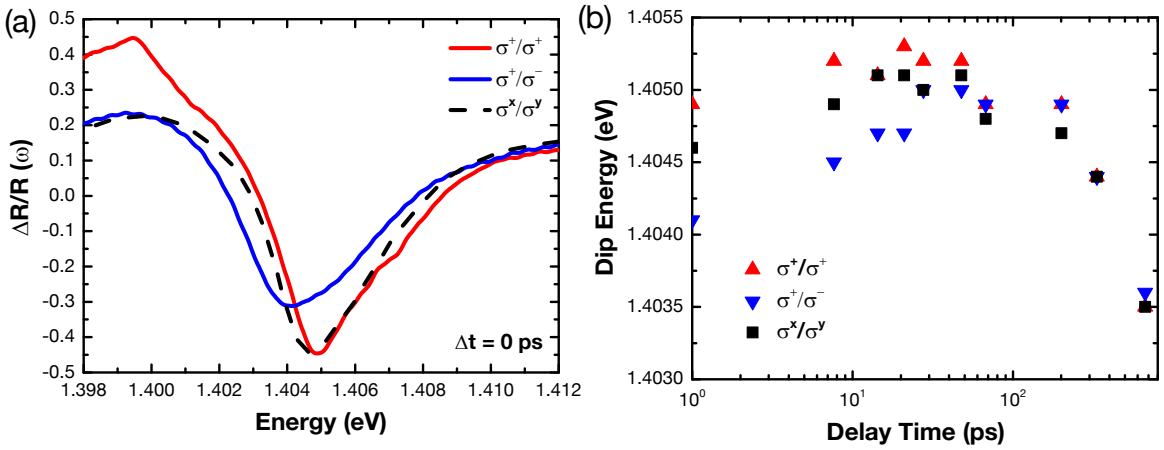

Figure 7.5 **Polarization-dependent resonance.**(a) Differential reflectance spectra under circularly polarized $/sigma^{+}$ pumping and linearly polarized σ^{x} pumping. The co-circular σ^{+}/σ^{+} (polarization of pump/probe) and cross-circular σ^{+}/σ^{-} components are represents as red and blue dots, respectively. The cross-linear component is shown as black dots. (b) Energy peaks of the differential reflectance spectra in (a) with a flattop shape of $10 \times 10\,\mu m^{2}$. The difference ΔE of energy peaks of orthogonal circular components appears at $\Delta t = 0$, and diminishes to zero with decay time approximated about 25 ps.

7.3 Simulation Result

The large $|\Delta R/R|$ can be seen as the effect of carrier-induced refractive index change in photoexcited microcavity. In the following paragraphs, I will present a few methods to simulate reflectance spectrum and explore the effect of relaxing carriers in the whole system. The discussion about potential existence of the existing correlated e-h pairs will be mentioned later.

7.3.1 Drude-Lorentz model

Before presenting the theoretical methods, I would like to outline the connection between the reflectance and the dielectric constant ε. The former one is a common measurement in optics, and the latter is one of important properties in materials. The dielectric constant ε affects the Coulomb

forces between two point charges in materials, so it can modify the optical properties of materials if ε changes. The refractive index n is typically used to represent the optical parameter of materials, and relates to the dielectric constant by $n = \sqrt{\varepsilon}$. The refractive index is normally a frequency dependence denoted as $n(\omega)$, where ω is the light frequency. The microcavity sample with the structure of multiple layered materials can be regarded as a whole sample with effective refractive index of sample $n(\omega)$. The reflectance can be deduced by: $R(\omega) = \left|\frac{n(\omega)-1}{n(\omega)+1}\right|^2$ according to Fresnel equation. If the dielectric constant is real number, then it can be experimentally determined by measuring $R(\omega)$. However, the dielectric constant is typically a complex number in math and can not be deduced by reflectance spectrum only.

Although $\varepsilon(\omega)$ can not be obtained precisely from the reflectance spectrum, we could apply few simple models to study the system properties under intense optical pumping. The first model we use is Drude-Lorentz (DL) model. It describes that the optical response of charge carriers in materials is represented as a set of harmonic (damped) oscillators, and the $\varepsilon(\omega)$ will be:

$$\varepsilon(\omega) = \varepsilon(\infty) + \sum_i \frac{\omega_{pi}^2}{\omega_{oi}^2 - \omega^2 - i\gamma_i\omega} \tag{7.1}$$

Here $\varepsilon(\infty)$ is defined as "high-frequency dielectric constant", which represents the contribution of all oscillators at very high frequencies (compared to the frequency range in consideration). The parameters ω_{pi}, ω_{oi}, and γ_i are the "plasma" frequency, the transverse frequency (eigenfrequency) and the linewidth (scattering rate), respectively of i-th Lorentz oscillators. The "Drude" in model's name describes the response of free (unbound) charge carriers, and the ω_{oi} is zero in this case. In the DL model, the Lorentz oscillators are independent, and the reflectance spectrum normally can be represented by the sum of independent Lorentz oscillators. Fig. 7.6 (a) give an example showing a reflectance spectrum (black dots) obtained in our experiment without pumping. The simulation curve based on DL model is shown as red line.

The DL model describes a material system with free carriers; however, the DL model can not fit well with the reflectance under pumping. This result indicates that the oscillators described by classical optics in the model are interacting instead of being independent. One could also

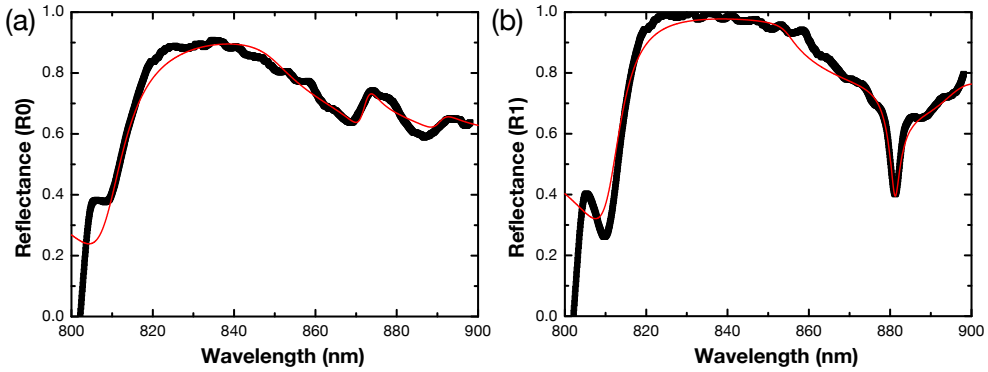

Figure 7.6 **Simulation of reflectance.** reflectance spectra without and with presence of pumping in (a) and (b), respectively. The black dots represent measured reflectance, and red lines are simulation. The simulation method used in (a) is classical Drude-Lorentz (DL) model, while in (b) a Fano-shaped oscillator is added in DL model.

witness the difference from the resonance shape. The resonance in the DL model is typically symmetric resembling the Lorentz shape, but the one in our measurement (Fig. 7.2) is asymmetric. The asymmetric shape of resonance is similar to the Fano-resonance reported in other interacting systems. Therefore, we modified DL model by swapping one of the Lorentz oscillators with a Fano-shaped Lorentz oscillator, which the form of dielectric constant is:

$$\varepsilon = \frac{\omega_p^2}{\omega_o^2 - \omega^2 - i\gamma\omega}\left(1 + i\frac{\omega_p}{\omega}\right)^2 + \left(\frac{\omega_p\omega_q}{\omega_o\omega}\right)^2 \tag{7.2}$$

Here ω_q is an inserted parameter that gives asymmetric shape. If $\omega_q = 0$, the above equation recovers to the aforementioned DL form. The ω_q relates to q-factor in Fano-resonance theory by: $q = \omega_o/\omega_q$. If the ω_q (or smaller q) is larger, then a severe asymmetric resonance shape is obtained. The simulation result of DL model with Fano-resonance is shown in Fig. 7.6 (b).

After optical pumping, the population distribution of photoexcited carriers varies in time and energy, thus we will explore these carriers' dynamics including non-radiative carriers through studying the time-dependent dielectric constant. Fig. 7.7 demonstrates the reflectance (black dots) with pumping in delay time Δt at (a) 0 ps and (b) 670 ps. The simulated curve shown in red line is based on DL model with additional Fano-shaped Lorentz resonance. Fig 7.7 (c) represents dielectric constant in real part ε_r (black) and imaginary part ε_i (red), with the solid and short dashed

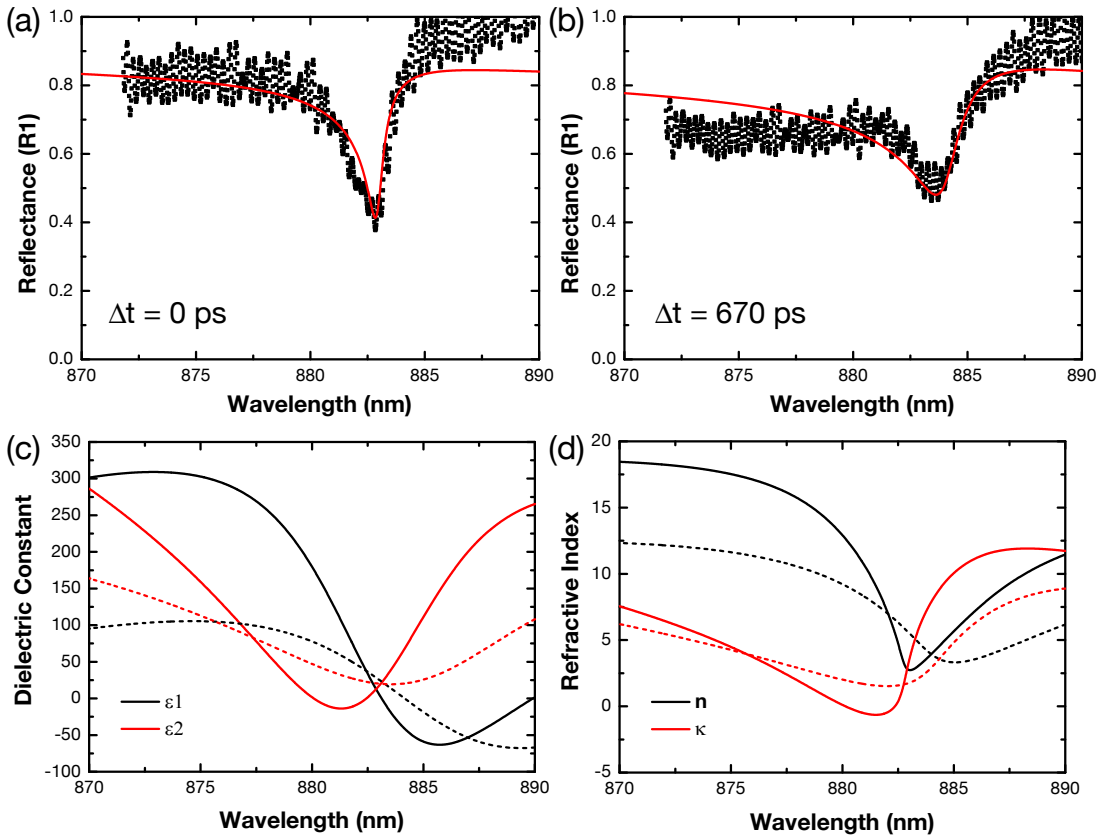

Figure 7.7 **Time dependent dielectric constant.** Reflectance under pumping (black dots) with simulation (red line) based on DL model with additional Fano-resonance shown at (a) $\Delta t = 0$ and (b) $\Delta t = 670ps$. (c) spectral resolved dielectric constant in real part (ε_1, black line) and imaginary part (ε_2, red line). The solid and short dashed line represent the case at Δt = 0 and 670 ps, respectively. (d) spectral resolved refractive index with same definition as (c).

line symbols the case at $\Delta t = 0$ and $\Delta t = 670ps$. Fig 7.7 (d) illustrates the case of refractive index and the extinction factor κ. The κ associates with absorption α by formula $\alpha = \frac{2\omega}{c} \times \kappa$, where ω is the light frequency. Near Δt = 0, the ε_i shows concave shape near resonance accompanied with smaller α. The depth of ε_i is closed but not the same to the peak of resonance, while the transition of ε_r (from positive to negative) as well as the minimum of n is same as the resonance peak. As time increases, the overall shape of dielectric constant red shifts in energy with attenuated amplitude. The concave shape of κ implies that the decreasing absorption near cavity resonance allows probe laser light penetrated into sample instead of bouncing back, so the reflectivity drops near the cavity.

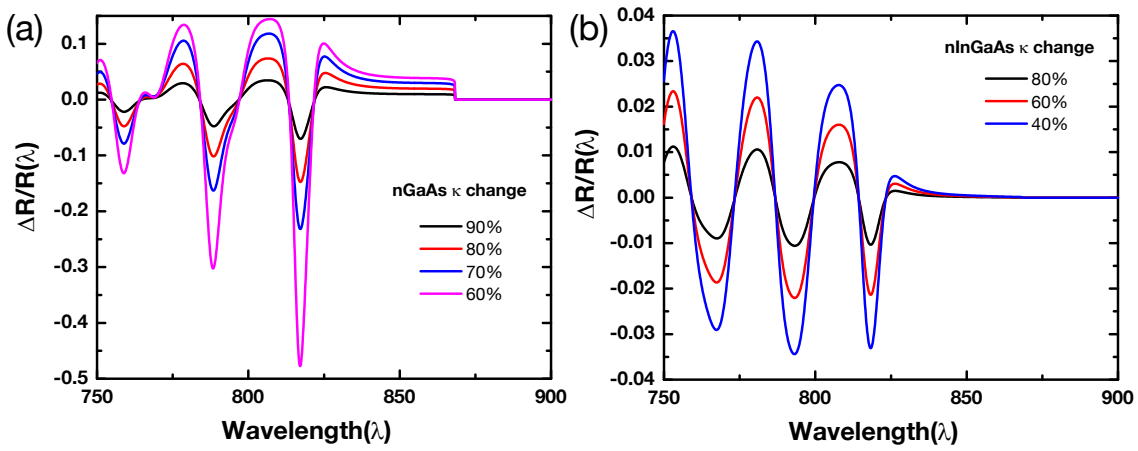

Figure 7.8 **Reflectance change from absorption effect.** Differential reflectance change resulting from different decreasing imaginary part of refractive index of (a) GaAs and (b) InGaAs.

7.3.2 Transfer-matrix method

The second way to simulate reflectance is the transfer-matrix method, and it gives some insight about carriers impact on the system, too. The transfer-matrix method is based on Maxwell equation plus the continuous condition for the electric field as the electromagnetic field across boundaries from one medium to another. If the field is known, the stack of layers can be represented as a system matrix. One example of simulation by this method is already shown in Fig. 3.2, I also discussed the resonance shift with the refractive index change induced by band filling effect of carriers in Sec. 4.5. Now I consider if the absorption of the system is modified by a large density of carriers, how the system behaves on its reflectance spectrum. The optical absorption of the system associates to the imaginary part of the effective refractive index.

The reduced imaginary part of the refractive index in the system could enhance the contrast of local minimum and maximum of reflectivity. Our microcavity sample consists of three layer materials: GaAs, AlAs and $In_{0.15}Ga_{0.85}As$ (abbreviated as InGaAs for convenience). I will not consider the absorption effect from AlAs since the band gap of AlAs is 2.12 eV, which is far above the pumping energy. The imaginary part of the refractive index n_i of one material is zero if light energy is below material's band gap (no absorption). Fig. 7.8 illustrates differential reflectance

change from different reduced degree of absorption part of (a) GaAs layers and (b) InGaAs layers. GaAs and InGaAs are also the main constituent materials of DBR and MQW, respectively. In an energy range above the band gap of semiconductors (GaAs or InGaAs), the reducing n_i can result in larger local maximum and smaller local minimum of reflectivity. Comparing the effect from between GaAs and InGaAs, the GaAs part gives more significant influence because the thickness of GaAs is much larger than that of InGaAs. In the experimental result (Fig. 7.2 (c)), the 50% magnitude of $\Delta R/R$ requires the change of imaginary refractive index up to 40% in GaAs or 60% in InGaAs. This deduction arises two unanswered questions: (1) Can a large-density free EHP results in 40% change in absorption of GaAs? So far I haven't found any work reported about large change of absorption in semiconductors due to high-density EHP. (2) How to explain an inconsistence of reflectance change between the experimental result and simulation. To be specific, the resonance in the experiment appear at energy below the GaAs band gap; however, the reflectance change near 880 nm is very small in our simulation model. The simulation model with transfer matrix method is based on the classical optics in the system of free carriers. Therefore, the inconsistence indirectly implies that an interaction beyond classical physics exists in our system.

7.4 The origin of optically induced resonance

From previous section, a large density of free carrier can cause carrier-induced refractive index change, but it can not explain all the result of the large magnitude of $\Delta R/R$. The optically induced resonance is attributed to the combination effect of carrier-induced refractive index change in DBR layers and the enhancement of optical nonlinearity due to e-h correlation in MQW. In this section, I will present two control experiments to explore how much contribution of such effect comes from pure cavity or DBR layers.

The first control experiment is the measurement of $\Delta R/R$ from a commercial VCSEL, which is thought no e-h correlation playing in role and is typically no absorption in DBR layers. The magnitude of $\Delta R/R$ is less than 5%, which is smaller than our simulation. It demonstrates again

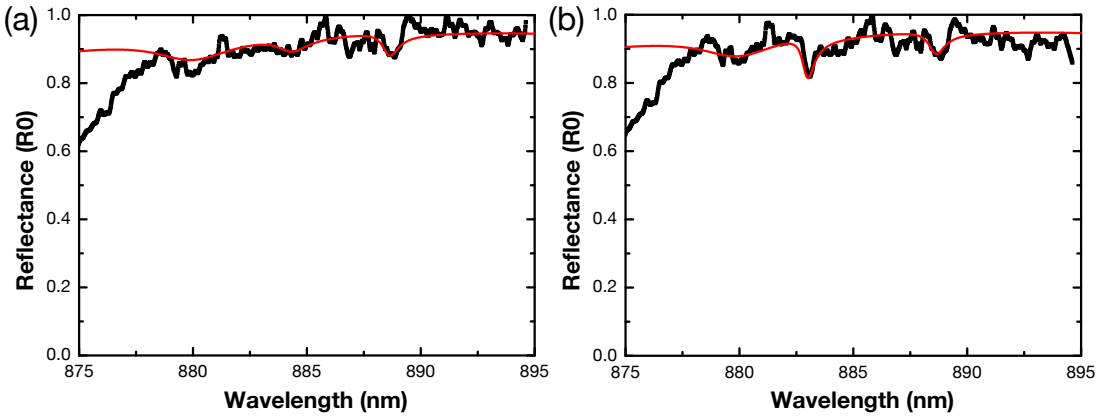

Figure 7.9 **Carrier effect on blank cavity.** Reflectance spectra (black dots) and simulation (red) under (a) no pumping and (b) pumping, respectively. The simulation is based on DL model.

that the absorption in DBR layers indeed changes the optical properties of microcavity sample.

The second control experiment is the measurement of $\Delta R/R$ from a microcavity sample with quantum dots (QDs). This sample is obtained from our collaborators, Lin's group, and it contains 19 top DBR layers and 24 bottom DBR layers with the same composite structure with microcavity sample presented before. The bare E_c is shifted to around $\sim 885\,nm$. The sample has much smaller active region (the total volume of QDs) compared to previous microcavity sample with MQW; therefore, the e-h correlation is suppressed. For convenience, I call the microcavity sample with QDs as blank cavity. Fig. 7.9 demonstrates the reflectance of blank cavity under a condition of (a) the absence of pumping and (b) the presence of pumping. Under the optical pumping (flat-top beam profile), a small dip appears at $\sim 883\,nm$, which is blue shift compared to bare cavity resonance. The red lines are the simulation based on DL model, which fits well with these two spectra. This implies the blank cavity can be described by the sum of independent Lorentz oscillators no matter if the system is optically pumped or not.

The optical response of the microcavity with MQW and blank cavity are quite different, and their comparison is shown in Fig. 7.10. The left panels show $\Delta R/R$ measured in our sample, and the right panels show $\Delta R/R$ measured in the blank cavity. The top and bottom panels are using flat-top and tightly focused spot beam profile of pumping, respectively. Under the same order

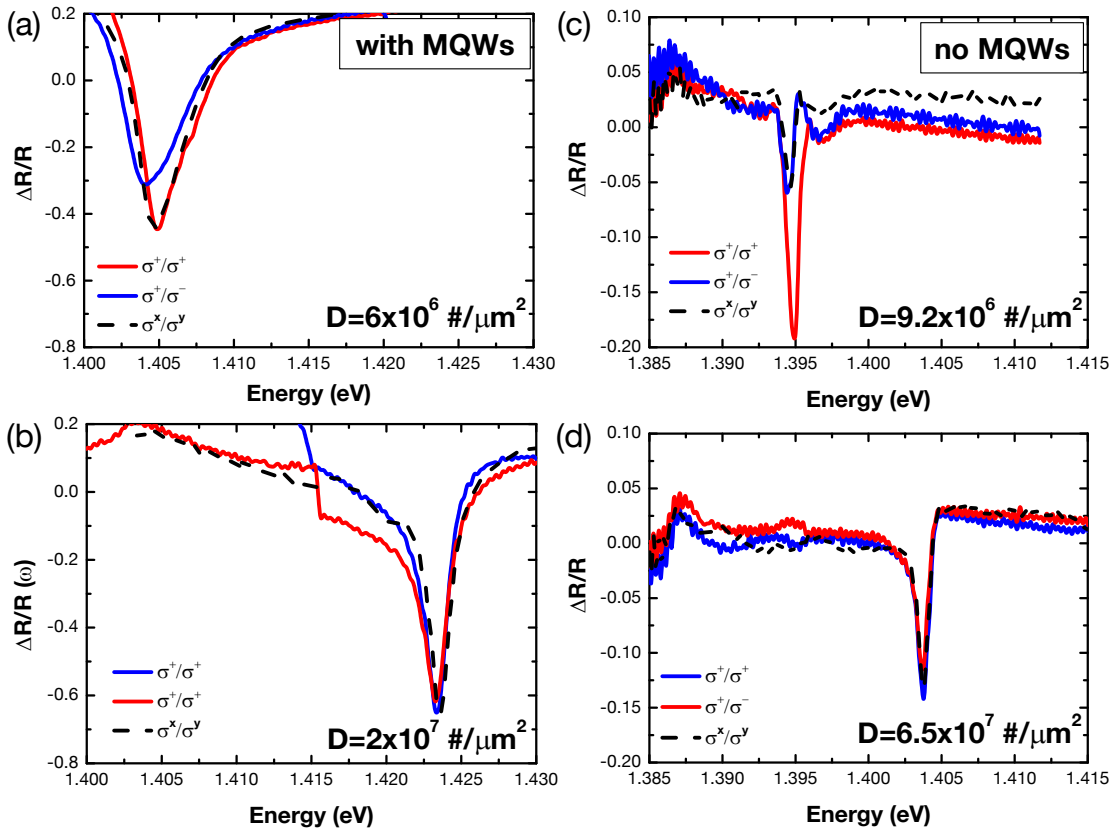

Figure 7.10 **Comparison of blank cavity with and without MQWs.** (a–b) Differential reflectance spectra of the microcavity with MQWs under flattop or focused excitation. (c–d) Same conditions as (a–b) but the samples are the microcavity without MQWs in the active region.

photoexcited density, the energy shift in the blank cavity is 10 meV, which is much shorter than that in our sample. Moreover, the linewidth of resonance in the sample is broader than that in the blank cavity. It gives an evidence that the light-induced e-h correlation in MQW modifies the optical properties significantly near E_c, and the e-h correlation makes more than 50% contributions on $|\Delta R/R|$.

7.5 Conclusion and Discussion

In conclusion, a transient optically-induced resonance appears near E_c within 5 ps after 2 ps pulse pump excitation with nearly 0.2 eV excess energy above E_c and then decays slowly with more than 500 ps delay time constant. The differential reflectance change $\Delta R/R$ measured in two-color

pump-probe reflectance spectroscopy can exceed 50 %, which is three to four orders of magnitude higher than typical photoexcited reflectance measurement in the GaAs-based quantum well or semiconductor microcavity. The optically induced resonance is attributed to the combination effect of carrier-induced refractive index change in DBR and e-h interaction in MQW. The energy peak of such resonance can shift in 5 meV under tightly focused pumping with two decay rates. On the other hand, the resonance has energy splitting under circularly polarized pumping with flat-top beam profile, indicating our microcavity is chiral characteristics.

Any reflectance spectrum change associates with effective refractive index change in a system, but such carrier-induced index change can not be totally attributed to optical constant change due to free carriers. I first simulate the pump-probe reflectance by DL model with an additional Fano-shaped Lorentz oscillator. The well-fitting of asymmetric shape of the resonance indirectly implies our microcavity is an interacting system under optical pumping. Next, the simulation with transfer-matrix method demonstrates that 50% $\Delta R/R$ needs 40% change in absorption of GaAs, which seems unlikely in a free EHP system. Last, I present comparison of $\Delta R/R$ measurement between microcavity with MQW and blank cavity, which both the energy shift with photoexcited density as well as the magnitude of $\Delta R/R$ in our microcavity are larger than the other case. It reveals that the light-induced e-h correlation can significantly modify the optical response near E_c with the contribution of the magnitude of $\Delta R/R$ exceeding 50%.

CHAPTER 8

DISCUSSION AND FUTURE DIRECTION

8.1 Summary and discussion

In this section, I will illustrate the significance of our work and summarize the essential experimental results.

In my thesis work, my co-workers and I explored the cooperative phenomena caused by e-h correlation in a highly photoexcited microcavity at room temperature. The photoexcited carriers form EHP with Fermi level about 80 meV above the band gap E_g of QW in microcavity. A fraction of electrons and holes in EHP can transform to light-induced correlated e-h pairs with energy near but not locked to cavity resonance E_c. These correlated e-h pairs results in lasing radiation when the photoexcited density exceeds the critical density. Few experimental results are listed and discussed in the following to support that the lasing radiation studied here is the stimulated emission of correlated e-h pairs instead of cavity photons:

- Dynamics of PL under flattop excitation: When the microcavity sample is pumped by flattop excitation with power far above lasing threshold P_{th}, a broad-band lasing radiation commences with transient lasing energy red-shifting in time domain (Fig. 4.10-c). The effective E_c determined by the refractive index of DBR is almost fixed within 100 ps after excitation. Therefore, the red-shift of lasing radiation can exclude the lasing mechanism from conventional laser in which the laser energy is locked to E_c. The energy shift of PL results from the chemical potential drop of correlated e-h pairs due to the dissipation of EHP. The dynamics of PL resembles the superfluorescence in the semiconductor QW [14, 15, 16] with the similar photoexcited density but at cryogenic temperature. Spontaneous construction of quantum correlation is a crucial factor resulting in these macroscopic cooperative phenomena. Such correlation can be enhanced with the assistance of E_c field, and make it possible

to realize quantum many-body phenomena at room temperature. Therefore, the energy level of correlated e-h pairs is near by E_c with estimated $\Delta E \sim 15$ meV range nearby E_c.

- Dynamics of multiple lasing from harmonic confinement: The multiple lasing with discrete energies from harmonic confinement appear with separate rising time in an order of high to low energy (Fig. 6.3). The condition for lasing from each energy state requires that the energy of correlated e-h pairs is resonant to the traverse cavity mode induced by the optically induced confinement. The chemical potential of correlated e-h pairs drops due to the dissipation of e-h pairs in EHP, so the sequential multiples lasing commence from high to low energy states. In conventional laser theory, it is expected that the ground state of traverse modes commences lasing radiation first, which is inconsistent to our experimental result.

- Large differential reflectance change in pump-probe spectroscopy: The magnitude of differential reflectance change $\Delta R/R$ in pump-probe spectroscopy is as large as 0.5 (Fig. 7.2). The $\Delta R/R$ is the result of effective reflective index change due to the combination of two effects: the reduction of light absorption in DBR materials, and the enhancement of nonlinearity caused by e-h correlation. From the result of Fig. 7.10, the DBR contributes to about 40 % $\Delta R/R$, and the e-h correlation leads to 60 % $\Delta R/R$.

Besides the exploration of correlated e-h pairs at room temperature, our work provides comprehensive analysis and potential impact for applications. The selective merits of my research include:

- The angle-resolved spectroscopy with increasing pump flux is measured to characterize the energy-momentum dispersion of photoexcited carriers. The dynamic of luminescence as well as the transient optical constant change are explored through Streak image and pump-probe spectroscopy. The pump-probe experimental setup includes synchronized two laser systems, which increases the feasibility of dynamical investigation in semiconductors especially when the energy difference between the excited pump and PL exceeds 200 meV. These

measurement determines the transient E_c and the dynamics of the correlated e-h pairs with photoexcited density.

- The luminescence displays highly circular-polarized lasing radiation even the microcavity sample is excited by nonresonant elliptically polarized light (Fig. 4.6). It is uncommon because the spin relaxation time of photoexcited carriers is less 10 ps and the laser commences at 20-30 ps after excitation, so the lasing radiation is expected to be unpolarized. The spin-polarized lasing from microcavity is attributed to a spin-dependent stimulated process of correlated e-h pairs. The luminescence polarization change with pump polarization can contribute to polarization-control of spin lasers.

- The microcavity under optically induced harmonic confinement produces sequential multiple lasing. The dispersion of luminescence resembles the quantum harmonic oscillator, and the pattern of harmonic states can be adjusted by tuning the beam profile size (Fig. 6.2). The beam shaping technique can be utilized to generate other desired optical confining potential to control the behavior of luminescence.

I list my publications relevant to our work in the following:

- **Ch. 4: Ultrafast spin-polarized lasing in a highly photoexcited semiconductor microcavity at room temperature.** [*F. Hsu, W. Xie, Y. Lee, S. Lin, and C. Lai*, Phys. Rev. B **91**, 195312 (2015)]

  Ch. 5: Transient dual-energy lasing in a semiconductor microcavity. [*F. Hsu, W. Xie, Y. Lee, S. Lin, and C. Lai*, Sci. Rep. **5**, 15347 (2015)]

- **Ch. 6: Multiple-pulse lasing from harmonic states in a highly photoexcited microcavity.** [*W. Xie, F. Hsu, Y. Lee, S. Lin, and C. Lai*, arXiv:1502.00040 (2015)]

- **Ch. 7: Transient reflectance studies of optically induced resonances in a semiconductor microcavity.** [in preparation]

8.2 Future direction

From previous sections, we have a conjecture to interpret experimental results: the correlated electron-hole pairs form at below the Fermi-edge of electron-hole plasma in the presence of the cavity light field. These correlated e-h pairs form a macroscopic coherent state through a spin-dependent stimulated process, resulting in circularly polarized superradiance-like radiation (lasing). Lasing energy depends on the density of correlated e-h pairs and redshifts with time as a result of dissipation via radiation.

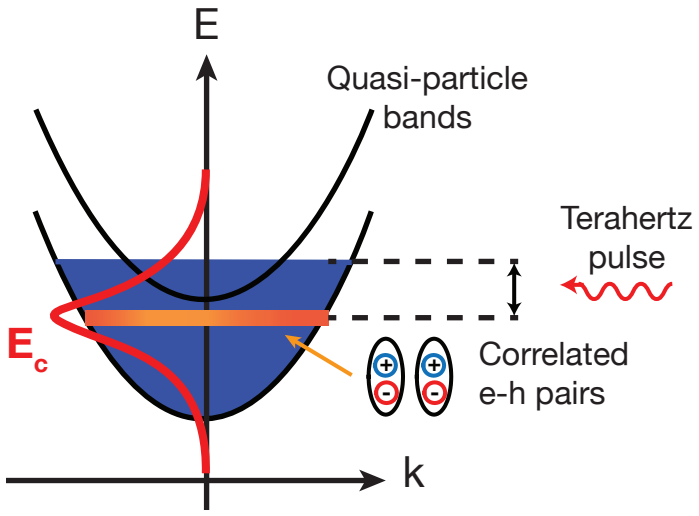

Figure 8.1 **Diagram of terahertz experiment.** The parabolic-like curves here are the band of quasiparticle (or the electron-hole pairings) in quantum wells. Photoexcited electron-hole pairs fill the band above the second quantized levels. The correlated e-h pairs are assumed to form below the Fermi-edge surface of quasiparticle. The correlated e-h pairs are expected to be ionized upon Fermi-edge surface if the sample is excited by a second lasing pulse with controlled energy matching the difference between Fermi-edge surface and the energy level of correlated e-h pairs.

To confirm correlated e-h pairs and the energy level of e-h pairs, we propose an experiment shown in Fig. 8.1. A tunable terahertz (THz) light source is used to excite the high-density plasmas, and the consequent luminescence/radiation generated by the 2-ps pulse pump excitation is monitored. If there is a gap caused by the BCS-like with correlated e-h pairs or a gap between the condensed e-h pairs and the quasi-Fermi level, the radiation would be greatly suppressed when THz light source is in resonance with the gap that might be as high as 20 meV.

There is still a lack of microscopic theoretical understanding of the density dependent lasing energy and linewidth caused by the possible formation of correlated e-h pairs at room temperature. We hope the results on lasing in highly photoexcited microcavities as reported in this thesis would lead to further developments to harness many-body effects and spin degree of freedom to control lasing or superradiance.

APPENDICES

APPENDIX A

TYPICAL VERTICAL-CAVITY SURFACE-EMITTING LASER CHARACTERISTIC

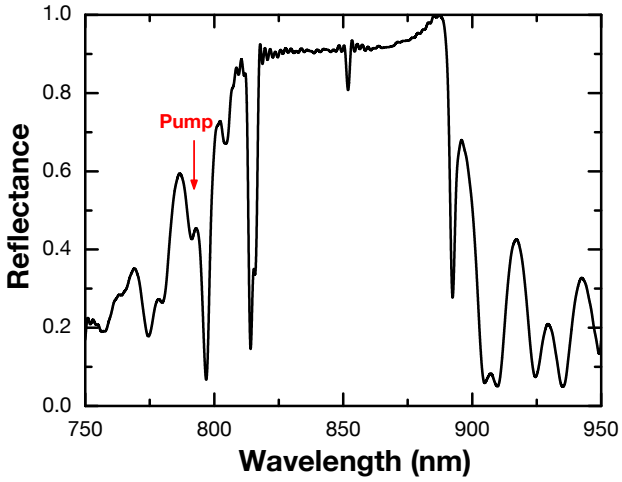

Figure A.1 **Reflectance spectrum of VCSEL.** the reflectance spectrum of VCSEL provided from Global Communication Semiconductors, LCC company. The bare cavity resonance is around 850 nm. The red arrow shows excitation wavelength 785 nm using in the experiment.

Here we compare luminescence characteristics of our microcavity sample with conventional vertical-cavity surface-emitting laser (VCSEL). The compared laser provided by Global Communication Semiconductors Inc company is 10Gps 850nm VCSEL (Do188-VCSEL). The reflectance spectrum is shown in Fig. A.1. In the experiment, we optically pump VCSEL with the same excitation of 785-nm Ti-sapphire laser pulse. The VCSEL exhibits nonlinear increase output vs. input with relative high lasing threshold compared to our case (Fig. 4.2). The largest efficiency (same definition in Sec. 4.1) of output in the experiment we can achieve is less than 0.5 % at 1.3 P_{th} (Fig. A.2 (b)). Compared to our result Fig. 4.2 (b), the efficiency reaches 3 % at 1.3 P_{th}, and the difference can be larger if we compare them with the same transmitted pump flux. The VCSEL studied here exhibits linearly polarized radiation in preference at above lasing threshold, which is different that our microcavity laser prefers circular polarization.

The crucial distinction between our microcavity laser and conventional VCSEL is the large

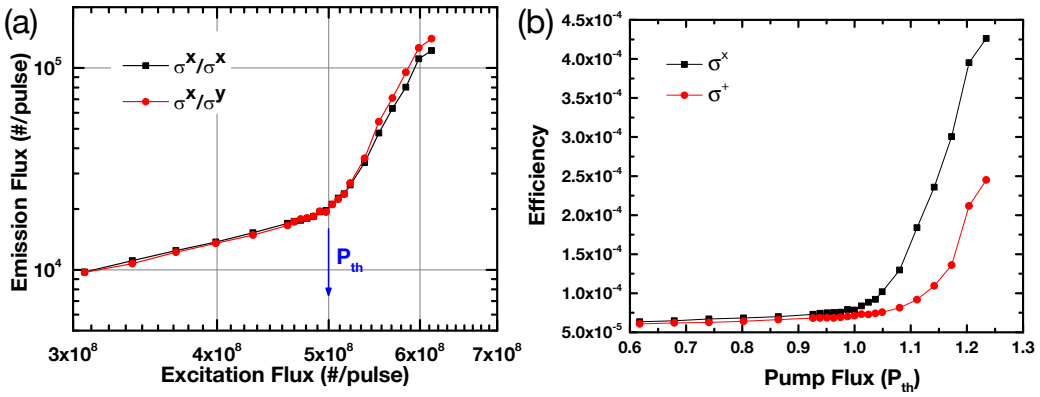

Figure A.2 **Nonlinear increase and efficiency in VCSEL.** (a) output flux versus input under linearly polarized excitation. The blue arrows denotes the lasing threshold, corresponding to 5×10^8 photon counts per pulse transmitted into VCSEL. (b) Output efficiency as a function of pump flux with linear (black) and circular (red) polarizations. The efficiency is calculated from the ratio between the output and input shown on the left.

energy shift. Fig. A.3 demonstrate the angle-resolved spectroscopy at selected pump flux in VCSEL. Below lasing threshold, parabolic-like dispersion emerges at the bare cavity resonance 1.456 eV (λ = 852 nm). Near and above threshold, radiation becomes spectrally and angularly narrow with energy exactly at bare cavity. Compared to spectral characteristics of our result (Fig. 4.4), the energy peak of our sample exhibits 10 meV with increasing pump flux. The origin of large energy shift is the large detuning between quantum well band gap and cavity resonance, which enhances accumulation of e-h density resulting in photomodulted index change.

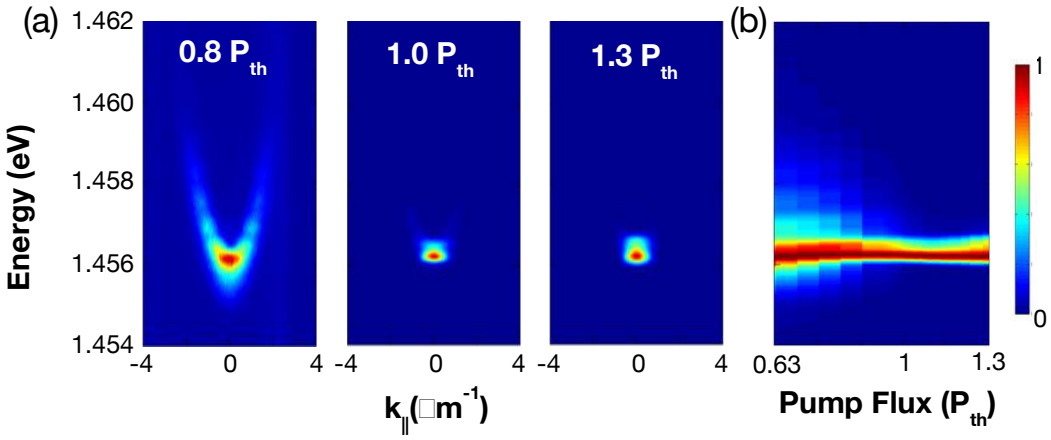

Figure A.3 **Angle-resolved spectroscopy in VCSEL.** (a) Angle-resolved spectroscopy in VCSEL with selected power 0.8, 1 and 1.3 P_{th} measured from σ^x/σ^x component. (b) 2D image of spectra versus pump flux. Each slice represents normalized spectrum obtained from time-integrated spectrum near $k \simeq 0$.

APPENDIX B

REFERENCE OF TERMINOLOGY ABBREVIATION

The following table lists the abbreviated words or terminology frequently used in this dissertation:

BEC	$\Rightarrow$ Bose-Einstein condensation
DBR	$\Rightarrow$ distributed Bragg reflector
DoCP	$\Rightarrow$ degree of circular polarization
FWHM	$\Rightarrow$ full width half maximum
e-h	$\Rightarrow$ electron-hole
e-h-γ	$\Rightarrow$ electron-hole-photon
EHP	$\Rightarrow$ electron-hole plasma
MQW	$\Rightarrow$ multiple quantum well
PL	$\Rightarrow$ photoluminescence
QD	$\Rightarrow$ quantum dot
QW	$\Rightarrow$ quantum well
SLM	$\Rightarrow$ spatial light modulator
VCSEL	$\Rightarrow$ vertical-cavity surface-emitting laser
$\Delta R/R$	$\Rightarrow$ differential reflectance change

BIBLIOGRAPHY

BIBLIOGRAPHY

[1] M. H. Anderson, J. R. Ensher, M. R. Matthews, C. E. Wieman, and E. A. Cornell, "Observation of Bose-Einstein condensation in a dilute atomic vapor," Science **269**, 198 (1995).

[2] K. B. Davis, M. O. Mewes, M. R. Andrews, N. J. van Druten, D. S. Durfee, D. M. Kurn, and W. Ketterle, "Bose-Einstein Condensation in a Gas of Sodium Atoms," Phys. Rev. Lett. **75**, 3969 (1995).

[3] L. V. Keldyh and A. N. Kozlov, "Collective properties of excitons in semiconductors," Sov. Phys. JETP **27**, 521 (1968).

[4] E. Hanamura and H. Haug, "Condensation effects of excitons," Phys. Rep.-Rev. Sec. Phys. Lett. **33**, 209 (1977).

[5] C. Weisbuch, M. Nishioka, A. Ishikawa, and Y. Arakawa, "Observation of the coupled exciton-photon mode splitting in a semiconductor quantum microcavity," Phys. Rev. Lett. **69**, 3314 (1992).

[6] H. Deng, H. Huag, and Y. Yamamoto, "Exciton-polariton Bose-Einstein condensate," Rev. Mod. Phys. **82**, 1489 (2010).

[7] J. L. Lin and J. P. Wolfe, "Bose-Einstein condensation of paraexcitons in stressed Cu_2O," Phys. Rev. Lett. **71**, 1222 (1993).

[8] A. Mysyrowicz, E. Benson, and E. Fortin, "Directed Beam of Excitons Produced by Stimulated Scattering," Phys. Rev. Lett. **77**, 896 (1996).

[9] L. V. Butov, C. W. Lai, A. L. Ivanov, A. C. Gossard, and D. S. Chemla, "Towards Bose-Einstein condensation of excitons in potential traps," Nature **417**, 47 (2002).

[10] D. Snoke, S. Denev, Y. Liu, L. Pfeiffer, and K. West, "Long-range transport in excitonic dark states in coupled quantum wells," Nature **418**, 754 (2002).

[11] C. R. and K. Ploog, "Frequency and density dependent radiative recombination processes in IIIâĂŞV semiconductor quantum wells and superlattices," Adv. Phys. **40**, 535 (1991).

[12] S. Schmitt-Rink, C. Ell, and H. Haug, "Many-body effects in the absorption, gain, and luminescence spectra of semiconductor quantum-well structures," Phys. Rev. B **33**, 1183 (1986).

[13] P. B. Littlewood and X. J. Zhu, "Possibilities for exciton condensation in semiconductor quantum-well structures," Phys. Scripta **T68**, 56–67 (1996).

[14] G. T. N. Noe II, J. H. Kim, J. Lee, Y. Wang, A. K. Wojcik, S. A. McGill, D. H. Reitze, A. A. Belyanin, and J. Kono, "Giant superfluorescent bursts from a semiconductor magneto-plasma," Nature Physics **8**, 219 (2012).

[15] J. H. Kim, G. T. N. Noe II, S. A. McGill, Y. Wang, A. K. Wojcik, A. A. Belyanin, and J. Kono, "Fermi-edge superfluorescence from a quantum degenerate electron-hole gas," Sci. Rep. **3**, 3283 (2013).

[16] K. Cong, Y. Wang, J. H. Kim, G. T. Noe II, S. A. McGill, A. Belyanin, and J. Kono, "Superfluorescence from photoexcited semiconductor quantum wells: Magnetic field, temperature, and excitation power dependence," Phys. Rev. B **91**, 235,448 (2015).

[17] H. Deng, G. Weihs, C. Santori, J. Bloch, and Y. Yamamoto, "Condensation of semiconductor microcavity exciton polaritons," Science **298**, 199 (2002).

[18] H. Deng, G. Welhs, D. Snoke, J. Bloch, and Y. Yamamoto, "Polariton lasing vs. photon lasing in a semiconductor microcavity," Proc. Natl. Acad. Sci. U.S.A. **100**, 15,318 (2003).

[19] R. Balili, V. Hartwell, D. Snoke, L. Pfeiffer, and K. West, "Bose-Einstein condensation of microcavity polaritons in a trap," Science **316**, 1007 (2007).

[20] J. Kasprzak, M. Richard, S. Kundermann, A. Baas, P. Jeambrun, J. M. J. Keeling, F. M. Marchetti, M. H. Szymaska, R. Andre, J. L. Staehli, V. Savona, P. B. Littlewood, B. Deveaud, and L. S. Dang, "Bose-Einstein condensation of exciton polaritons," Nature **443**, 409 (2006).

[21] K. G. Lagoudakis, M. Wouters, M. Richard, A. Baas, I. Carusotto, R. Andre, L. S. Dang, and B. Deveaud, "Quantized vortices in an exciton–polariton condensate," Nature Phys. **4**, 706 (2008).

[22] G. Roumpos, M. D. Fraser, A. Loffler, S. Hofling, A. Forchel, and Y. Yamamoto, "Single vortex-antivortex pair in an exciton-polariton condensate," Nautre Phys. **7**, 129 (2011).

[23] V. L. Berezinskii, "Destruction of long-range order in one-dimensional and two-dimensional systems possessing a continuous symmetry group. II. quantum systems." Sov. Phys. JETP **34**, 610 (1972).

[24] J. M. Kosterlitz and D. J. Thouless, "Ordering, metastability and phase transitions in two-dimensional systems," J. Phys. C6 **6**, 1181 (1973).

[25] N. N. Bogoliubov, "On the theory of superfluidity," J. Phys. (USSR) **11**, 23 (1947).

[26] S. Utsunomiya, L. Tian, G. Roumpos, C. W. Lai, N. Kumada, T. Fujisawa, M. Kuwata-Gonokami, A. Loffler, S. Hofling, A. Forchel, and Y. Yamamoto, "Observation of Bogoliubov excitations in exciton-polariton condensates," Nature Phys. **4**, 700 (2008).

[27] A. Amo, D. Sanvitto, F. P. Laussy, D. Ballarini, E. del Valle, M. D. Martin, A. Lemaitre, J. Bloch, D. N. Krizhanovskii, M. S. Skolnick, C. Tejedor, and L. Viña, "Collective fluid dynamics of a polariton condensate in a semiconductor microcavity," Nature **457**, 291 (2009).

[28] G. Nardin, G. Grosso, Y. Leger, B. Pietka, F. Morier-Genoud, and B. Deveaud-Pledran, "Hydrodynamic nucleation of quantized vortex pairs in a polariton quantum fluid," Nature Phys. **7**, 635 (2011).

[29] C. W. Lai, J. Zoch, A. C. Gossard, and D. S. Chemla, "Phase Diagram of Degenerate Exciton Systems," Science **303**, 503 (2004).

[30] D. Sanvitto, A. Amo, L. Viña, R. André, D. D. Solnyshkov, and G. Malpuech, "Exciton-polariton condensation in a natural two-dimensional trap," Phys. Rev. B **80**, 045,301 (2009).

[31] M. De Giorgi, D. Ballarini, P. Cazzato, G. Deligeorgis, S. I. Tsintzos, Z. Hatzopoulos, P. G. Savvidis, G. Gigli, F. P. Laussy, and D. Sanvitto, "Relaxation Oscillations in the Formation of a Polariton Condensate," Phys. Rev. Lett. **112**, 113,602 (2014).

[32] H. S. Nguyen, Z. Han, K. Abdel-Baki, X. Lafosse, A. Amo, J. S. Lauret, E. Deleporte, S. Bouchoule, and J. Bloch, "Quantum confinement of zero-dimensional hybrid organic-inorganic polaritons at room temperature," Appl. Phys. Lett. **104**, 081,103 (2014).

[33] R. I. Kaitouni, O. El Daif, A. Baas, M. Richard, T. Paraiso, L. P., T. Guillet, F. Morier-Genoud, J. D. Ganiere, J. L. Staehli, V. Savona, and B. Deveaud, "Engineering the spatial confinement of exciton polaritons in semiconductors," Phys. Rev. B **74**, 155,311 (2006).

[34] C. W. Lai, N. Y. Kim, S. Utsunomiya, G. Roumpos, H. Deng, M. D. Fraser, T. Byrnes, P. Recher, N. Kumada, T. Fujisawa, and Y. Y, "Coherent zero-state and p-state in an exciton–polariton condensate array," Nature **450**, 529 (2007).

[35] D. Bajoni, P. Senellart, E. Wertz, I. Sagnes, A. Miard, A. Lemaître, and J. Bloch, "Polariton laser using single micropillar GaAs-GaAlAs semiconductor cavities," Phys. Rev. Lett. **100**, 047,401 (2008).

[36] E. Wertz, L. Ferrier, D. D. Solnyshkov, J. R., D. Sanvitto, A. Lemaitre, I. Sagnes, R. Grousson, A. V. Kavokin, P. Senellart, G. Malpuech, and J. Bloch, "Spontaneous formation and optical manipulation of extended polariton condensates," Nature Phys. **6**, 860 (2010).

[37] E. Wertz, A. Amo, D. D. Solnyshkov, L. Ferrier, T. C. H. Liew, D. Sanvitto, P. Senellart, I. Sagnes, A. Lemaitre, A. V. Kavokin, G. Malpuech, and J. Bloch, "Propagation and amplification dynamics of 1D polariton condensates," Phys. Rev. Lett. **109**, 216,404 (2012).

[38] M. Maragkou, A. J. D. Grundy, E. Wertz, A. Lemaitre, I. Sagnes, P. Senellart, J. Bloch, and P. G. Lagoudakis, "Spontaneous nonground state polariton condensation in pillar microcavities," Phys. Rev. B **81**, 081,307 (2010).

[39] F. Manni, K. G. Lagoudakis, T. C. H. Liew, R. Andre, and B. Deveaud, "Spontaneous pattern formation in a polariton condensate," Phys. Rev. Lett. **107**, 106,401 (2011).

[40] G. Tosi, G. Christmann, N. G. Berloff, P. Tsotsis, T. Gao, Z. Hatzopoulos, P. G. Savvidis, and J. J. Baumberg, "Sculpting oscillators with light within a nonlinear quantum fluid," Nature Phys. **8**, 190 (2012).

[41] P. Cristofolini, A. Dreismann, G. Christian, N. Franchetti, N. G. Berloff, P. Tsotsis, Z. Hadzibabic, P. G. Savvidis, and J. J. Baumberg, "Optical superfluid phase transitions and trapping of polariton condensates," Phys. Rev. Lett. **110**, 186,403 (2013).

[42] A. Dreismann, P. Cristofolini, R. Balili, G. Christian, F. Pinsker, N. G. Berloff, Z. Hatzopoulos, P. G. Savvidis, and J. J. Baumberg, "Coupled counterrotating polariton condensates in optically defined annular potentials," PNAS **111**, 8770 (2014).

[43] S. Christopoulos, G. B. H. von Högersthal, A. J. D. Grundy, P. G. Lagoudakis, A. V. Kavokin, J. J. Baumberg, G. Christmann, R. Butté, E. Feltin, J.-F. Carlin, and N. Grandjean, "Room-temperature polariton lasing in semiconductor microcavities," Phys. Rev. Lett. **98**, 126,405 (2007).

[44] A. Das, J. Heo, M. Jankowski, W. Guo, L. Zhang, H. Deng, and P. Bhattacharya, "Room temperature ultralow threshold GaN nanowire polariton laser," Phys. Rev. Lett. **107**, 066,405 (2011).

[45] P. Bhattacharya, T. Frost, S. Deshpande, M. Z. Baten, A. Hazari, and A. Das, "Room temperature electrically injected polariton laser," Phys. Rev. Lett. **112**, 236,802 (2014).

[46] T. Guillet, M. Mexis, J. Levrat, G. Rossbach, C. Brimont, T. Bretagnon, B. Gil, R. Butte, N. Grandjean, L. Orosz, F. Reveret, J. Leymarie, J. Zuniga-Perez, M. Leroux, F. Semond, and S. Bouchoule, "Polariton lasing in a hybrid bulk ZnO microcavity," Appl. Phys. Lett. **99**, 161,104 (2011).

[47] W. Xie, H. Dong, S. Zhang, L. Sun, W. Zhou, Y. Ling, J. Lu, X. Shen, and Z. Chen, "Room-temperature polariton parametric scattering driven by a one-dimensional polariton condensate," Phys. Rev. Lett. **108**, 166,401 (2012).

[48] D. Xu, W. Xie, W. Liu, J. Wang, L. Zhang, Y. Wang, S. Zhang, L. Sun, X. Shen, and Z. Chen, "Polariton lasing in a ZnO microwire above 450K," Appl. Phys. Lett. **104**, 082,101 (2014).

[49] P. P. Vasil'ev and I. V. Smetanin, "Condensation of electron-hole pairs in a degenerate semiconductor at room temperature," Phys. Rev. B **74**, 125,206 (2006).

[50] C. Comte and G. Mahler, "Dynamic Stark effect in interacting electron-hole systems: Light-enhanced excitons," Phys. Rev. B **34**, 7164 (1986).

[51] J. Rudolph, D. Hagele, H. M. Gibbs, G. Kihitrova, and M. Oestreich, "Laser threshold reduction in a spintronic device," Appl. Phys. Lett. **82**, 4516 (2003).

[52] J. Rudolph, S. Dohrmann, D. Hagele, M. Oestreich, and W. Stolz, "Room-temperature threshold reduction in vertical-cavity surface-emitting lasers by injection of spin-polarized electrons," Appl. Phys. Lett. **87**, 241,117 (2005).

[53] M. Holub, J. Shin, D. Saha, and P. Bhattacharya, "Electrical spin injection and threshold reduction in a semiconductor laser," Phys. Rev. Lett. **98**, 146,603 (2007).

[54] H. Ando, T. Sogawa, and H. Gotoh, "Photon-spin controlled lasing oscillation in surface-emitting lasers," Appl. Phys. Lett. **73**, 566 (1998).

[55] I. Zutic, J. Fabian, and S. D. Sarma, "Spintronics: fundamentals and applications," Rev. Mod. Phys. **76**, 323 (2004).

[56] S. Hovel, N. C. Gerhardt, M. R. Hofmann, J. Yang, D. Reuter, and A. Wieck, "Spin controlled optically pumped vertical cavity surface emitting laser," Electron, Lett. **41**, 251 (2005).

[57] N. Gerhardt, S. Hovel, M. Hofmann, J. Yang, D. Read, and A. Wieck, "Enhancement of spin information with vertical cavity surface emitting lasers," Electron, Lett. **42**, 88 (2006).

[58] S. Iba, S. Koh, K. Ikeda, and H. Kawaguchi, "Room temperature circularly polarized lasing in an optically spin injected vertical-cavity surface-emitting laser with (110) GaAs quantum wells," Appl. Phys. Lett. **98**, 081,113 (2011).

[59] I. A. Shelykh, A. Kavokin, Y. G. Rubo, T. C. H. Liew, and G. Malpuech, "Polariton polarization-sensitive phenomena in planar semiconductor microcavities," Semicond. Sci. Technol. **25**, 013,001 (2010).

[60] A. Kavokin, G. Malpuech, and M. Glazov, "Optical spin Hall effect," Phys. Rev. Lett. **95**, 136,601 (2005).

[61] C. Leyder, M. Romanelli, J. P. Karr, E. Giacobino, T. C. H. Liew, M. Glazov, A. Kavokin, G. Malpuech, and A. Bramati, "Observation of the optical spin Hall effect," Nature Phys. **3**, 628 (2007).

[62] P. Renucci, T. Amand, X. Marie, P. Senellart, J. Bloch, B. Sermage, and K. V. Kavokin, "Microcavity polariton spin quantum beats without a magnetic field: A manifestation of Coulomb exchange in dense and polarized polariton systems," Phys. Rev. B **72**, 075,317 (2005).

[63] A. V. Kavokin, J. J. Baumberg, G. Malpuech, and F. P. Laussy, *Microcavities* (Oxford Science Publication, 2007).

[64] T. Byrnes, N. Y. Kim, and Y. Yamamoto, "Exciton–polariton condensates," Nature Phys. **10**, 803 (2014).

[65] T. Horikiri, P. Schwendimann, A. Quattropani, S. Höfling, A. Forchel, and Y. Yamamoto, "Higher order coherence of exciton-polariton condensates," Phys. Rev. B **81**, 033,307 (2010).

[66] S. S. Hodgman, R. G. Dall, K. G. H. Manning, A. G. Baldwin, and A. G. Truscott, "Direct measurement of long-range third-order coherence in Bose-Einstein condensates," Science **331**, 1046 (2011).

[67] D. Bajoni, P. Senellart, A. Lemaitre, and J. Bloch, "Photon lasing in GaAs microcavity: Similarities with a polariton condensate," Phys. Rev. B **76**, 201,305 (2007).

[68] E. Kammann, H. Ohadi, M. Maragkou, A. V. Kavokin, and K. G. Lagoudakis, "Crossover from photon to exciton-polariton lasing," New J. Phys. **14**, 105,003 (2012).

[69] N. Y. Kim, K. Kusudo, C. Wu, N. Masumoto, A. Loffler, S. Hofling, N. Kumada, L. Worschech, A. Forchel, and Y. Yamamoto, "Dynamical d-wave condensation of excitonâĂŞpolaritons in a two-dimensional square-lattice potential," Nature Phys. **7**, 681 (2011).

[70] T. Jacqmin, I. Carusotto, I. Sagnes, M. Abbarchi, D. D. Solnyshkov, G. Malpuech, E. Galopin, A. Lemaitre, J. Bloch, and A. Amo, "Direct observation of Dirac cones and a flatband in a honeycomb lattice for polaritons," Phys. Rev. Lett. **112**, 116,402 (2014).

[71] N. Masumoto, N. Y. Kim, T. Byrnes, K. Kusudo, A. Loffler, S. Hofling, A. Forchel, and Y. Yamamoto, "Exciton–polariton condensates with flat bands in a two-dimensional kagome lattice," New. J. Phys. **14**, 065,002 (2012).

[72] T. C. H. Liew, A. V. Kavokin, and I. A. Shelykh, "Optical circuits based on polariton neurons in semiconductor microcavities," Phys. Rev. Lett. **101**, 016,402 (2008).

[73] T. C. H. Liew, A. V. Kavokin, T. Ostatnicky, M. Kaliteevski, I. A. Shelykh, and R. A. Abram, "Exciton-polariton integrated circuits," Phys. Rev. B **82**, 033,302 (2010).

[74] M. W. Wu, J. H. Jiang, and M. Q. Weng, "Spin dynamics in semiconductors," Phys. Report **61**, 61 (2010).

[75] Y. Ohno, R. Terauchi, T. Adachi, F. Matsukura, and H. Ohno, "Spin relaxation in GaAs(110) quantum wells," Phys. Rev. Lett. **83**, 4196 (1999).

[76] P. Yeh, *Optical Waves in Layered Media* (Wiley Interscience, 2005).

[77] G. C. DeSalvo, W. F. Tseng, and J. Comas, "Etch rates and selectivities of citric acid/hdrogen peroxide on $GaAs$, $Al_{0.3}Ga_{0.7}As$, $In_{0.2}Ga_{0.8}As$, $In_{0.53}Ga_{0.47}As$, $In_{0.52}Al_{0.48}As$, and InP," J. Electrochem. Soc. **139**, 831 (1992).

[78] E. A. Donley, T. P. Heavner, F. Levi, M. O. Tataw, and S. R. Jefferts, "Double-pass acousto-optic modulator system," Rev. Sci. Instrum. **76**, 063,112 (2005).

[79] L. A. Romero and F. M. Dickey, "Lossless laser beam shaping," J. Opt. Soc. Am. **13**, 751 (1996).

[80] R. Atanasov, F. Bassani, A. D'Andrea, and N. Tomassini, "Exciton properties and optical response in InGaAs/GaAs strained quantum wells," Phys. Rev. B **50**, 14,381 (1994).

[81] A. T. Friberg and R. J. Sudol, "Propagation parameters of gaussian Schell-model beams," Opt. Commun. **41**, 383 (1982).

[82] M. Oestreich, J. Rudolph, R. Winkler, and D. Hagele, "Design considerations for semiconductor spin lasers," Supperlattices Microstruct. **37**, 306 (2005).

[83] C. Gothgen, R. Oszwaldowski, A. Petrou, and I. Zutic, "Analytical model of spin-polarized semiconductor lasers," Appl. Phys. Lett. **93**, 042,513 (2008).

[84] J. Lee, R. Oszwaldowski, C. Gothgen, and I. Zutic, "Mapping between quantum dot and quantum well lasers: From conventional to spin lasers," Phys. Rev. B **85**, 045,314 (2012).

[85] J. Lee, S. Bearden, E. Wasner, and I. Zutic, "Spin-lasers: From threshold reduction to large-signal analysis," Appl. Phys. Lett. **105**, 042,411 (2014).

[86] N. C. Gerhardt, M. Y. Li, J. H., H. Hopfner, T. Achemann, and M. R. Hofmann, "Ultra-fast spin-induced polarization oscillations with tunable lifetime in vertical-cavity surface-emitting lasers," Appl. Phys. Lett. **99**, 151,107 (2011).

[87] N. C. Gerhardt and M. R. Hofmann, "Spin-controlled vertical-cavity surface-emitting lasers," Adv. Opt. Technol. **2012**, 268,949 (2012).

[88] H. Hopfner, M. Lindemann, N. C. Gerhardt, and M. R. Hofmann, "Controlled switching of ultrafast circular polarization oscillations in spin-polarized vertical-cavity surface-emitting lasers," Appl. Phys. Lett. **104**, 022,409 (2014).

[89] M. Adams and D. Alexandropoulos, "Parametric analysis of spin-polarized VCSELs," IEEE J. Quantum Electron. **41**, 287 (2009).

[90] B. R. Bennett, R. A. Soref, and J. A. del Alamo, "Carrier-induced change in refractive index of InP, GaAs and InGaAsP," IEEE J. Quantum Electron. **26**, 113 (1990).

[91] K. Iga, F. Koyama, and S. Kinoshita, "Surface emitting semiconductor lasers," IEEE. J. Quantum Electron. **24**, 1845 (1988).

[92] C. Chang-Hasnain, "Tunable VCSEL," IEEE J. Sel. Topics Quantum Electron. **6**, 978 (2000).

[93] F. Koyama, "Recent advances of VCSEL photonics," J. Lightw. Technol. **24**, 4502 (2006).

[94] C. H. Henry, "Theory of the linewidth of semiconductor lasers," IEEE J. Quantum Electron **18**, 259 (1982).

[95] C. H. Henry, "Phase noise in semiconductor lasers," J. Lightw. Technol. **4**, 298 (1986).

[96] Y. Arakawa and A. Yariv, "Theory of gain, modulation response, and spectral linewidth in AlGaAs quantum well lasers," IEEE J. Quantum Electron **21**, 1666 (1985).

[97] K. Panajotov and F. Prati, *Polarization dynamics of VCSELs, in VCSELs* (Springer Berlin Heidelberg, 2013).

[98] W. Xie, F. K. Hsu, Y. S. Lee, S. D. Lin, and C. W. Lai, "Multiple-pulse lasing from an optically induced harmonic confinement in a highly photoexcited microcavity," arXiv p. 1502.00040 (2015).

[99] F. K. Hsu, X. W., Y. S. Lee, S. D. Lin, and C. W. Lai, "Ultrafast spin-polarized lasing in a highly photoexcited semiconductor microcavity at room temperature," Phys. Rev. B **91**, 195,312 (2015).

[100] P. R. Eastham and P. B. Littlewood, "Bose condensation of cavity polaritons beyond the linear regime: The thermal equilibrium of a model microcavity," Phys. Rev. B **64**, 235,101 (2001).

[101] K. Kamide and T. Ogawa, "Ground-state properties of microcavity polariton condensates at arbitrary excitation density," Phys. Rev. B **83**, 165,319 (2011).

[102] K. Kamide, M. Yoshita, H. Akiyama, M. Yamaguchi, and T. Ogawa, "Fano-resonance gain by dephasing electron-hole Cooper pairs in semiconductors," J. Phys. Soc. Jpn. **81**, 093,706 (2012).

[103] X. Zhu, M. S. Hybertsen, and P. B. Littlewood, "Electron-hole system revisited: A variational quantum monte carlo study," Phys. Rev. B **54**, 13,575 (1996).

[104] M. Wouters and I. Carusotto, "Excitations in a nonequilibrium Bose-Einstein condensate of exciton polaritons," Phys. Rev. Lett. **99**, 140,402 (2007).

[105] J. Keeling, P. R. Eastham, M. H. Szymanska, and P. B. Littlewood, "BCS-BEC crossover in a system of microcavity polaritons," Phys. Rev. B **72**, 115,320 (2005).

[106] K. Kamide and T. Ogawa, "What determines the wave function of electron-hole pairs in polariton condensates?" Phys. Rev. Lett. **105**, 056,401 (2010).

[107] M. Yamaguchi, K. Kamide, T. Ogawa, and Y. Yamamoto, "BEC-BCS-laser crossover in coulomb-correlated electron-hole-photon systems," New. J. Phys. **14**, 065,001 (2012).

[108] M. Yamaguchi, K. Kamide, R. Nii, T. Ogawa, and Y. Yamamoto, "Second thresholds in BEC-BCS-laser crossover of exciton-polariton systems," Phys. Rev. Lett. **111**, 026,404 (2013).

[109] D. S. Jin, M. R. Matthews, J. R. Ensher, C. E. Wieman, and E. A. Cornell, "Temperature-dependent damping and frequency shifts in collective excitations of a dilute Bose-Einstein condensate," Phys. Rev. Lett. **78**, 764 (1997).

[110] C. J. Pethick and H. T. C. Stoof, "Collisional frequency shifts of absorption lines in an atomic hydrogen gas," Phys. Rev. A **64**, 013,618 (2001).

[111] M. O. Oktel and L. S. Levitov, "Optical excitations in a nonideal bose gas," Phys. Rev. Lett. **83**, 6 (1999).

[112] R. J. Donnelly, "The two-fluid theory and second sound in liquid helium," Phys. Today **62**, 34 (2009).

[113] P. G. Lagoudakis, M. D. Martin, J. J. Baumberg, G. Malpuech, and A. V. Kavokin, "Coexistence of low threshold lasing and strong coupling in microcavities," J. Appl. Phys. **95**, 2487 (2004).

[114] H. Ohadi, E. Kammann, T. C. H. Liew, K. G. Lagoudakis, A. V. Kavokin, and P. G. Lagoudakis, "Spontaneous symmetry breaking in a polariton and photon laser," Phys. Rev. Lett. **109**, 016,404 (2012).

[115] R. H. Dicke, "Coherence in spontaneous radiation processes," Phys. Rev. **93**, 99 (1954).

[116] V. V. Zheleznyakov, V. V. Kocharovskii, and V. V. Kocharovskii, "Polarization waves and super-radiance in active media," Sov. Phys. Usp. **32**, 835 (1989).

[117] Y. D. Jho, X. Wang, J. Kono, D. H. Reitze, X. Wei, A. A. Belyanin, V. V. Kocharovskii, V. V. Kocharovskii, and G. S. Solomon, "Cooperative recombination of a quantized high-density electron-hole plasma in semiconductor quantum wells," Phys. Rev. Lett. **96**, 237,401 (2006).

[118] Y. D. Jho, X. Wang, D. Read, J. Kono, A. A. Belyanin, V. V. Kocharovskii, V. V. Kocharovskii, and G. S. Solomon, "Cooperative recombination of electron-hole pairs in semiconductor quantum wells under quantizing magnetic fields," Phys. Rev. B **81**, 155,314 (2010).

[119] D. S. Chemla and D. A. B. Miller, "Room-temperature excitonic nonlinear-optical effects in semiconductor quantum-well structures," J. Opt. Soc. Am. B **2**, 1155 (1985).

[120] M. Colocci, M. Gurioli, and V. Vinattieri, "Thermal ionization of excitons in GaAs/AlGaAs quantum well structures," J. Appl. Phys. **68**, 2809 (1990).

[121] M. H. Szymanska, J. Keeling, and P. B. Littlewood, "Nonequilibrium quantum condensation in an incoherently pumped dissipative system," Phys. Rev. Lett. **96**, 230,602 (2006).

[122] P. Mandel and M. Tlidi, "Transverse dynamics in cavity nonlinear optics (2000âĂŞ2003)," J. Opt. B: Quantum Semiclass. Opt. **6**, R60 (2004).

[123] C. J. Chang-Hasnain, J. P. Harbison, G. Hasnain, A. C. Von Lehmen, L. T. Florez, and N. G. Stoffel, "Dynamic, polarization, and transverse mode characteristics of vertical cavity surface emitting lasers," IEEE J. Quantum Electron. **27**, 1402 (1991).

[124] H. Zhang, G. Mrozynski, A. Walrabenstein, and J. Schrage, "Analysis of transverse mode competition of VCSELs based on a spatially independent model," IEEE J. Quantum Electron. **40**, 18 (2004).

[125] J. P. Reithmaier, M. Rohner, H. Zull, F. Schafer, A. Forchel, P. A. Knipp, and T. L. Reinecke, "Size dependence of confined optical modes in photonic quantum dots," Phys. Rev. Lett. **78**, 378 (1997).

[126] S. W. Koch, F. Jahnke, and W. W. Chow, "Physics of semiconductor microcavity lasers," Semicond. Sci. Technol. **10**, 739 (1995).

[127] R. Sarzala, T. Czyszanowski, M. Wasiak, M. Dems, L. Piskorski, W. Nakwaski, and K. Panajotov, "Numerical self-consistent analysis of VCSELs," Adv. Opt. Technol. **2012**, 17 (2012).

[128] D. Campi, G. Coli, and M. Vallone, "Formulation of the optical response in semiconductors and quantum-confined structures," Phys. Rev. B **57**, 4681 (1998).

[129] C. Tanguy, "Analytical expression of the complex dielectric function for the Hulthen potential," Phys. Rev. B **60**, 10,660 (1999).

[130] Y. H. Lee, A. Chavez-Pirson, S. W. Koch, H. M. Gibbs, S. H. Park, J. Morchange, A. Jeffery, N. Peyghambarian, L. Banyai, A. C. Gossard, and W. Wiegmann, "Room-temperature optical nonlinearities in GaAs," Phys. Rev. Lett. **57**, 2446 (1986).

[131] L. Huang, J. P. Callan, E. N. Glezer, and E. Mazur, "GaAs under intense ultrafast excitation: response of the dielectric function," Phys. Rev. Lett. **80**, 185 (1998).